






Universitat Autònoma de Barcelona

**Contribution of histone modifications
to double-strand break repair and aging**

Lourdes González Bermúdez

ADVERTIMENT. L'accés als continguts d'aquesta tesi queda condicionat a l'acceptació de les condicions d'ús establertes per la següent llicència Creative Commons:  http://cat.creativecommons.org/?page_id=184

ADVERTENCIA. El acceso a los contenidos de esta tesis queda condicionado a la aceptación de las condiciones de uso establecidas por la siguiente licencia Creative Commons:  <http://es.creativecommons.org/blog/licencias/>

WARNING. The access to the contents of this doctoral thesis it is limited to the acceptance of the use conditions set by the following Creative Commons license:  <https://creativecommons.org/licenses/?lang=en>

Contribution of histone modifications to double-strand break repair and aging

Lourdes González Bermúdez



UAB
2019

Contribution of histone modifications to double-strand break repair and aging

Lourdes González Bermúdez

Report submitted to qualify for the Doctor Philosophy Degree in Cell Biology
at the Universitat Autònoma de Barcelona

Memoria presentada para optar al Grado de Doctora en Biología Celular por
la Universitat Autònoma de Barcelona

Tesis doctoral inscrita en el Departament de Biologia Cel·lular, de Fisiologia i
d'Immunologia de la Universitat Autònoma de Barcelona

Directors / Directoras:

Dra. Marta Martín Flix

Dra. Mariona Terradas III

Bellaterra, 2019



Universitat Autònoma de Barcelona

La **Dra. Marta Martín Flix**, profesora del Departament de Biologia Cel·lular, Fisiologia i Immunologia de la Universitat Autònoma de Barcelona,

La **Dra. Mariona Terradas III**, investigadora del Departament de Càncer Hereditari de l'Institut d'Investigació Biomèdica de Bellvitge,

CERTIFICAN:

Que **Lourdes González Bermúdez** ha realizado bajo su dirección el presente trabajo de investigación que lleva por título "**Contribution of histone modifications to double-strand break repair and aging**" para optar al grado de Doctora por la Universitat Autònoma de Barcelona.

Que este trabajo se ha llevado a cabo en la Unitat de Biologia Cel·lular del Departament de Biologia Cel·lular, de Fisiologia i d'Immunologia de la Universitat Autònoma de Barcelona.

Y para que así conste, firman el presente certificado.

Dra. Marta Martín Flix

Dra. Mariona Terradas III

Lourdes González Bermúdez

Bellaterra, 19 de septiembre de 2019

Este estudio ha sido financiado por:

- Consejo de Seguridad Nacional.
- Fundación Dexeus Salud de la Mujer.
- Generalitat de Catalunya (proyectos: 2014 SGR-524 y 2017 SGR-503).

Lourdes González Bermúdez ha sido beneficiaria de una beca predoctoral para personal investigador en formación (PIF 2015), concedida por la Universitat Autònoma de Barcelona.

«Golpe a golpe, verso a verso»

Proverbios y Cantares, Antonio Machado.

Adaptado por Joan Manuel Serrat.

A mi familia, especialmente a mi padre,
por ayudarme a matar dragones.

A Stefano,
por su amor generoso y paciente.

A mi amiga Ángeles,
por su fortaleza y por recordarme, a su pesar,
la importancia de la investigación biomédica.

Index

<u>ABSTRACT</u>	<u>1</u>
<u>RESUMEN</u>	<u>3</u>
<u>ABBREVIATIONS</u>	<u>5</u>
<u>INTRODUCTION</u>	<u>9</u>
1. DNA damage	11
1.1. Sources and types of DNA lesions	11
1.2. DNA damage response	13
1.2.1. Recognition and signaling of DSBs	13
1.2.2. DSB repair pathways	15
a. Nonhomologous end joining (NHEJ)	15
b. Homologous recombination (HR)	17
c. Choice between NHEJ and HR	19
2. Chromatin dynamics in response to DNA damage	22
2.1. Chromatin structure	22
2.2. Post-translational modifications of histones	24
2.2.1. Histone acetylation	26
Acetylation of histone 4 at lysine 16 (H4K16Ac)	27
2.2.2. Histone lysine deamination: oxidation of H3 at lysine 4 (H3K4ox)	30

3. Aging	31
3.1. DNA damage response in aging	32
3.2. Epigenetic alterations	34
3.3. Cellular aging models	35
3.3.1. Oncogene-induced senescence (OIS)	36
3.3.2. <i>In vitro</i> aging	38
<u>HYPOTHESIS & OBJECTIVES</u>	<u>41</u>
<u>MATERIALS & METHODS</u>	<u>45</u>
1. Cell culture	47
1.1. Culture of Human Dermal Fibroblasts	47
1.2. Culture of Human BJ Fibroblasts	48
1.2.1. Senescence induction and detection	48
2. Cell treatments	49
2.1. DSB induction	49
2.1.1. γ -irradiation	49
2.1.2. Bleocin treatment	50
2.2. Trichostatin A and Nicotinamide treatment	50
3. Cell cycle analysis by flow cytometry	50
4. Generation of lentiviral particles	51
4.1. Cloning of shRNA sequences	53
4.2. Plasmid amplification and isolation	53
4.3. Diagnostic restriction enzyme digestion	54
4.4. Production of lentiviral particles	54
4.5. Infection of HDFs with lentiviral particles	56

5. Analysis of gene expression	56
5.1. Total RNA extraction	57
5.2. cDNA synthesis from total RNA	58
5.3. RT-qPCR	58
5.4. Data analysis	59
6. Chromatin immunoprecipitation (ChIP)-qPCR	59
7. Protein analysis	62
7.1. Western Blotting	62
7.1.1. Protein extraction for immunoblotting analysis	62
7.1.2. Immunoblotting	63
7.2. Immunocytochemistry	65
7.2.1. Cell fixation	65
7.2.2. Double immunofluorescence for γ H2AX and 53BP1	65
7.2.3. Triple immunofluorescence for γ H2AX, 53BP1 and H4K16Ac	66
7.2.4. Immunofluorescence analysis	68
8. Statistics	69
RESULTS	73
1. Establishment of aging models	75
1.1. Establishment of an oncogene-induced senescence model	75
1.2. Establishment of an <i>in vitro</i> aging model	79

2. Evaluation of H3K4ox in cellular aging models	81
2.1. Analysis of H3K4ox, <i>LOXL2</i> and <i>LOXL1</i> in OIS and <i>in vitro</i> aging	81
2.2. Analysis of H3K4ox in heterochromatin regions	83
3. Evaluation of H4K16 acetylation in cellular aging models	86
3.1. Analysis of H4K16Ac pattern in OIS	86
3.2. Analysis of H4K16Ac pattern during <i>in vitro</i> aging	88
4. Contribution of H4K16 acetylation to DSB repair in <i>in vitro</i> aging	90
4.1. H4K16 acetylation state after DSB induction	91
4.2. Analysis of H4K16Ac levels and its involvement in 53BP1 recruitment	95
4.3. Effects of H4K16 hyperacetylation on 53BP1 recruitment	100
4.4. Effects of H4K16 hypoacetylation on 53BP1 recruitment	103
DISCUSSION	111
1. Evaluation of cellular aging models	114
2. H3K4ox is an age-dependent epigenetic mark	116
3. Loss of H4K16 acetylation in OIS and in <i>in vitro</i> aging	118
4. Age-associated role of H4K16 acetylation in 53BP1 recruitment to DSBs	121

4.1. Age-related alterations in 53BP1 recruitment correlate with changes in H4K16Ac	122
4.2. A specific level of H4K16Ac is required for a proper 53BP1 recruitment	124
<u>CONCLUSIONS</u>	<u>129</u>
<u>REFERENCES</u>	<u>133</u>
<u>ANNEX I</u>	<u>159</u>
<u>ANNEX II</u>	<u>197</u>
<u>ACKNOWLEDGEMENTS</u>	<u>205</u>

Abstract

To efficiently maintain genome integrity cells have evolved an intricate signaling network termed as DNA damage response (DDR). A proper function of the DDR is required to repair deleterious DNA lesions, such as DNA double-strand breaks (DSBs). During *in vitro* and *in vivo* aging, a persistent accumulation of DSBs has been reported, suggesting a decline of the DNA repair mechanisms with age. Recent studies have highlighted the relevance of histone modifications in the regulation of the DDR. This is the case of the oxidation of H3 at lysine 4 (H3K4ox) and the acetylation of H4 at lysine 16 (H4K16Ac). The novel mark H3K4ox has been associated with the regulation of the DDR signaling. Regarding H4K16Ac, it has been related to DSB repair since its deacetylation is required for 53BP1 recruitment to DSB sites. Additionally, H4K16Ac varies during aging and cellular senescence. In this study we analyze the age-associated changes of these marks and their contribution to age-related DSB accumulation.

Although H3K4ox has been linked to heterochromatinization, our results showed a global reduction of H3K4ox in BJ fibroblasts displaying oncogene-induced senescence (OIS) and during *in vitro* aging of human dermal fibroblasts (HDFs). Accordingly, the expression levels of the oxidases *LOXL2* and *LOXL1* also suffered from a strong decrease in senescent fibroblasts while in *in vitro* aged HDFs only *LOXL1* expression was reduced. Nonetheless, we described how, although global levels of H3K4ox were reduced after OIS, they specifically increased in senescence-associated heterochromatin foci (SAHF). Hence, our findings suggest a relationship between heterochromatin regions and H3K4ox, conferring it a potential role in SAHF assembly and gene silencing during senescence.

Similarly to H3K4ox, a global reduction of H4K16Ac was found in both senescent BJ fibroblasts and *in vitro* aged HDFs in comparison to the levels of their control counterparts. Our results indicated that the decrease of H4K16Ac

was established through different molecular mechanisms in each process: while an increase in deacetylase activity was related to a higher expression of sirtuins in OIS, during *in vitro* aging the acetyltransferase activity was reduced due to decreased *MOF* expression.

Next, we analyzed the presence of 53BP1 at γ H2AX foci along with H4K16Ac levels in the whole nucleus before and after DSB induction in young and aged HDFs. In untreated *in vitro* aged cells, the decrease in H4K16Ac levels correlated with a reduction in 53BP1 recruitment to basal γ H2AX-labelled DSBs. Strikingly, following DSB induction, H4K16Ac slightly decreased in early passage HDFs while it increased in late passage HDFs. The same tendency was observed regarding 53BP1 recruitment to DSBs which prompted us to speculate that a relation might exist between H4K16Ac levels and efficient 53BP1 recruitment to DSBs. H4K16 hyperacetylation using both nicotinamide and trichostatin A failed to ameliorate the recruitment of 53BP1 to DSBs; instead, H4K16 hypoacetylation by *MOF* depletion impaired 53BP1 recruitment to γ H2AX-labelled DSBs. Thus, our results suggest that a specific H4K16Ac level should be reached for proper 53BP1 recruitment to DSBs.

In summary, we report H3K4ox as a promising age-associated epigenetic modification. Indeed, its specific enrichment in SAHF indicates a prominent role for H3K4ox in senescence. Regarding H4K16Ac, our data suggest that following DSB induction, H4K16Ac reaches a specific level required for the recruitment of 53BP1 to DSB sites. In young cells, this level is rapidly reached by slightly lowering their basal levels of H4K16Ac. However, aged cells start from lower basal levels of H4K16Ac that might impede them to reach the optimum H4K16Ac level for proper 53BP1 recruitment. Consequently, H4K16Ac stands as a key mark in the regulation of DSB repair during aging.

Resumen

El mantenimiento de la integridad del DNA es fundamental para evitar la aparición de mutaciones. Entre los diferentes tipos de daños en el DNA a los que la célula debe enfrentarse, destacan las roturas de la doble cadena del DNA (DSBs). La regulación de la respuesta al daño depende en gran medida del estado de la cromatina. En este sentido resultan de especial interés la oxidación de la histona 3 en la lisina 4 (H3K4ox) y la acetilación de la histona 4 en la lisina 16 (H4K16Ac). H3K4ox se ha relacionado recientemente con la señalización de la respuesta al daño. Por otro lado, la deacetilación de H4K16 es necesaria para el reclutamiento de 53BP1 a los DSBs. Además, se han descrito cambios en los niveles de H4K16Ac durante el envejecimiento y la senescencia. Considerando que los DSBs se acumulan con la edad, nos propusimos estudiar cómo los cambios de estas marcas durante el envejecimiento podrían contribuir a la reparación de DSBs.

A pesar de la relación entre H3K4ox y la condensación de la cromatina, se observó un descenso de los niveles globales de H3K4ox tras la inducción de senescencia por oncogenes (OIS) en fibroblastos BJ y durante el envejecimiento *in vitro* de fibroblastos humanos (HDFs). Asimismo, se determinó un descenso en la expresión de ambas oxidasas *LOXL2* y *LOXL1* en OIS y una disminución de *LOXL1* en HDFs envejecidos. Aunque los niveles globales de H3K4ox disminuyeron en OIS, el análisis de H3K4ox en los focos de heterocromatina asociados a la senescencia (SAHF) mostró un aumento de los niveles de oxidación en estas regiones cromatínicas específicas.

Los fibroblastos senescentes y los HDFs envejecidos *in vitro* mostraron también unos niveles de H4K16Ac más bajos que los de sus respectivas células control. Además, los bajos niveles de H4K16Ac respondían a un incremento en la expresión de las sirtuinas en OIS y a una reducción de la expresión de *MOF* durante el envejecimiento *in vitro*.

A continuación, se investigó cómo los cambios de H4K16Ac asociados al envejecimiento podrían afectar al reclutamiento de 53BP1 a los DSBs. Para ello se analizó la colocalización entre 53BP1 y γ H2AX y los niveles de H4K16Ac en HDFs jóvenes y envejecidos *in vitro* antes y después de la inducción de DSBs. En células no tratadas, el envejecimiento *in vitro* se correlacionó con una disminución de los niveles de H4K16Ac y con un menor reclutamiento de 53BP1 a los DSBs basales. Sin embargo, tras la inducción de DSBs, los niveles de H4K16Ac se redujeron ligeramente en los HDFs de pases tempranos y aumentaron en HDFs de pases más tardíos. El reclutamiento de 53BP1 siguió una tendencia similar a la descrita para H4K16Ac. Por lo tanto, tras la inducción de DSBs, H4K16Ac alcanzó un nivel estable, relacionado con un adecuado reclutamiento de 53BP1. Confirmando esta hipótesis, la hiperacetilación mediada por nicotinamida y tricostatina A no mejoró el reclutamiento de 53BP1. Además, la hipoacetilación de H4K16 mediante el silenciamiento de *MOF* se tradujo en una disminución de la colocalización entre 53BP1 y γ H2AX.

Nuestros resultados señalan a H3K4ox como una marca epigenética asociada al envejecimiento especialmente relevante en senescencia. Además, describimos que, tras la inducción de DSBs, H4K16Ac alcanza unos niveles concretos, necesarios para el reclutamiento de 53BP1 a los DSBs. Las células jóvenes alcanzan este nivel rápidamente disminuyendo sus niveles basales de acetilación. Sin embargo, la consecución de dicho nivel puede verse dificultada en células envejecidas, ya que parten de niveles basales de H4K16Ac considerablemente inferiores. Por lo tanto, H4K16Ac se erige como una marca clave en la regulación de la reparación de los DSBs durante el envejecimiento.

Abbreviations

4-OHT	4-hydroxytamoxifen
53BP1	p53 binding protein 1
ATM	Ataxia-telangiectasia mutated
BACH1	Transcription regulator protein BACH1
bp	Base pair
BRCA_	Breast cancer type _ susceptibility protein
BSA	Bovine serum albumin
cDNA	Complementary deoxyribonucleic acid
ChIP	Chromatin immunoprecipitation
Ct	Threshold cycle
CTCF	Corrected total cell fluorescence
CtIP	CtBP-interacting protein
DAPI	4',6-diamidino-2-phenylindole
DDR	DNA damage response
DMEM	Dulbecco's modified eagle medium
DMSO	Dimethyl sulfoxide
DNA	Deoxyribonucleic acid
DNA-PKcs	DNA-dependent protein kinase catalytic subunit
DNase	Deoxyribonuclease
DSB	Double strand break
EDTA	Ethylenediaminetetraacetic acid
EP	Early passage
ER	Estrogen receptor
F	Forward
FBS	Fetal bovine serum
FC	Fold change
H2AK13ub	Ubiquitination of H2A at lysine 13
H2AK15ub	Ubiquitination of H2A at lysine 15

H3K4me3	Trimethylation of H3 at lysine 4
H3K9me3	Trimethylation of H3 at lysine 9
H4K16Ac	Acetylation of H4 at lysine 16
H4K20me2	Dimethylation of H4 at lysine 20
HATs	Histone acetyltransferases
HBS	Hepes buffered saline
HDACs	Histone deacetylases
HDFs	Human dermal fibroblasts
IP	Immunoprecipitation
Ku70	70 kDa subunit of Ku antigen
Ku80	86 kDa subunit of Ku antigen
LADs	Lamina-associated domains
LOXL_	Lysyl oxidase like_
LP	Late passage
MDC1	Mediator of DNA damage checkpoint 1
MOF	Males absent on the first
MRE11	Meiotic recombination 11
mRNA	Messenger ribonucleic acid
NAM	Nicotinamide
NBS1	Nijmegen breakage syndrome 1
OIS	Oncogene-induced senescence
p53	Cellular tumor antigen p53
PBS	Phosphate buffered saline
PCNA	Proliferating cell nuclear antigen
PFA	Paraformaldehyde
PI	Post-irradiation
PIKK	Phosphatidylinositol 3-kinase-like proteins
Pol_	DNA polymerase
PTMs	Post-translational modifications
R	Reverse

RAD50	DNA repair protein RAD50
RAD51	DNA repair protein RAD51 homolog 1
RAD54	DNA repair and recombination protein RAD54-like
RAP80	Receptor-associated protein 80
Rb	Retinoblastoma-associated protein
RIF1	Rap1-interacting factor 1 homolog
RNA	Ribonucleic acid
RNase	Ribonuclease
RPA	Replication protein A
RT	Room temperature
RT-qPCR	Reverse transcription quantitative-polymerase chain reaction
SAHF	Senescence-associated heterochromatin foci
shRNA	Short hairpin RNA
SIRT_	Sirtuins
TOPBP1	DNA topoisomerase 2-binding protein 1
TSA	Trichostatin A
TTBS	Tween-Tris-buffered saline
XLF	XRCC4-like factor
XRCC_	X-ray repair cross-complementing protein
γH2AX	H2AX phosphorylation on serine 139





Introduction

1. DNA damage

Cells are continuously facing endogenous and exogenous stresses that can ultimately lead to DNA damage. These lesions can block DNA replication and transcription, and if they are not repaired or are repaired incorrectly, they can cause mutations or large-scale genome aberrations that threaten genomic integrity and cell viability (Jackson and Bartek, 2009). To combat threats presented by DNA damage, cells have evolved defense mechanisms collectively termed as DNA damage response (DDR). The DDR can act through different DNA repair pathways, depending on the type and relevance of the DNA lesion (Harper and Elledge, 2007; Jackson and Bartek, 2009).

1.1. Sources and types of DNA lesions

DNA damage results from either endogenous sources (produced during normal cell metabolism) or exogenous sources (they come from the environment) (**Figure 1**). Endogenous sources of DNA damage include hydrolysis, oxidation, alkylation and mismatch of DNA bases. For instance, deamination of cytosine, adenine, guanine or 5-methylcytosine converts these bases to the miscoding uracil, hypoxanthine, xanthine and thymine, respectively. In addition, products derived from oxidative respiration and lipid peroxidation (reactive oxygen species) constitute permanent enemies of genome integrity (Hoeijmakers, 2001; Shiloh, 2003). Regarding exogenous sources of DNA, environmental agents such as ultraviolet and ionizing radiation or numerous genotoxic chemicals produce alterations in the DNA structure (Hoeijmakers, 2001).

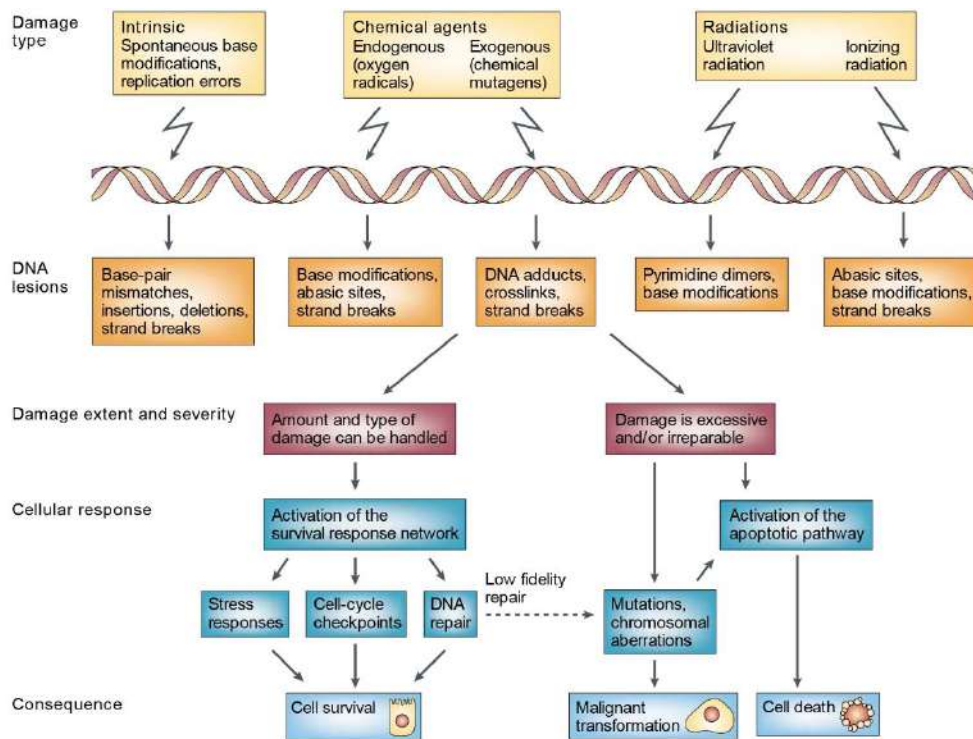


Figure 1. Different sources of DNA damage cause different lesions. Overview of the DNA-damaging agents and examples of DNA lesions induced by these agents. In the lower part, the possible cellular responses against DNA damage depending on the type, amount and severity of DNA lesions (Shiloh, 2003). Picture reproduced with permission from the copyright owner.

The different DNA damage sources can generate a wide variety of DNA lesions that range from double strand breaks (DSBs), single strand breaks (SSBs), excision of nucleotides to unions DNA-protein and DNA-DNA (Pagès and Fuchs, 2002). Among the diversity of DNA lesions, the most deleterious ones are the DSBs as their incorrect repair could result into deletions, translocations, dicentrics and other genomic rearrangements (Misteli and Soutoglou, 2009). These DNA alterations might drive the activation of proto-oncogenes or the inactivation of tumor-suppressor genes (Hoeijmakers, 2001; Shiloh, 2003). Consequently, accumulation of DSBs has been associated with cancer (Aplan, 2006; Aparicio et al., 2014) and aging (Gorbunova and Seluanov, 2016; White and Vijg, 2016).

1.2. DNA damage response

To properly protect the genome, the DDR, through the action of sensors, mediators, and effectors, orchestrates the appropriate repair of DNA damage. This hierarchical pathway begins with the detection of the DNA lesion by the sensor proteins which subsequently activate the mediators. Then, mediators amplify the signal and transduce it to the effectors. Finally, effectors inhibit cell cycle progression and repair the damage. If the lesion is too complex to be efficiently repaired, effectors induce programmed cell death (apoptosis) or senescence (Shiloh, 2003; Bree et al., 2004; Harper and Elledge, 2007).

1.2.1. Recognition and signaling of DSBs

DSB recognition is accomplished by the MRE11/RAD50/NSB1 (MRN) complex. Immediately after the generation of a DSB, the MRN complex is recruited to the DNA damage site (Lavin, 2007). Once the complex finds a DSB, ataxia telangiectasia mutated (ATM), the main protein involved in the DDR signal amplification is recruited to the C-terminus of NBS1 (Berkovich et al., 2007; Stracker et al., 2007). ATM is a serine-threonine protein kinase that belongs to the family of the phosphatidylinositol 3-kinase-like proteins (PIKKs) (Lempiäinen and Halazonetis, 2009; Lovejoy and Cortez, 2009). The interaction with the MRN complex stimulates ATM kinase activity which is required for optimal ATM signaling in cells (Uziel et al., 2003; Blackford and Jackson, 2017). Once ATM is recruited to the DSB site, ATM phosphorylates itself, an event that results in its transition from an inactive dimer into active monomers (**Figure 2A**) (Bakkenist and Kastan, 2003).

Following its activation, ATM phosphorylates the serine 139 of histone H2AX, which is referred as γ H2AX (Rogakou et al., 1998; Paull et al., 2000; Burma et al., 2001). This phosphorylation is needed for the recruitment of the mediator of damage-checkpoint 1 (MDC1), which stabilizes the MRN complex at the break site and amplifies ATM-mediated signaling (**Figure 2A**) (Lukas et al., 2004; Stucki et al., 2005). Indeed, the recruitment of MDC1 to the γ H2AX

proximal to the lesion promotes a positive feedback for the recruitment and retention of more activated ATM. Then, ATM phosphorylates more H2AX molecules that are located more distal to the initial break. Hence, the γ H2AX mark spreads over larger chromatin domains (Lou et al., 2006; Stucki and Jackson, 2006; Jungmichel and Stucki, 2010). The spreading of γ H2AX provides a platform for the recruitment of additional repair proteins and chromatin modifying enzymes (Bekker-Jensen and Mailand, 2010; Nakamura et al., 2010).

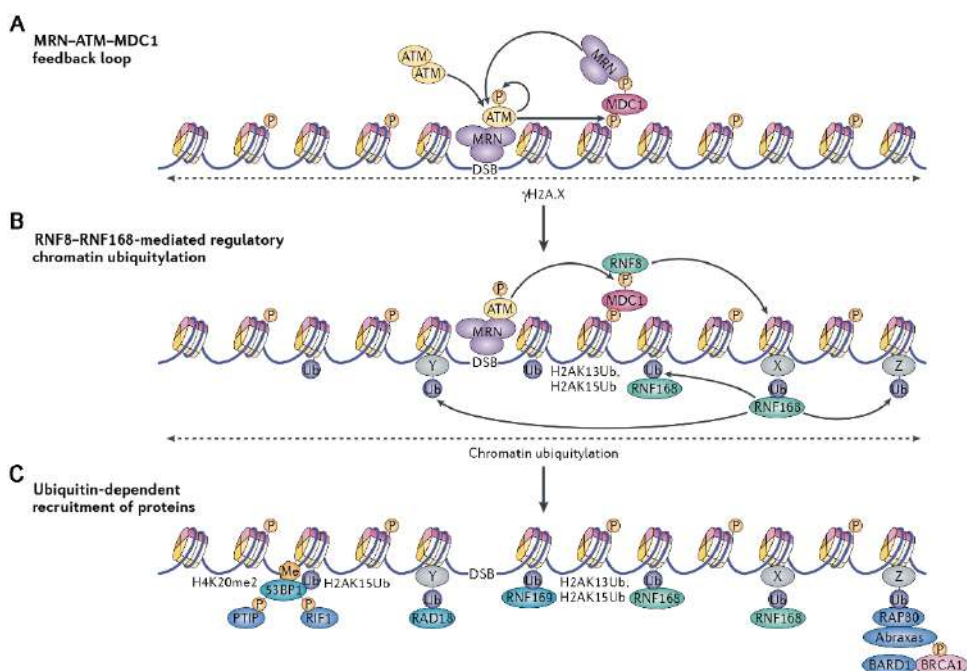


Figure 2. ATM-mediated signaling cascade of DSBs. Schematic representation of the recruitment of proteins involved in the recognition and signaling of DSBs (Panier and Durocher, 2013). Picture reproduced with permission from the copyright owner.

Subsequently, MDC1 recruits the ubiquitin E3 ligases RNF8 and RNF168 which catalyze the ubiquitylation of H2A at the DSB sites (**Figure 2B**). The concerted action of these enzymes promotes the focal accumulation of downstream DNA repair proteins such as p53 binding protein 1 (53BP1) or breast cancer type 1 susceptibility protein (BRCA1) that will determine the DNA

repair pathway choice (**Figure 2C**) (Mailand et al., 2007; Polo and Jackson, 2011; Mattioli et al., 2012).

1.2.2. DSB repair pathways

The two major DSB repair pathways are the homologous recombination (HR) and the nonhomologous end joining (NHEJ) pathways (Helleday et al., 2007). HR requires a sister chromatid as a template to provide a precise copy of the damaged sequence. Hence, HR is restricted to the S and G2 phases of the cell cycle when the DNA duplication has occurred. On the contrary, NHEJ does not need a homologous template to repair the DNA lesion and thereby, it is active throughout the cell cycle. During the NHEJ, ends of the breaks can be directly ligated after slight processing to create short homology stretches (1-6 bp). Thus, NHEJ is faster than HR, but more prone to errors, since it uses short homologous DNA sequences for repair instead of the large templates used by HR. The balance between both repair mechanisms is highly regulated and essential for genome stability (Shaltiel et al., 2015; Hustedt and Durocher, 2017; Her and Bunting, 2018).

a. Nonhomologous end joining (NHEJ)

The NHEJ is the predominant DSB repair pathway throughout the cell cycle. NHEJ modifies the broken DNA ends to make them compatible and ligates them together with no-to-little regard for homology (Weterings and Chen, 2008). Although the NHEJ acts on a wide variety of DNA-end configurations, the resulting repaired DNA junctions can often contain mutations (Chang et al., 2017).

The first step in the NHEJ is the recognition of the DSB by the Ku protein which is a heterodimer composed of two subunits: Ku70 and Ku80. Ku binds to the broken DNA ends in a sequence-independent manner and forms a ring that encircles the broken DNA. Then, Ku aligns the DNA ends and protects them from degradation (**Figure 3A**) (Downs and Jackson, 2004; Grundy et al., 2016).

Subsequently, Ku functions as a recruitment platform for the DNA dependent protein kinase catalytic subunit (DNA-PKcs) to the DSB site. Ku is translocated allowing two DNA-PKcs molecules to interact with each end of the broken DNA forming the so-called “synaptic complex (**Figure 3B**). Once assembled, the DNA-PKcs-Ku-DSB complex allows to keep close together the ends of the DSB and to protect them from nucleases attack (DeFazio et al., 2002; Weterings and van Gent, 2004). The interaction between the two DNA-PKcs molecules stimulates their kinase activity, promoting both their self-phosphorylation and the phosphorylation of other downstream repair substrates (Jette and Lees-Miller, 2015).

Following the detection of the DNA ends, the next step consists of processing the DNA termini to remove blocking end groups and fill in the gaps (Mahaney et al., 2009; Pannunzio et al., 2018). One of the nucleases involved in this procedure is Artemis that possesses 5'-3' exonuclease activity and also DNA-PKcs-dependent endonuclease activity. These characteristics makes Artemis able to cut DNA ends at single-strand to double-strand DNA boundaries, which includes all overhangs and other structures such as loops (**Figure 3C**) (Ma et al., 2002; Pannicke et al., 2004). After the nuclease's actions, the resulting DNA gaps are filled by the DNA polymerases. Members of the DNA pol X family of DNA polymerases, Pol μ and Pol λ are responsible for the addition of nucleotides to finally generate blunt ends (Ramsden, 2011). While nucleotide insertion by Pol λ is generally template-dependent, insertion by pol μ appears to be template-

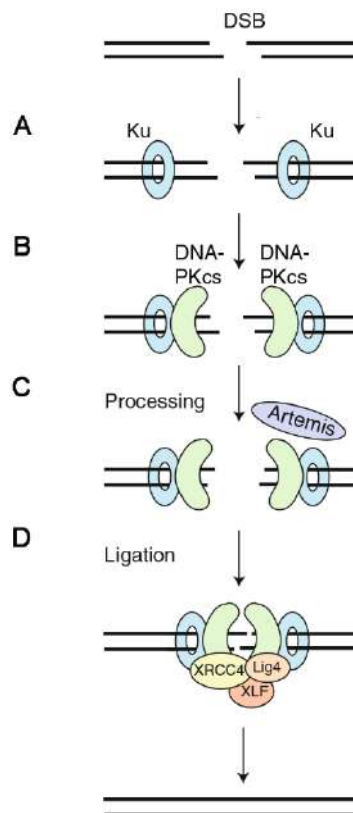


Figure 3. Overview of the NHEJ pathway. Modified picture from Brandsma and Gent, 2012 with permission from the copyright owner.

independent which could ultimately lead to errors in the repair process (Nick McElhinny et al., 2005).

Finally, the modified DNA ends must be ligated to repair the DNA. Ligation is mainly carried out by DNA ligase IV, which exists in complex with the X-ray repair cross complementing protein 4 (XRCC4) (**Figure 3D**) (Mahaney et al., 2009). XRCC4 stabilizes the DNA ligase IV and stimulates its activity to complete the DSB repair (Grawunder et al., 1998). The activity of the XRCC4-DNA ligase IV complex is also enhanced by other proteins such as XRCC4-like factor (XLF, also named Cernunnos) (Ahnesorg et al., 2006; Bhargava et al., 2018) or the paralog of XRCC4 and XLF (PAXX) (Craxton et al., 2015; Tadi et al., 2016).

b. Homologous recombination (HR)

Since it requires a homologous sister chromatid as a template for repair, HR is a largely error-free process. Thus, it operates exclusively in post-replicative chromatin during S and G2 phases of the cell cycle (Shaltiel et al., 2015; Hustedt and Durocher, 2017; Her and Bunting, 2018).

HR is initiated by the resection of DNA ends which generates extended regions of SSBs. For this purpose, MRN complex promotes end clipping via the 3'-5' endonuclease activity of MRE11 in close proximity to the break site (Paull and Gellert, 1998). This DNA degradation is followed by a limited 5'-3' resection mediated by CtBP-interacting protein (CtIP) (**Figure 4A**) (Sartori et al., 2007). These sequential resections result in a 3' SSB overhang that is rapidly coated by the replication protein A (RPA) to protect it from nucleolytic degradation (**Figure 4B**) (Zou et al., 2006; Pokhrel et al., 2017).

To promote the repair of the break, RPA is subsequently displaced from the SSB and exchanged with the DNA repair protein RAD51 homolog 1 (RAD51) (San Filippo et al., 2008; Symington, 2016). RAD51 binding to the SSBs is enhanced by mediator proteins, including breast cancer type 2 susceptibility protein (BRCA2) and the RAD51 paralogues (Figure 4C) (Suwaki et al., 2011). Then, the resulting RAD51 nucleoprotein filament performs homology search and strand invasion. Once the homologous sequence is found, RAD51 promotes the exchange of DNA strands that leads to formation of joint molecules (D-loops) with a Holliday junction at the end (Figure 4D) (Baumann et al., 1996). To stimulate the formation of the D-loop, RAD51 interacts with the DNA repair and recombination protein RAD54-like (RAD54) to increase the stability of the heteroduplex (Solinger et al., 2001; Mazin et al., 2010).

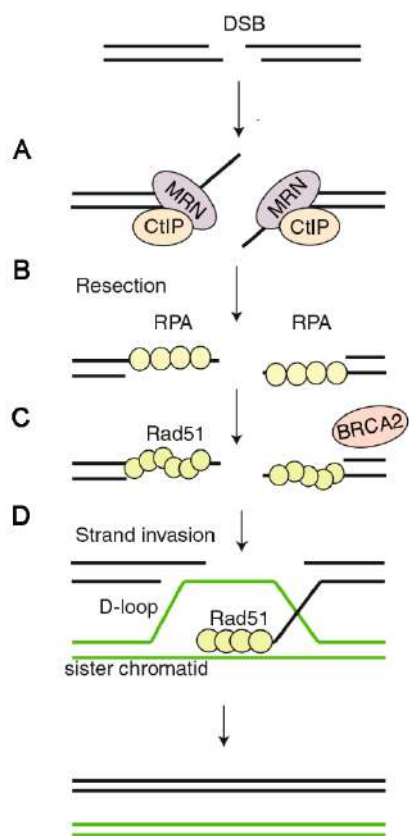


Figure 4. Overview of the HR pathway. Modified picture from Brandsma and Gent, 2012 with permission from the copyright owner.

Following strand invasion, de novo DNA synthesis occurs within the D-loop. From the several polymerases involved in this process, polymerase δ (Pol δ) has emerged as the major player. The DNA synthesis by Pol δ is greatly stimulated by the proliferating cell nuclear antigen (PCNA) which also regulates the length of the extension (Maloisel et al., 2008; Li et al., 2009). Finally, the Holliday junction resolution is performed by the bloom syndrome protein (BLM) helicase and the topoisomerase II α to end the repair process and restore the

chromosomes back to their original state (Wu and Hickson, 2003; Russell et al., 2011).

c. Choice between NHEJ and HR

The mechanisms that govern whether a DSB is repaired by NHEJ or HR are tightly regulated. As mentioned before, when DSBs occur, the cell cycle phase has a major influence on the choice of the repair pathway. The cell cycle-dependent performance of NHEJ and HR is regulated by the antagonistic proteins 53BP1 and BRCA1. The recruitment of 53BP1 to DSB regions occurs preferably during the G1 phase of the cell cycle and inhibits HR by blocking DNA resection. On the other hand, BRCA1 binds to the DSBs preferentially during S and G2 phases of the cell cycle, displacing 53BP1 to the focal periphery. Consequently, an overall reduction of 53BP1 occupancy at DNA damage sites takes place, promoting DNA resection and repair through the HR (Chapman et al., 2012; Escribano-Díaz et al., 2013).

53BP1 recognizes the ubiquitinated H2A on lysine 15 (H2AK15ub) at the DSB and is recruited through its ubiquitination-dependent recruitment (UDR) motif (Fradet-Turcotte et al., 2013; Panier and Boulton, 2014). 53BP1 binding to the chromatin also requires the recognition of the dimethylated histone H4 on lysine 20 (H4K20me2) via its Tudor domain (**Figure 5A**) (Botuyan et al., 2006). The affinity of 53BP1 for H4K20me2 is modulated by the acetylation of lysine 16 of the same histone H4 (H4K16Ac). Indeed, H4K16Ac reduces 53BP1 binding to H4K20me2 by disrupting a salt bridge that is necessary for the association of the Tudor domain with the H4 (**Figure 5B**) (Hsiao and Mizzen, 2013; Tang et al., 2013).

Apart from the recruitment of 53BP1 to DSBs, phosphorylation of 53BP1 by ATM is also required for the anti-HR role of 53BP1 (Bothmer et al., 2011; Feng et al., 2015). ATM-dependent phosphorylation of 53BP1 is necessary for the recruitment of the principal effector of 53BP1: RAP1-interacting factor 1 (RIF1). RIF1 prevents 5' end resection at DSBs by inhibiting the recruitment of BRCA1 during G1, thus promoting repair through the 53BP1-dependent NHEJ pathway (**Figure 5A**) (Chapman et al., 2013; Di Virgilio et al., 2013; Escribano-Díaz et al., 2013; Feng et al., 2013; Zimmermann et al., 2013).

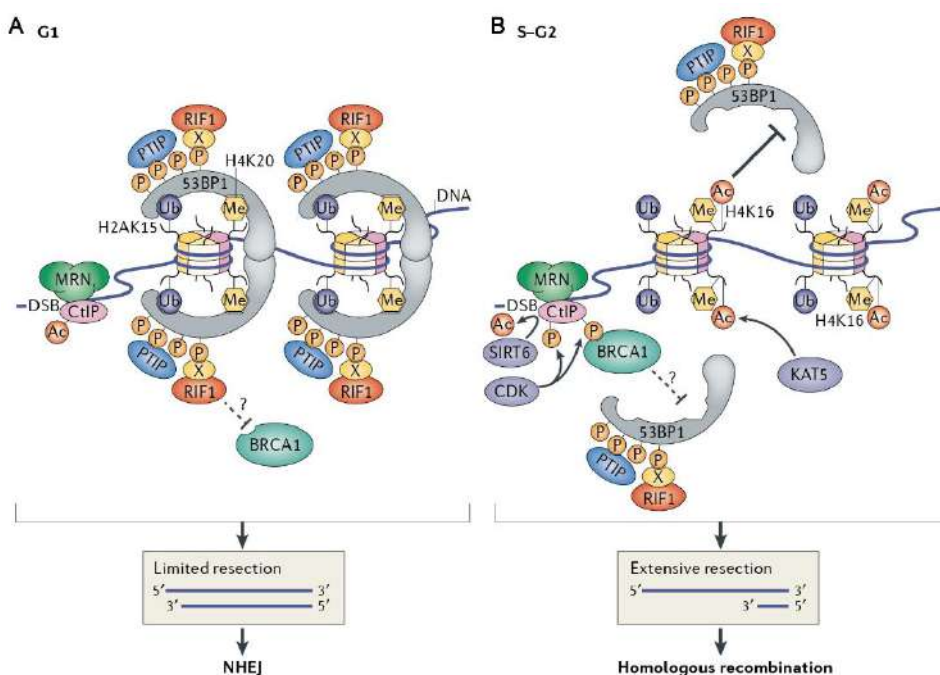


Figure 5. Antagonistic relationship between 53BP1 and BRCA1 during DSB repair pathway choice. (A) During G1, 53BP1 binds to H2AK15ub and H4K20me2 and recruits its effector protein RIF1, conducting repair to NHEJ. (B) During S phase, CtIP promotes its binding to BRCA1 and prevents association of 53BP1–RIF1. Additionally, H4K16ac reduces 53BP1 binding to the H4K20me2 mark, allowing DNA end resection and repair through the HR pathway. Modified picture from Panier and Boulton, 2014 with permission from the copyright owner.

As cells transition from G1 to S phase, recruitment of BRCA1 functions as a molecular switch to shift the balance from NHEJ to HR. Recently, it has been shown that BRCA1 recruitment requires recognition of histone H4 unmethylated at lysine 20 (H4K20me0). During S phase, H4K20me0 is

incorporated on newly synthesized DNA and mixed with old nucleosomes methylated at H4K20. Thereby, recruitment of BRCA1 by H4K20me0 recognition links DSB repair pathway choice directly to sister chromatid availability (Nakamura et al., 2019). Apart from the novel role of BRCA1 as a sensor of the cell-cycle phase, BRCA1 is also a key component of at least four complexes (BRCA1A to BRCA1D) (**Figure 6**) (Her et al., 2016). Together with BRCA1, the major components of the BRCA1-A complex are the receptor-associated protein 80 (RAP80) and the adaptor protein Abraxas (Wang et al., 2007). Abraxas directly interacts with BRCA1 and links it to other components of the BRCA1-A complex, such as RAP80. The BRCA1-Abraxas-RAP80 interaction allows the recruitment of BRCA1 to the DSBs, since RAP80 recognizes the poly-ubiquitin chains of the H2AX at the damage sites (Sobhian et al., 2007; Wang et al., 2007; Yan et al., 2007).

Once BRCA1 is recruited to the DSBs, CtIP is phosphorylated by cyclin-dependent kinases (CDKs) and it subsequently interacts with BRCA1 forming the BRCA1-C complex (Yu and Chen, 2004). Through its interaction with BRCA1, activated CtIP promotes DNA end resection. (Sartori et al., 2007). In addition, BRCA1-C complex inhibits the recruitment of RIF to DSBs thus blocking the NHEJ (Chen et al., 2008; Huertas and Jackson, 2009; Escribano-Díaz et al., 2013). Then, BRCA1 associates with BRCA2 and RAD51, among other factors, to form BRCA1-D complex, which stimulates RAD51 recruitment and promotes efficient HR (Sy et al., 2009; Zhang et al., 2009).

Finally, the last of the complexes, BRCA1-B, is composed of BRCA1, topoisomerase 2-binding protein 1 (TOPBP1) and transcription regulator protein (BACH1). This complex plays a role in DNA replication stress-induced checkpoint but its precise function is still unknown (Mäkiniemi et al., 2001; Kumaraswamy and Shiekhattar, 2007; Roy et al., 2011).

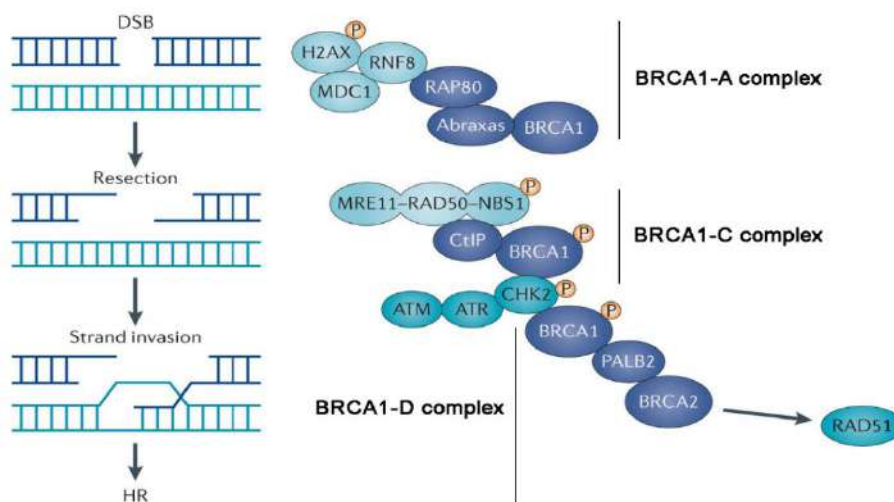


Figure 6. Multiple BRCA1-containing complexes. Schematic representation of the different BRCA1 complexes and their respective functions during the HR. Modified picture from Roy et al., 2011 with permission from the copyright owner.

2. Chromatin dynamics in response to DNA damage

The processes related to DNA recognition and repair are orchestrated within the layers of chromatin (Krishnan et al., 2011a). The past several years have provided important insights into the role of chromatin remodeling and histone modifications to control DNA damage sensing, signaling and repair (Pandita and Richardson, 2009). Indeed, the chromatin state can determine the accessibility of the repair proteins to the damaged DNA (Sabarinathan et al., 2016) or the ability to properly activate the DDR (Misteli, 2007).

2.1. Chromatin structure

The basic and repeating structural units of chromatin are the nucleosomes that comprise about 147 base pairs of DNA wrapped around eight histone proteins assembled in an octameric core (Luger et al., 1997; Kornberg and Lorch, 1999). Each histone octamer is formed by two copies of histone 2A (H2A), histone 2B (H2B), histone 3 (H3) and histone 4 (H4). Protruding from the core of the nucleosomes, there are particular domains termed histone tails which are the

N-terminal regions of these proteins (Strahl and Allis, 2000; Jenuwein and Allis, 2001). The histone tails are crucial for nucleosome biology since their post-translational modifications (PTMs) confer them specific functionality (Kouzarides, 2007; Lawrence et al., 2016). Nucleosomes are connected by a DNA linker of variable length (20-90 bp) which is bound to histone 1 (H1). The length and the structure of the DNA linker also regulates the accessibility to the surrounding DNA (Bednar et al., 1998).

When viewed under an electron microscope, thousands of nucleosomes joint by the DNA linker form the next level of chromatin organization, which is known as the 10 nm beads-on-a-string fiber (Olins and Olins, 2003). Subsequently, this fiber is further coiled into a thicker and shorter structure called the 30 nm chromatin fiber. Lastly, the interaction between overcrowded and randomly placed nucleosomal arrays produce tertiary chromatin conformations, like such observed in mitotic chromosomes (**Figure 7**) (Eltssov et al., 2008; Maeshima et al., 2010).

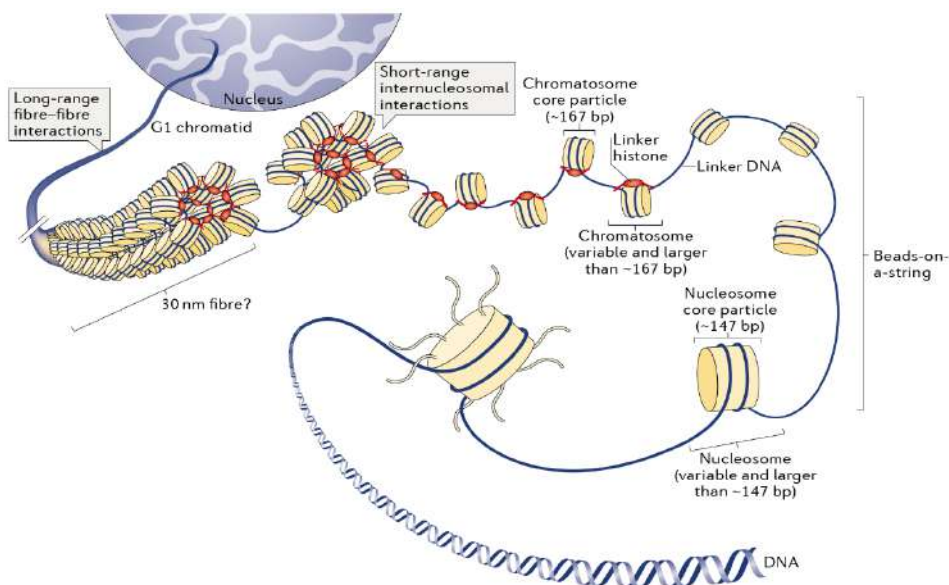


Figure 7. Chromatin structural levels. Hierarchical levels of DNA packaging, which range from the basic unit of chromatin, the nucleosome, to the highest degree of compaction, the chromosome (Fyodorov et al., 2017). Picture reproduced with permission from the copyright owner.

Apart from being compacted enough to fit inside the nucleus, DNA sequences should be accessible to transcription factors and DNA repair machinery when needed. This requirement distinguishes two chromatin domains in interphase: euchromatin and heterochromatin. Euchromatin is less condensed, gene enriched, transcriptionally permissive and the first region to be replicated during early S phase (Gilbert et al., 2004). Conversely, heterochromatin is tightly condensed, gene poor, transcriptionally inactive and it replicates in late S phase (Becker et al., 2016).

The organization of DNA into chromatin fibers complicates its accessibility to the DNA repair machinery which has to overcome this physical barrier to access the DNA lesion and repair it. Several studies have demonstrated that the chromatin undergoes enormous changes in the surroundings of a DSB (Kruhlak et al., 2006; Luijsterburg and van Attikum, 2011; Goodarzi and Jeggo, 2012). For instance, following DSB induction, ATM phosphorylates its effector protein KAP-1 which is rapidly diffused throughout the chromatin allowing an efficient induction of chromatin relaxation on a global scale (Ziv et al., 2006). Additionally, both the size and the expansion of γ H2AX are reduced in heterochromatic regions compared to euchromatic areas (Karagiannis et al., 2007; Kim et al., 2007). Interestingly, recent studies have shown that proteins classically related to chromatin compaction, such as HP1 and histone deacetylases can be recruited to DSB sites (Miller et al., 2010; Baldeyron et al., 2011). Therefore, the chromatin structure changes after DNA damage can lead to both relaxation and compaction of chromatin, depending on the type of lesion and time post DNA damage (Goodarzi and Jeggo, 2012).

2.2. Post-translational modifications of histones

As mentioned, chromatin structure should be dynamic and capable of regulating unfolding-folding transitions to guarantee the access of DNA repair proteins to the lesions. In order to modulate nucleosome dynamics and ultimately gene expression, post-translational modifications (PTMs) of the

histone tails represent an exquisite mechanism for regulating chromatin state (Kouzarides, 2007; Lawrence et al., 2016). There are numerous PTMs described in different residues of the histone tail. The more characterized ones are acetylations, methylations and phosphorylations. Nevertheless, several others, such as ubiquitinations, sumoylations, butyrylation and oxidations have been described (**Figure 8**) (Kouzarides, 2007; Lawrence et al., 2016).

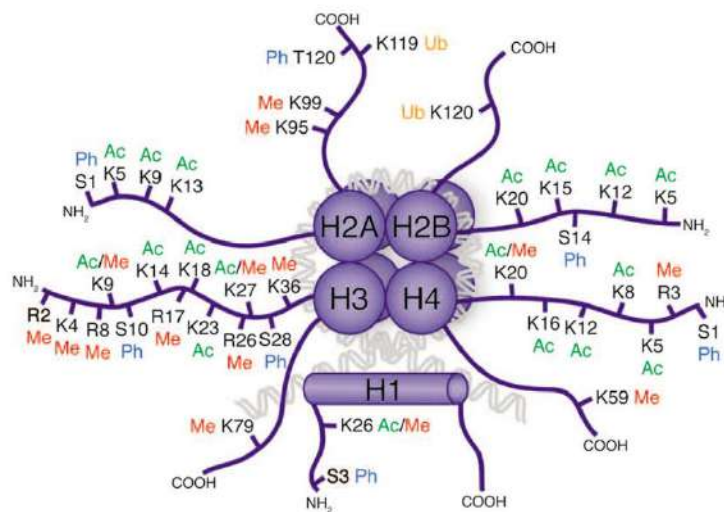


Figure 8. Schematic drawing of a nucleosome. Histone octamer with the post-translational modifications highlighted on the terminal tails of each histone (Tollervey and Lunyak, 2012). Picture reproduced with permission from the copyright owner.

The nature of the PTMs may determine the degree of chromatin compaction, establishing euchromatin or heterochromatin regions. For instance, histone acetylations have been historically linked to open chromatin, whereas, histone methylations have been associated with closed chromatin. However, these concepts are somehow outdated since the code is far more complex than previously established and the role of a specific histone modification strongly depends on the context (Sims and Reinberg, 2008; Smith and Shilatifard, 2010). Additionally, the interplay between PTMs adds a new level of complexity to the chromatin signaling pathway. Indeed, a cross-talk can be established

between modifications in the same histone tail (cis) or between different histone tails belonging to the same nucleosome (trans) (Venne et al., 2014).

The relevance of PTMs in the DDR is exemplified by their roles in the initiation and execution of these cellular processes. Among the wide variety of PTMs involved in the DDR, the most studied one is the phosphorylation of the histone variant H2AX (γ H2AX) which is triggered by DSB generation (Rogakou et al., 1998; Paull et al., 2000; Burma et al., 2001). Another well-characterized example is the ubiquitination of H2A on lysine 13 and lysine 15 (yielding H2AK13ub and H2AK15ub, respectively), that are required for the recruitment of 53BP1 to DSBs (Mailand et al., 2007; Polo and Jackson, 2011; Mattioli et al., 2012). Multiple PTMs are related to the DDR; however, the following sections will focus on two histone marks that are essential for this thesis.

2.2.1. Histone acetylation

Histone acetylation involves the addition of an acetyl group to the N-terminus of a lysine, forming an amide bond. In non-acetylated conditions, the positive charge of the lysine chain binds tightly to the negative charge of the DNA, resulting in a closed structure. Thus, acetylation of lysine removes the positive charge and reduces the interaction (Bannister and Kouzarides, 2011). For this reason, acetylation is associated with relaxed chromatin state that facilitates active transcription, while hypoacetylation is related to condensed chromatin and repressed transcription (Gorisch et al., 2005).

The enzymes responsible for histone acetylation are the histone acetyltransferases (HATs). HATs are classified into four families depending on their homology: GNAT, MYST, p300/CBP and SRC (**Figure 9**) (Sternier and Berger, 2000). On the other hand, the enzymes in charge of the removal of the acetyl group are the histone deacetylases (HDACs). HDACs are divided into four groups depending on their location and homology: classes I, II and IV, that require zinc ion as a cofactor; and class III, also called sirtuins, that require NAD⁺ as cofactor (**Figure 9**) (de Ruijter et al., 2003; Michan and Sinclair,

2007). HDAC activity can be inhibited by HDAC inhibitors (HDACi). HDACi of classes I, II and IV HDACs contain a zinc binding group which interacts with the corresponding catalytic site of the HDACs. Among these types of HDACi, trichostatin A (TSA), sodium butyrate (NaB) and suberoylanilide hydroxamic acid (SAHA) are the best characterized (Kim and Bae, 2011). However, sirtuins (class III HDACs) are not sensitive to these HDACi. For these enzymes the most well-known inhibitor is nicotinamide (NAM) that interacts with a reaction intermediate of the NAD⁺-dependent deacetylation performed by sirtuins (Avalos et al., 2005).

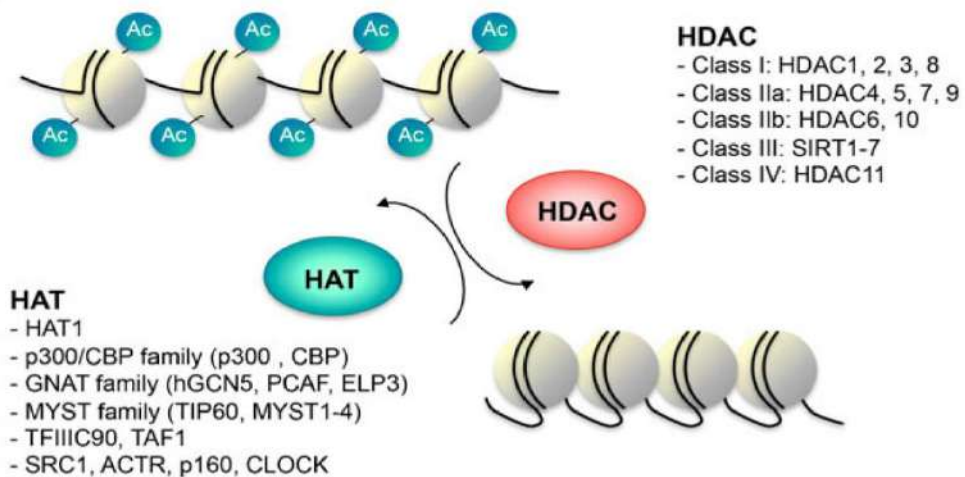


Figure 9. Different families and classes of HATs and HDACs. Picture reproduced from Schneider et al., 2013 with permission from the copyright owner.

Acetylation of histone 4 at lysine 16 (H4K16Ac)

H4K16Ac is an important mark of actively transcribed genes from yeast to humans (**Figure 10**). *In vitro* studies have shown that H4K16Ac reduces the nucleosome-nucleosome interaction and inhibits the formation of the 30 nm chromatin fibers (Shogren-Knaak, 2006; Shogren-Knaak and Peterson, 2006). Its role as an inhibitor of chromatin compaction reinforces the cell cycle-related variations of H4K16Ac. Specifically, H4K16Ac peaks during S phase, when the chromatin structure has to be open, and decreases at G2/M reaching its lowest

level during mitosis, when chromosome formation takes place (Vaquero et al., 2006).

The relevance of H4K16Ac goes beyond its role in the maintenance of the chromatin structure since it also serves as a signal to promote or inhibit protein binding to the chromatin. To this extend, loss of acetylation at H4K6 is a common hallmark of human cancer and it has been related to defects on differentiation, cell cycle regulation or DNA damage repair (Fraga and Esteller, 2007).

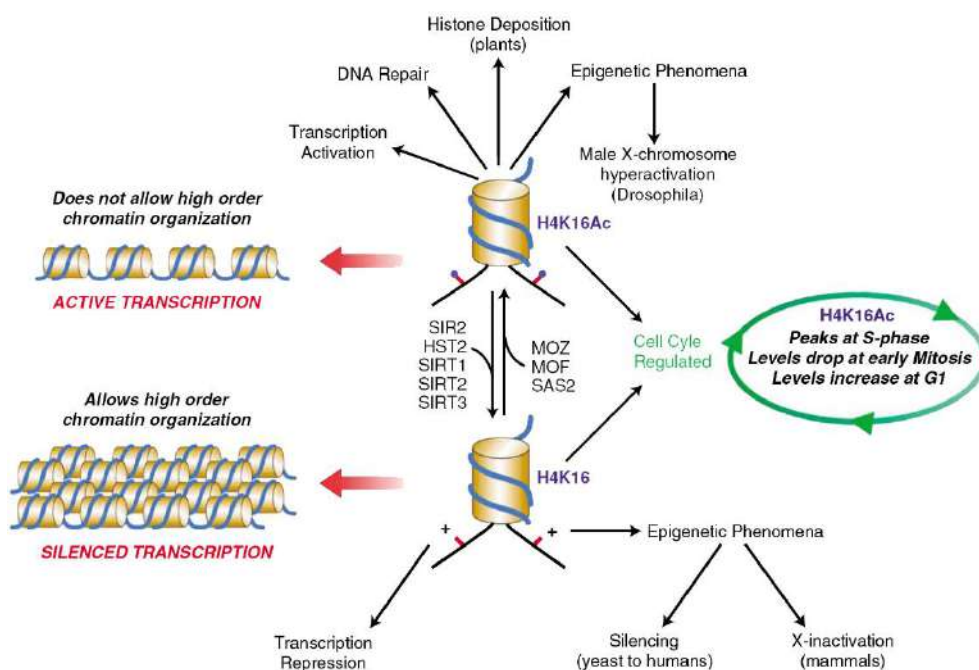


Figure 10. Overview of the multiple roles of H4K16Ac in chromatin regulation throughout evolution. Picture reproduced from Vaquero et al., 2007 with permission from the copyright owner.

The major enzyme in charge of H4K16 acetylation is the so-called Males absent on the first (MOF) (Smith et al., 2005; Taipale et al., 2005). MOF is a member of the MYST family of HATs and is critical for the DSB repair. In this line, MOF depletion leads to the abrogation of the ATM-dependent phosphorylation of DNA-PKcs (Sharma et al., 2010). In addition, MOF depletion also leads to the

complete abolishment of MDC1 recruitment and its downstream signaling proteins 53BP1 and BRCA1 to DSB sites (Li et al., 2010). Hence, MOF is indispensable for both NHEJ and HR DSB repair pathways. Apart from MOF, TIP60 is another acetyltransferase from the MYST family that can acetylate H4K16. TIP60-mediated acetylation of H4K16 seems to be crucial for the balance between NHEJ and HR pathways (Tang et al., 2013). It is worth mentioning that MOF and TIP60 can acetylate both histone and nonhistone proteins. In this regard, different studies describe that following DNA damage, MOF and TIP60 participate in the acetylation of ATM which seems required for its full activation. (Gupta et al., 2005; Sun et al., 2005).

On the other hand, removal of H4K16Ac depends on different HDACs. SIRT1, SIRT2 and SIRT3, from the sirtuin family, are the main HDACs responsible for H4K16Ac deacetylation. SIRT1 is a nuclear sirtuin that deacetylates H4K16Ac in a cell cycle-independent manner, while SIRT2 is cytoplasmatic and is transported to the nucleus during G2/M when it can only deacetylate H4K16Ac (Vaquero et al., 2006). SIRT3 is mainly located in the mitochondria, although a small subpopulation localizes in the nucleus, where it deacetylates H4K16Ac upon cellular stress (Scher et al., 2007). Moreover, HDAC1 and HDAC2 (class I HDACs) deacetylate H4K16Ac during S phase and in response to DNA damage (Miller et al., 2010; Tang et al., 2013).

Of particular relevance is the role of H4K16Ac in DNA damage repair; specifically, its involvement in the regulation of 53BP1 recruitment. H4K16 acetylation state directly affects the binding affinity of the 53BP1 Tudor domain for the neighboring H4K20me2 (Hsiao and Mizzen, 2013; Tang et al., 2013). H4K16 acetylation by the acetyltransferase TIP60 disrupts a salt bridge between the negatively charged Glu1551 of the 53BP1 Tudor domain and the positively charged non-acetylated H4K16, resulting in a reduced affinity of 53BP1 to H4K20me2 (Tang et al., 2013). Moreover, 53BP1 association with H4K20me2 seems to be facilitated by histone deacetylases HDAC1 and

HDAC2, which deacetylase H4K16Ac shortly after DSB induction (Miller et al., 2010; Hsiao and Mizzen, 2013; Tang et al., 2013). This dynamic pattern of H4K16Ac at DSBs has been proposed to contribute to DSB repair pathway choice by regulating the balance between 53BP1 and BRCA1 (Tang et al., 2013). Supporting the involvement of H4K16Ac in DNA damage repair, it has been shown that the absence of this mark in *Zmpste24^{-/-}* mice, a model of premature aging, correlates with a delayed recruitment of 53BP1 (Krishnan et al., 2011a).

2.2.2. Histone lysine deamination: oxidation of H3 at lysine 4 (H3K4ox)

Apart from the classical PTMs, other PTMs have been recently described. Among them, deamination of lysine 4 trimethylated in H3 (H3K4me3) by the catalytic activity of the lysyl oxidase like protein 2 (LOXL2) is a novel epigenetic mark with promising roles in the DDR (Herranz et al., 2016; Cebrià-Costa et al., 2019). LOXL2 deaminates H3K4me3 through an amino-oxidase reaction that requires the internal co-factor lysine-tyrosylquinone (LTQ), releasing the amino group and converting K4 into an allysine (H3K4ox) (Figure 11). Recently, it has been shown that another protein of the LOX family, LOXL1, is also capable of oxidizing H3K4me3 *in vitro* (Iturbide et al., 2015).

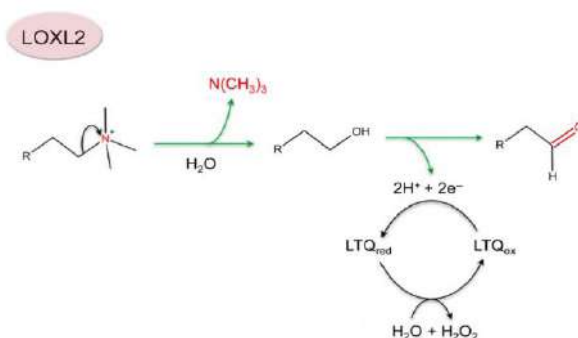


Figure 11. Reaction model for H3K4me3 oxidation. LOXL2 removes the amino group of the lysine, the resulting alcoholic form is rapidly oxidized by the LTQ cofactor of LOXL2 generating the aldehyde group. Modified picture from Herranz et al., 2016 with permission from the copyright owner.

Studies performed so far on the H3K4ox physiological functions relate this mark with breast cancer. Specifically, mesenchymal triple-negative breast cancer (TNBC) cell lines and breast cancer patient-derived xenographs (PDXs) show high H3K4ox levels that correlate with high LOXL2 expression (Cebrià-Costa et al., 2019). Regarding the impact of this mark on the chromatin structure, H3K4ox is enriched in heterochromatin regions in TNBC cells. Particularly, H3K4ox peaks are found within certain specific heterochromatin regions and lamina-associated domains (LADs). Supporting these findings, reduction of LOXL2 and the subsequent decrease of H3K4ox have been associated with chromatin decondensation (Cebrià-Costa et al., 2019). Since chromatin accessibility is related to DDR, it has been proposed that LOXL2, through the oxidation of H3K4me3, might lead to a more compacted chromatin and to a less efficient DDR. This hypothesis is in accordance with the fact that the absence of LOXL2 and the subsequent reduction of H3K4ox results in higher detection of γ H2AX and 53BP1 foci (Cebrià-Costa et al., 2019).

3. Aging

Aging is a physiological process characterized by a time-dependent loss of cellular and tissue integrity, leading to impaired biological function and increased risk of pathologies (Campisi, 2013). Aging is accompanied by molecular and cellular changes that can be considered as hallmarks of this process. These aging-related hallmarks are classified into three categories: primary, antagonistic and integrative hallmarks (**Figure 12**) (López-Otín et al., 2013).

The primary hallmarks are considered to be the major causes of age-related cellular damage. Indeed, the common characteristic of this type of hallmarks are their clearly negative effects on the organismal fitness. This is the case of genomic instability, telomere loss, epigenetic alterations and defective proteostasis. On the contrary, antagonistic hallmarks have opposite effects depending on their intensity: at low levels, they have beneficial effects but at

high levels, they are deleterious. This group comprises deregulation of nutrient sensing, mitochondrial dysfunction and senescence. Lastly, the integrative hallmarks result as direct consequences of the previous two groups of hallmarks. They are responsible for the age-related functional decline and loss of tissue homeostasis. This is the case of stem cell exhaustion and altered intercellular communication (López-Otín et al., 2013).

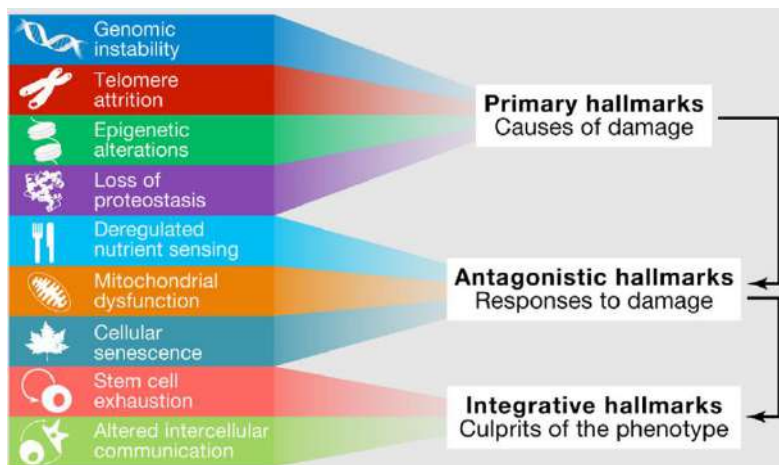


Figure 12. Classification of the hallmarks of aging. Picture reproduced from López-Otín et al., 2013 with permission from the copyright owner.

The following sections focus on the contribution of age-associated unrepaired DNA damage to genomic instability and on the major epigenetic changes related to the aging process.

3.1. DNA damage response in aging

The accumulation of genetic damage throughout life is one of the major causal factors of aging (Moskalev et al., 2013). If the DNA damage is unrepaired or incorrectly repaired, these lesions can result in severe mutations (Vijg and Suh, 2013). For this reason, a great number of studies have proposed that aging is accompanied by accumulation of somatic mutations that ultimately lead to genome instability (Best, 2009; Hoeijmakers, 2009; Freitas and de Magalhães, 2011). Indeed, the link between accumulation of DNA damage and aging has been reinforced by the studies of premature aging syndromes, showing

defective DNA repair as a common feature of these pathologies (Hoeijmakers, 2009; Gregg et al., 2012). Additionally, treatments that result in DSB induction, such as γ -irradiation, accelerate aging in animal models and human cancer survivors (Gorbunova and Seluanov, 2016).

From the several DNA lesions that accumulate with age, defects on DSB repair result in chromosomal rearrangements and loss of genome integrity (Gorbunova and Seluanov, 2016). Increased frequency of basal DSBs have been observed in neurons from aged rats (Mandavilli and Rao, 1996) and in liver, lung, testes, kidney and brain from aged mice (Sedelnikova et al., 2004). Regarding human aging, the incidence of DSBs increases in fibroblasts and in human mammary epithelial cells (HMECs) during *in vitro* aging (Sedelnikova et al., 2008; Hernández et al., 2013). Similarly, persistent DSBs have been found in different cell types from human aged donors such as hematopoietic stem cells (Rübe et al., 2011), lymphocytes (Sedelnikova et al., 2008), fibroblasts (Kalfalah et al., 2015), oocytes (Titus et al., 2013) or HMECs (Anglada et al., 2019).

The accumulation of DNA damage with age suggests age-associated impairments in the DSB repair processes. To this extent, it has been shown that NHEJ becomes more error-prone in senescent human fibroblasts (Seluanov et al., 2004) and, in support of this observation, a reduction of the levels of Ku70/80 has been described in replicative senescent cells (Seluanov et al., 2007). Furthermore, NHEJ efficiency declines in peripheral lymphocytes, fibroblasts and HMECs from aged human donors (Garm et al., 2013; Li et al., 2016; Anglada, 2018) which, in some cases, has been also related to a lower expression of Ku70 and MRE11 with increased donor's age (Ju et al., 2006). Additionally, DSB repair by NHEJ is also reduced in multiple tissues of aged mice and rats (Vyjayanti and Rao, 2006; Vaidya et al., 2014). Regarding HR-mediated repair, decrease of its efficiency has been observed in diverse somatic cell types from aged mice (White et al., 2013; Sukup-Jackson et al.,

2014). Moreover, central proteins of the HR pathway, such as RAD51 or CtIP, are reduced in replicative senescent human fibroblasts (Mao et al., 2012).

These alterations in the repair of DSBs may contribute to age-associated genomic instability and to a higher incidence of tumorigenesis with age. Therefore, a deeper understanding of the repair pathways affected during aging would provide a potential therapeutic strategy to prevent the decline in genome integrity.

3.2. Epigenetic alterations

Normal ageing processes as well as pathogenic age-related disorders are associated with profound epigenetic changes, resulting in changes of gene expression and disturbances in the epigenomic landscape (Brunet and Berger, 2014). These age-associated epigenetic changes involve alterations in DNA methylation patterns, chromatin remodeling and PTMs (López-Otín et al., 2013).

Among the distinct epigenetic mechanisms, aging is strongly associated with global and local changes in the DNA methylation profile (Ben-Avraham et al., 2012). In particular, aging is related to a global hypomethylation although several loci, including some containing tumor suppressor genes or differentiation genes, become aberrantly hypermethylated with age (Christensen et al., 2009; Maegawa et al., 2010). Similarly, at the chromatin level, aging is associated with a loss of constitutive heterochromatin together with an increase in facultative heterochromatin at specific loci. This process has been referred as the “heterochromatin redistribution” model for aging (Tsurumi and Li, 2012). Consequently, age-related deregulation of silenced genes and global heterochromatin loss result in altered gene expression patterns and cellular dysfunction (Gorbunova and Seluanov, 2016).

Changes in the abundance of histone PTMs during aging has been extensively investigated. In particular, the age-related changes in H4K16Ac are especially

interesting for the present study. Alterations in the pattern of H4K16Ac during aging have been studied in a wide range of organisms and cell types. However, given the diversity of organs studied and variations between species, these findings can be sometimes contradictory. For instance, in yeast, replicative aging is associated with an increase of H4K16Ac. Indeed, a reduction of H4K16Ac levels by depletion of its acetyltransferase Sas2 extends the replicative lifespan of normal and senescent yeast strains (Dang et al., 2009; Kozak et al., 2010). Conversely, global decrease of H4K16Ac has been observed in both replicative and oncogene-induced senescence in human fibroblasts (Contrepois et al., 2012). Similarly, global H4K16 hypoacetylation has been associated with an early cellular senescence phenotype in a mouse model of Hutchinson-Gilford progeria syndrome (Krishnan et al., 2011a). A global deacetylation of H4K16 occurs in the liver, heart and bone marrow of normal old mice (Krishnan et al., 2011a). Additionally, an age-dependent decrease of H4K16 acetylation has been also observed in oocytes from aged mice (Manosalva and González, 2009). Hence, H4K16 acetylation stands as an interesting epigenetic mark involved in both aging and DNA repair regulation.

3.3. Cellular aging models

The molecular mechanisms of aging-related processes are challenging fields of study, particularly in humans. The environmental influences, genetic heterogeneity and most importantly, their long natural lifespan, make aging research in humans very complicated. To overcome these difficulties, the isolation and comparison of cells from young and old donors represent a widely-extended approach to study *in vivo* human aging (Boraldi et al., 2010). Nevertheless, depending on the cell type, they might require a short time in culture, exposing them to cell culture conditions and selection (Arantes-Rodrigues et al., 2013). Due to the heterogeneity and complexity of the aging phenotype in humans, *in vitro* studies using serially cultured cells have been also extensively used as a reliable approach to investigate the mechanisms of

aging. The biggest limitation of *in vitro* studies is whether cell culture adequately reflects *in vivo* conditions (Lidzbarsky et al., 2018). Other alternative approaches are the use of model organisms and the study of cells isolated from patients with progeroid syndromes, especially Hutchinson–Gilford progeria syndrome and Werner syndrome (Mitchell et al., 2015; Lidzbarsky et al., 2018). In summary, each aging model has its drawbacks and its advantages, thus researchers should carefully select the most convenient one for their work.

In the present study *in vitro* aging and senescent models have been used to study human aging and thus they are further described in the following subsections. Since Hayflick and Moorehead (1961) demonstrated that fibroblasts have limited proliferation capability in culture before undergoing replicative senescence, extensive passaging of fibroblasts have become a widespread *in vitro* model for the study of genetics and biology of aging (Lidzbarsky et al., 2018). Additionally, fibroblast strains, such as BJ or IMR90, have been used to generate stable models of inducible senescence in response to aberrant activation of oncogenic signalling, resulting in oncogene-induced senescence (OIS) (Innes and Gil, 2019).

3.3.1. Oncogene-induced senescence (OIS)

Cellular senescence, a process that imposes permanent cell-cycle arrest in response to various stressors, has emerged as an important contributor to organismal aging. This process is triggered by several factors such as accumulation of DNA damage, telomere erosion and various epigenetic alterations (López-Otín et al., 2013; Lidzbarsky et al., 2018).

The primary purpose of the age-related increase of senescent cells is to prevent the propagation of damaged and potentially oncogenic cells (Campisi and d’Adda di Fagagna, 2007; Campisi, 2013). However, in aged organisms the capacity to clear senescent cells is inefficient and eventually their accumulation leads to tissue inflammation and to the development of age-related diseases (Childs et al., 2015).

Senescence can occur both during *in vitro* and *in vivo* aging (Pedro de Magalhães, 2004). There are different types of senescence, depending on the senescence-inducing stimuli (Kuilman et al., 2010). Telomere attrition and DNA damage accumulation due to cellular replication, lead to replicative senescence (Campisi and d'Adda di Fagagna, 2007). Senescence can be also induced in the absence of any detectable telomere loss as a consequence of inadequate culturing conditions or oxidative damage that may promote stress-induced senescence (Kuilman et al., 2010). Furthermore, senescence can be triggered by the expression of oncogenes such as RAS, which results in oncogene-induced senescence (Kuilman et al., 2010).

The development of inducible models of OIS allows for a better understanding of the senescent phenotypes. Their relative ease of use and reliability make OIS models optimal tools for studying senescence (Innes and Gil, 2019). To establish these models, a mutant oncogene is introduced into the cells, generating an excessive mitogenic signaling that activates suppressor proteins such as p53 which leads to the upregulation of its target gene, p21.

Then, p21 activates retinoblastoma protein (Rb) through inhibition of a cyclin-dependent kinase (Cdk) complex, cyclin E/Cdk2. Finally, the activated (hypophosphorylated) Rb inhibits cell cycle progression. Another Cdk inhibitor, p16^{INK4a}, which also activates Rb through inhibition of cyclin D/Cdk4,6 complexes, is also overexpressed in cells undergoing OIS (Figure 13) (Serrano et al., 1997; Ben-Porath and Weinberg, 2005; Funayama and Ishikawa, 2007).

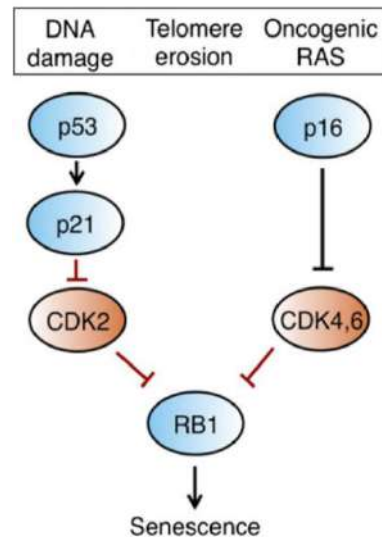


Figure 13. Senescence is controlled by p53 and p16–Rb pathways. Scheme of the molecular pathways involved in senescence. Modified picture from Lujambio, 2016 with permission from the copyright owner.

3.3.2. *In vitro* aging

The complexity and duration of human aging makes it highly difficult to perform *in vivo* studies. Considering that age-associated changes also occur at cellular levels, it is reasonable to assume cellular culture as a simpler alternative to study human aging (Pedro de Magalhães, 2004). To this extend, normal human cells show a limited number of divisions *in vitro* before they undergo replicative senescence (Hayflick and Moorhead, 1961). This proliferation limit can be associated with the *in vivo* lifespan of the organism (Rubin, 1997). Hence, *in vitro* aging of normal human cells by serial culture constitutes a model that mimics the cellular and molecular changes associated with development and aging. Furthermore, *in vitro* studies enable comparisons between many cell types, easy manipulation, direct treatments and the study of cell's responses isolated from their original environment (Lidzbarsky et al., 2018).

Normal human dermal fibroblasts are widely used in cell culture, since they are resistant to culture stress, easily cultured and maintained *in vitro*. Furthermore, cultured primary fibroblasts exhibit most of the established and ubiquitous hallmarks of aging such as genome instability, telomere attrition or epigenetic alterations. Consequently, it is not surprising that fibroblasts aged in culture represent an extensively used *in vitro* model for exploring the molecular pathways underlying human aging (Phipps et al., 2007; Dekker et al., 2009; Boraldi et al., 2010; Tigges et al., 2014).



Hypothesis & Objectives

Hypothesis

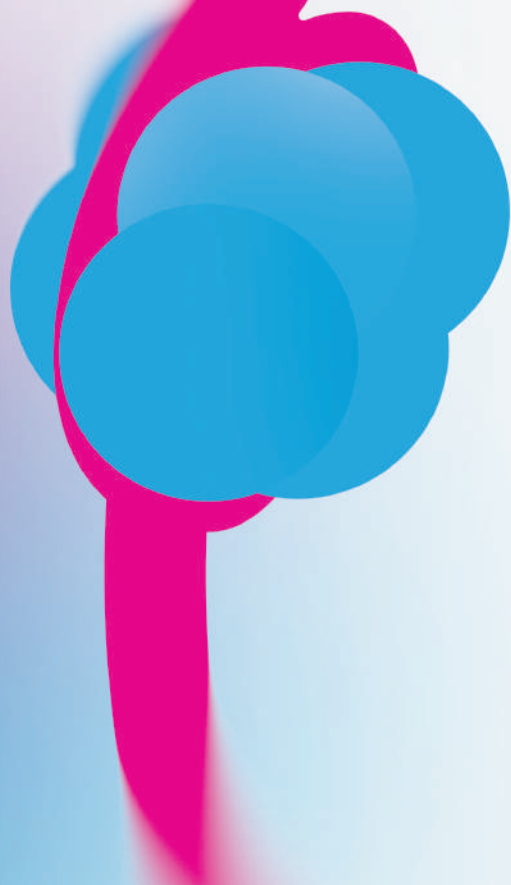
Age-associated epigenetic alterations might contribute to DNA repair defects that favor the accumulation of DSBs and increase genomic instability with age.

Objectives

The main objective of this thesis is to evaluate the contribution of histone modifications to age-associated DSB accumulation.

In order to address this general objective, we aimed to fulfil the following specific objectives:

1. To analyze the distribution pattern of the novel epigenetic mark H3K4ox in OIS and in *in vitro* aging.
2. To evaluate the levels of H4K16 acetylation in OIS and in *in vitro* aging.
3. To study H4K16Ac before and after DSB induction in young and in *in vitro* aged fibroblasts.
4. To determine the relationship between the acetylation levels of H4K16 and the recruitment of 53BP1 to DSBs during *in vitro* aging.



Materials & Methods

1. Cell culture

1.1. Culture of Human Dermal Fibroblasts

Human dermal fibroblasts (HDFs) from healthy human foreskin were commercially obtained from Cell Applications (San Diego, CA, USA). HDFs were cultured in Dulbecco's Modified Eagle's Medium (Biowest, Riverside, MO, USA), supplemented with 10% fetal bovine serum (FBS), 1% GlutaMAX and 1% penicillin-streptomycin (Thermo Fisher Scientific Inc., Waltham, MA, USA). HDFs were incubated under conditions of 5% CO₂ atmosphere, 37°C and a relative humidity of about 95%. Medium was replaced each 48 h. Once the culture reached 80% confluence, subculture of HDFs was performed by trypsinization at a dilution rate of 1:4. Firstly, the medium was removed from the flask and cells were washed with 1XPBS Ca⁺² and Mg⁺² free. To detach cells, the culture was incubated with trypsin-EDTA (Biowest, Riverside, MO, USA) for 5 min. Subsequently, trypsin-EDTA effect was neutralized with medium and the cells were resuspended to ensure a homogeneous cell suspension.

In order to cryopreserve a culture passage of interest, a freezing medium consisting of 95% FBS and 5% dimethyl sulfoxide (DMSO) (MP Biomedical, Santa Ana, CA, USA) was prepared. Cells were collected after trypsinization and centrifuged for 5 min at 300 g. The supernatant was discarded, the cellular pellet was resuspended in the freezing medium and collected in cryotubes. These cryotubes were placed in a Mr.Frosty® freezing container which contains isopropyl alcohol and achieves a rate of cooling of -1°C/min once it is kept at -80°C. Finally, cryotubes were stored in a liquid nitrogen container. For recovery of cells after freezing, the frozen cells were thawed at 37°C for 1 min and diluted in fresh complete medium. The cells were allowed to attach for one day before the medium was replaced with fresh complete medium.

1.2. Culture of Human BJ Fibroblasts

Immortalized human diploid BJ fibroblasts expressing telomerase (hTERT) were used as a model of oncogene-induced senescence after taking advantage of the well characterized system of *ER:RAS* inducible retroviral vector (Tarutani et al., 2003; Innes and Gil, 2019). In this study, BJ^{hTERT} fibroblasts were infected with *H-RAS* oncogene fused to a 4-hydroxytamoxifen (4-OHT)-responsive Estrogen Receptor (ER) ligand binding domain. BJ^{hTERT} *ER:RAS* fibroblasts were kindly provided by Maite Huarte's laboratory at *Centro de Investigación Médica Aplicada* (Pamplona, Spain).

BJ fibroblasts were cultured in Dulbecco's Modified Eagle's Medium, supplemented with 10% FBS, 1% GlutaMAX and 1% penicillin-streptomycin. BJ fibroblasts were incubated under conditions of 5% CO₂ atmosphere, 37°C and a relative humidity of about 95%. For subculture, cells were detached from the plate surface by trypsinization. BJ fibroblasts were subcultured 3 times per week at a dilution rate of 1:5. Freezing and thawing protocols of BJs fibroblasts are the same to those explained in the section 1.1.

1.2.1. Senescence induction and detection

Exponentially growing BJ^{hTERT} *ER:RAS* fibroblasts were treated with 200 nM of 4-OHT for 8 days to induce senescence. To monitor the effects of *RAS* expression after 4-OHT treatment, detection of Senescence Associated β -galactosidase activity (SA- β -gal) was performed. SA- β -gal was assessed using a biochemical assay based on the generation of a blue precipitate that results from the cleavage of the chromogenic substrate X-Gal by the β -galactosidase enzyme (Debacq-Chainiaux et al., 2009). The protocol employed to detect SA- β -gal activity was the following:

- Fix cells with 2% formaldehyde and 0.2% glutaraldehyde in 1XPBS for 10 min at room temperature (RT).
- Aspirate the fixation solution and wash the cells twice with 1XPBS.

- Prepare SA- β -gal staining with H₂O containing 40 mM citrate-phosphate buffer (pH 6), 2 mM MgCl₂, 150 mM NaCl, 1 mg/ml X-Gal, 5 mM potassium ferricyanide and 5 mM potassium ferrocyanide. This SA- β -gal staining was added to the cells followed by a 13 h incubation in the dark at 37°C.
- Wash cells twice with 1XPBS.
- Wash cells with methanol for 30 s.
- Remove methanol and wash cells with distilled water.
- Allow the samples to dry.

To identify senescent cells, blue staining was detected under an IX71 microscope equipped with DP20 camera and cell^A software (Olympus, Hamburg, Germany). SA- β -gal positive cells were scored with the Cell Counter plug-in from the Fiji software (Schindelin et al., 2012).

2. Cell treatments

2.1. DSB induction

In addition to endogenous processes, DSBs can result from the exposure to exogenous agents such as radiation or certain radiomimetic chemicals. In this study, to generate DSBs in cultured cells, two different procedures were applied.

2.1.1. γ -irradiation

Cells were seeded and grown for at least 24 h before irradiation. In order to generate DSBs, exponentially growing HDFs were exposed to different doses of ionizing radiation (2 Gy or 5 Gy of γ -rays) using an IBL-437C irradiator equipped with two gamma sources of Cesium-137 (dose rate of 5.10 Gy/min). Cells were irradiated at the Technical Unit of Radiological Protection of *Universitat Autònoma Barcelona* (UTPR-UAB). After γ -irradiation, HDFs were incubated at 37°C for 30 min, 2 h and 24 h. In each experiment, a non-

irradiated control group of cells was also transported to the UTPR to mimic cell conditions.

2.1.2. Bleocin treatment

DSBs can also be chemically induced with radiomimetic drugs like bleocin. Cells were grown to confluence, treated with 10 µg/ml bleocin and incubated for 1 h at 37°C. Then, medium with bleocin was removed and cells were washed with 1XPBS before fixation.

2.2. Trichostatin A and Nicotinamide treatment

To study the effects of H4K16 hyperacetylation, cells were treated with functionally divergent HDACs inhibitors. Firstly, cells were treated with trichostatin A (Sigma-Aldrich, St. Louis, MO, USA) which selectively inhibits class I, II and IV mammalian HDACs (Kim and Bae, 2011). In this case, cells were treated with 1 µM TSA for 12 h at 37°C. In addition, specific inhibition of sirtuins (class III HDACs) was performed with nicotinamide (Avalos et al., 2005). Cells were treated with 5 mM nicotinamide (Sigma-Aldrich, St. Louis, MO, USA) for 24 h at 37°C. Nicotinamide was kindly provided by Vaquero's laboratory at *Institut d'Investigació Biomèdica de Bellvitge* (Hospitalet de Llobregat, Spain). When needed, treatment with both drugs was combined. After either treatment, medium with the deacetylating drug was removed, and cells were washed with 1XPBS before fixation.

3. Cell cycle analysis by flow cytometry

To analyze cell cycle distribution, the following protocol based of the measurement of cellular DNA content was carried out:

- Harvest the cells in 5 ml of 1XPBS after trypsinization and centrifuge them at 200 g for 5 min at 4°C. Then, resuspend the cells in 0.5 ml of 1XPBS.
- Fix cells by transferring the suspension into a centrifuge tube containing 4.5 ml of 70% ethanol. Store the cells at -20°C.

- Centrifuge the ethanol-suspended cells at 200 g for 5 min at 4°C.
- Wash the pellet with cold 1XPBS and centrifuge again at 200 g for 5 min at 4°C.
- Resuspend the cell pellet in 1 ml of propidium iodide staining solution (0.1% Triton-X-100 in PBS, 0.2 mg/ml DNase-free RNase A and 0.02 mg/ml of propidium iodide).
- Incubate the solution in the dark and at RT for 30 min.
- Transfer sample to the flow cytometer and measure cell fluorescence.

Fluorescence intensity was measured using FACS Calibur cytometer (Becton Dickinson, Franklin Lakes, NJ, USA) and analyzed using FlowJo software (Becton Dickinson, Franklin Lakes, NJ, USA).

4. Generation of lentiviral particles

To perform stable gene silencing, lentiviruses expressing shRNA (small hairpin RNA) against *MOF* were produced. Lentiviruses are capable of integrating shRNAs in the genome of both dividing and non-dividing cells (Manjunath et al., 2009), thus providing a high silencing efficiency. Lentiviral delivery of shRNAs was initiated with the design of the shRNA construct. Then, shRNA oligonucleotides were inserted into lentiviral vectors to produce lentiviral particles. Finally, cells were infected with the shRNA-containing lentiviruses.

Box 1. Lentiviral vector delivery of shRNAs.

Gene silencing with shRNA-containing lentiviruses is based on the use of small interfering RNAs (siRNAs) that mediate sequence-specific gene silencing. In this approach, an oligonucleotide containing the siRNA sequence followed by a ~9 nucleotide loop and a reverse complement of the siRNA sequence is cloned in viral vectors to generate the shRNA plasmid DNA. The transcription of such nucleotide sequences leads to the formation of shRNA molecules that are processed by the endoribonuclease DICER leaving a two nucleotide 3' overhang which binds to the RISC complex and leads to the activation of the enzyme Argonaute. Argonaute cleaves the sense strand which results in the formation of siRNA molecules. The siRNA, which is still contained in the activated RISC, guides the RISC complex to the corresponding mRNA due to sequence homology. Then, Argonaute cleaves the target mRNA leading to specific gene silencing (**Figure 14**) (Li and Rossi, 2008; Manjunath et al., 2009).

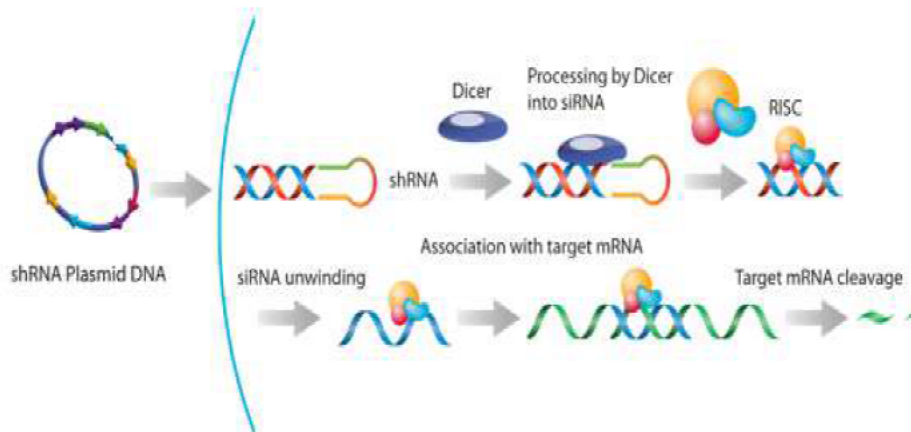


Figure 14. Outline of the shRNA plasmid-mediated gene silencing. Modified from Santa Cruz lentiviral protocols with permission from the copyright owner.

4.1. Cloning of shRNA sequences

For gene knockdown, two pLKO TRC cloning vector plasmids containing two different shRNA to silence *MOF* were used, together with a control shRNA scramble plasmid. Briefly, each *MOF* shRNA was inserted into the pLKO TRC cloning vector by restriction enzyme digestion with Age I and EcoRI and subsequent ligation was performed with T4 DNA ligase. These procedures were performed by Vaquero's laboratory at *Institut d'Investigació Biomèdica de Bellvitge* (Hospitalet de Llobregat, Spain) which kindly provided us with all the shRNA used in the present study. ShRNA sequences are detailed in the Annex II.

4.2. Plasmid amplification and isolation

In order to amplify the cloning plasmids with the inserted shRNA sequences, chemically competent *E.coli* were transformed with plasmid DNA using the heat shock method. In this procedure, bacteria were thawed on ice and gently mixed with plasmid DNA. After a 30 min incubation on ice, the mixture of bacteria and plasmid DNA was placed at 42 °C for 45 s and then placed back on ice. The bacteria transformed with the plasmid DNA, were then cultured in SOC media (Thermo Fisher Scientific Inc., Waltham, MA, USA) and incubated at 37 °C for 1 h with agitation (220-225 rpm). Finally, and in order to select those bacteria actually transformed with the plasmid DNA, they were cultured on agar plates with LB medium (Sigma-Aldrich, St. Louis, MO, USA) and ampicillin (50 µg/ml) (Thermo Fisher Scientific Inc., Waltham, MA, USA).

After an overnight incubation at 37°C, single colonies were picked and transferred to an Erlenmeyer with liquid LB medium supplemented with ampicillin to grow selected bacteria. The bacteria culture was incubated overnight at 37°C with agitation (220 rpm).

Following overnight replication, plasmid DNA was extracted and purified from bacteria according to the instructions of the NucleoBond® PC 500 kit

(MACHERY NAGEL, Düren, Germany). The maxiprep protocol was performed according to the manufacturer's instructions that establish the following major steps:

- Alkaline lysis: add the lysis buffer which is an alkaline solution containing NaOH and the detergent Sodium Dodecyl Sulfate (SDS).
- Neutralization: add the neutralization buffer which contains KAc and neutralizes the alkalinity of the resulting cell lysate.
- Purification and elution: place DNA solution into the columns and add the elution buffer containing Tris, ethanol and KCl to the column.
- Precipitate DNA with 100% isopropanol, wash it with 70% ethanol and reconstitute DNA with nuclease-free water.

To determine the effectivity of the DNA extraction, DNA concentration and purity were measured with a NanoDrop 2000 spectrometer (Thermo Fisher Scientific Inc., Waltham, MA, USA).

4.3. Diagnostic restriction enzyme digestion

To verify whether the amplification of the DNA plasmid was correct, a diagnostic digestion was performed to cut the plasmid into pieces of a specific size and the resulting fragments were examined by gel electrophoresis. For digestion of the pLKO TRC cloning vector containing the shRNA targeting *MOF* plasmid DNA, 1 µg of DNA was digested with 10 U/µl of the restriction enzyme NotI and 5X buffer for 1-2 h at 37°C. After digestion, loading buffer was added to the samples and gel electrophoresis was performed. Gel was run at 90-100 V for 1 h and the DNA fragments were visualized under a UV-light transilluminator.

4.4. Production of lentiviral particles

Second-generation lentivirus containing shRNA targeting *MOF* were produced using a transient three-plasmid expression system. This system consists of the transfection of three different plasmids into HEK-293T producing cells: a packing plasmid (psPAX2), an Env plasmid (pMD.2G) and the transfer vector

with the cloned shRNA sequences. The packing plasmid expresses Gag, Pol, Rev and Tat genes that are required for vector packing. The Env plasmid expresses VSV-G gene that encodes the viral envelop glycoprotein. The transfer vector is finally included in the viral particles created by the other two vectors (**Figure 15**).

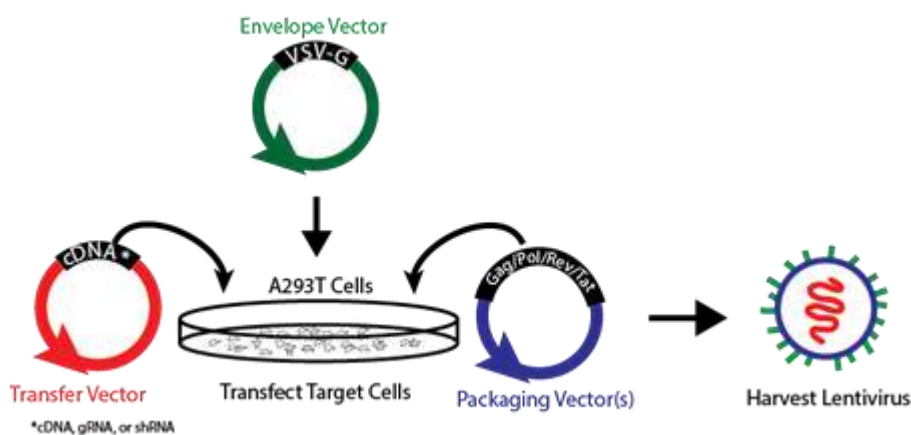


Figure 15. Schematic diagram of second-generation viral production. Picture from Addgene lentivirus protocols with permission from the copyright owner.

HEK-293T cells were plated on T75 culture flasks and cultured with Dulbecco's Modified Eagle's Medium containing 10% FBS and 1% penicillin-streptomycin. Once the cells were grown to approximately 70% confluence, transfection of HEK-293T with the three vectors was carried out using the calcium phosphate precipitation method. Briefly, 585 μl of sterile H_2O and 65 μl of 2.5 M CaCl_2 were mixed. Then, a mixture of the lentiviral transfer plasmid, together with psPAX2 packaging and pMD2.G envelope plasmid DNA was prepared at a ratio of 4:3:1, respectively. Finally, 700 μl of 2XHBS (detailed composition is included in the Annex II) were added drop wise to the DNA/ CaCl_2 mix. The final solution was incubated at RT for 15 min and subsequently added onto the cells. 24 h after transfection the medium was replaced with Dulbecco's Modified Eagle's Medium supplemented with 20% FBS and 1% penicillin-streptomycin. 48 h after transfection, the medium which contained the lentiviral particles was

harvested, cleared through a 0.2 μm filter and kept on ice until its use for infection.

4.5. Infection of HDFs with lentiviral particles

Infections were performed at the *Servei de Cultius Cel·lulars, Producció d'Anticossos i Citometria de l'Institut de Biotecnologia i Biomedicina* of the *Universitat Autònoma Barcelona*. The whole protocol was carried out into a class II biological safety cabinet placed on a special laboratory that accomplished the requirements for the safe manipulation of viral particles.

HDFs were seeded in p100 plates and grown to approximately 70% confluence. HDF medium was removed and directly replaced with the viral medium. The infected HDFs were incubated under conditions of 5% CO_2 atmosphere, 37 °C and a relative humidity of about 95%. 48 h after infection, the culture was washed twice with 1XPBS and fresh free-virus HDF medium was added. HDFs were then subcultured and plated for further experiments.

5. Analysis of gene expression

Reverse transcription quantitative-polymerase chain reaction (RT-qPCR) has emerged as one of the most powerful techniques to evaluate changes in gene expression level. Features such as great accuracy, high sensitivity, reproducibility and high-throughput make RT-qPCR the most prevalent technique to assess mRNA expression. During RT-qPCR amplification, a fluorescent dye binds to the dsDNA and fluorescence values are measured at the end of each cycle of the amplification process. Thus, the fluorescent signal is directly proportional to the DNA concentration and the correlation between amplification product and fluorescence intensity is used to calculate the amount of template DNA present at the beginning of the reaction. The point at which the fluorescence level is first detected as statistically significant above the background value is known as the threshold cycle or Ct value. The higher the

initial amount of DNA, the sooner the accumulated fluorescent product is detected and the lower the Ct value (Bustin et al., 2009).

5.1. Total RNA extraction

For isolation of total RNA, cells were seeded on p100 plates and grown to confluence. Then, cells were washed once with ice cold 1XPBS and lysed with 1 ml of TRIzol[®] (Thermo Fisher Scientific Inc., Waltham, MA, USA) by pipetting. In order to separate RNA from proteins and DNA, 100 μ l of chloroform was added for each ml of TRIzol[®] and the mixture was shaken with vortex for 10 s and incubated at RT for 3 min. After a 12000 rpm centrifugation for 15 min at 4°C, a three-phased solution was obtained: an aqueous phase containing the RNA, a DNA-enriched white intermediate phase and a protein-containing pink phase. A maximum of 200 μ l of the aqueous phase was transferred into a RNase-free eppendorf tube. From this step, Maxwell[®] RSC simplyRNA Tissue Kit (Promega, Madison, WI, USA) was used to isolate total RNA following the manufacturer's instructions:

- Add 200 μ l of the lysis buffer to 200 μ l of the collected water phase.
- Vortex vigorously for 10 s to mix.
- Transfer all 400 μ l of lysate to the first well of the Maxwell[®] RSC Cartridge.
- Add 5 μ l of DNase I solution to the fourth well.
- Place a plunger in the eighth well of each cartridge.
- Place 0.5 ml elution tubes in the front of the deck and add 40 μ l of nuclease-free water to the bottom of each elution tube.
- Run the Maxwell[®] RSC Instrument.

The RNA concentration was determined using the Nanodrop 2000 spectrophotometer. RNA was stored at -80 °C or used directly for cDNA synthesis.

5.2. cDNA synthesis from total RNA

For cDNA synthesis, 1 µg of RNA was reverse transcribed to cDNA using the iScript cDNA Synthesis (Bio-Rad, Hercules, CA, USA). For a single reaction with a total volume of 20 µl, 4 µl of 5X iScript Reaction Mix, 1 µl of iScript Reverse Transcriptase and a variable volume of nuclease-free water were mixed and incubated in a thermal cycler using the following protocol:

- Priming: 25 °C for 5 min.
- Reverse transcription: 42 °C for 30 min.
- RT inactivation: 85 °C for 5 min.
- Operational step: hold at 4 °C.

The resulting cDNA was stored at -20 °C or directly used for the RT-qPCR.

5.3. RT-qPCR

To quantify the expression level of distinct set of genes, specific oligonucleotides were designed with the Primer3 online software and were *in silico* validated with the UCSC Genome Browser (<https://genome.ucsc.edu>). Primer sequences are listed in the Annex II.

Each target gene along with a reference gene was analyzed in a 96 well plate for RT-qPCRs. For each well a 10 µl reaction mix containing 0.1 ng of cDNA, 5 µl of SYBR Green Supermix (Bio-Rad, Hercules, CA, USA), 0.2 µl of primers mix (1 µM) and 3.8 µl of H₂O was prepared. The plate was covered with a plastic film, centrifuged and placed into a CFX96 thermal cycler with Bio-Rad CFX Manager software (Bio-Rad, Hercules, CA, USA). The amplification program was as follows:

- Initial denaturation: 95 °C for 3 min.
- Denaturation: 40 cycles of 10 s at 95 °C.
- Annealing and extension: 40 cycles of 30 s at 60 °C.

After amplification, an additional thermal denaturing cycle (temperature ranged between 65 °C and 95 °C in 0.5 °C increments) was performed to obtain the melting curves of the RT-qPCR products and to verify the amplification specificity. Reactions for each sample were run in triplicates.

5.4. Data analysis

The analysis of the results was performed with Bio-Rad CFX Manager software (Bio-Rad, Hercules, CA, USA) and Microsoft Excel (Microsoft, Redmond, WA, USA). To detect changes in gene expression, RT-qPCR data were normalized against an endogenous reference gene. Normalization was performed by subtracting the Ct of the reference gene to the Ct of the gene of interest (ΔCt). Then, the relative expression of the gene of interest was calculated by the $2^{-\Delta\text{Ct}}$ method. In addition, fold change (FC) of relative mRNA expression was calculated between control and treatment conditions:

$$\Delta\Delta\text{Ct} = \Delta\text{Ct}_{(\text{control})} - \Delta\text{Ct}_{(\text{treatment})}$$

$$\text{FC} = 2^{-\Delta\Delta\text{Ct}}$$

6. Chromatin immunoprecipitation (ChIP)-qPCR

ChIP assay is an elegant and versatile technique used for probing protein-DNA interactions within the natural chromatin context of the cell (Kuo and Allis, 1999). This technique is based on the immunoprecipitation of proteins that bind chromatin. Hence, ChIP assay is employed to identify the many regions of the genome associated with a particular protein.

When performing ChIP, protein-DNA complexes are crosslinked to preserve the protein-DNA interactions occurring in the cell. Then, chromatin is digested into DNA-protein fragments. Chromatin is subjected to immunoprecipitation with antibodies against a particular protein or histone modification. Following immunoprecipitation, the protein-DNA crosslinks are reversed and the DNA is

purified. DNA sequences are analyzed using PCR (ChIP-qPCR), microarray (ChIP-chip), or sequencing (ChIP-seq) (**Figure 16**) (Kuo and Allis, 1999).

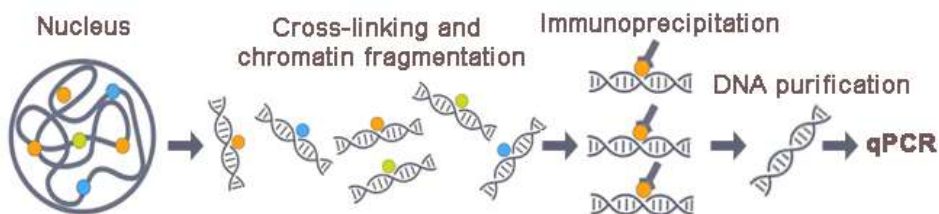


Figure 16. Scheme of the chromatin immunoprecipitation protocol. Modified from Illumina protocols with permission from the copyright owner.

In the present study, ChIP-qPCR was performed to determine the oxidation state of H3K4 in specific DNA regions during senescence using the anti-H3K4ox antibody. The protocol for ChIP-qPCR was as follows (buffer's recipes are detailed in the Annex II):

- Wash cells with 1XPBS at 37 °C.
- Crosslink protein complexes and DNA with formaldehyde 1% for 10 min at 37 °C 100 rpm.
- Stop reaction with Glycine 125 mM for 2 min at RT.
- Wash cells with 1XPBS at 4 °C.
- Lyse cells using soft lysis buffer with protease inhibitors.
- Harvest cells and centrifuge 15 min at 3000 rpm. Pellet can be stored at -80 °C.
- Resuspend pellet in SDS lysis buffer with protease inhibitors.
- Sonicate sample with pulses of 10 min at high intensity.
- Put on ice for 20 min. Centrifuge 10 min at 13000 rpm and keep the supernatant (chromatin).
 - Check the sonication protocol: take 50 ul of chromatin and dilute with 50 ul of dilution buffer. Add 1 µl RNAsa for 30 min at 37 °C. After that, add 5 µl proteinase K and leave at 65 °C shaking for at least 1 h. Then, purify DNA with a DNA isolation kit (Quiagen, Germantown, MD, USA)

and check the fragments in agarose gel (1%). The expected size of generated DNA fragments should be of around 200-300 base pairs. In case DNA is not appropriately sonicated, time of sonication should be increased.

- Quantify protein in the supernatant (chromatin) using Nanodrop spectrophotometer. To immunoprecipitate histone modifications, 200 ng of protein were used.
- Dilute sample 1/10 with dilution buffer.
- To avoid non-specific binding to agarose beads, a preclearing step was carried out: add 20 μ l of agarose beads and 1 μ g of an irrelevant antibody for each immunoprecipitation (IP). In this study, anti-IgG antibody was used. Leave 3 h rotating at 4 °C.
- Centrifuge 5 min at 2000 rpm to remove beads.
- Separate sample for immunoprecipitation:
 - 1000 μ l for the IgG control IP (it uses an antibody that will not bind to nuclear proteins to generate random immunoprecipitated DNA).
 - 1000 μ l for total H3 IP.
 - 1000 μ l for H3K4ox IP.
 - 100 μ l for the input (DNA samples that has been cross-linked, sonicated but not immunoprecipitated).
- Add corresponding antibody or IgG to each tube. Rotate at 4 °C overnight. Save input at 4 °C until next day.
- Block beads with 5% bovine serum albumin (BSA). Incubate for 15 min at 4 °C with rotation.
- Centrifuge 5 min at 2000 rpm and resuspend beads in dilution buffer. Put 500 μ l beads in each eppendorf for immunoprecipitation. Centrifuge 5 min at 2000 rpm. Discard supernatant.
- Resuspend beads with corresponding chromatin sample. Incubate for 3 h rotating at 4 °C.
- Wash beads with columns: low salt buffer, high salt buffer, LiCl buffer.

- Elute with 100 μ l elution buffer for each sample (fresh prepared: 1% SDS, 0.1M Na_2CO_3). Leave samples 1 h shaking at 37 $^\circ\text{C}$. Centrifuge 3 min at 2000 rpm, discard beads and keep the the eluted sample.
- Decrosslink samples by adding NaCl at 200 mM final concentration. Incubate at 65 $^\circ\text{C}$ overnight while shaking.
- Add Proteinase K (for each 100 μ l of sample, add 10 μ l 0.5M EDTA, 20 μ l Tris 1 M pH 6.5 and 2 μ l proteinase K) and incubate 1 h at 55 $^\circ\text{C}$.
- Purify DNA with Qiagen kit or by phenol-chloroform purification.
- Analyze ChIP results by RT-qPCR following the protocol explained in section 4.3. Primers used are detailed in Annex II.

7. Protein analysis

7.1. Western Blotting

In order to study the presence of specific proteins in samples of interest, protein immunodetection was carried out by Western Blot. This technique allows protein separation by size and their transfer to a solid support. Finally, the target protein is identified using a suitable primary and secondary antibody.

7.1.1. Protein extraction for immunoblotting analysis

To prepare cell lysates for immunoblotting analysis, cells were seeded in p100 plates. Once the culture reached a confluence of about 70%, medium was removed, and cells were washed with ice cold 1XPBS. At this point cells could be stored at -80 $^\circ\text{C}$ for several months. Then, SDS lysis buffer (detailed composition in the Annex II) was added and cells were detached and harvested by scrapping. Total cell lysis was ensured by sonication. To precipitate cell debris, samples were centrifuged at 12000 g for 2 min at 4 $^\circ\text{C}$. After centrifugation the supernatant was placed into a new eppendorf for protein quantification that was performed with the Pierce BCA Protein Assay (Thermo Fisher Scientific Inc., Waltham, MA, USA). Using this method, absorbance values of unknown samples are then interpolated onto the plot of the standard

curve to determine their concentrations. Manufacturer's instructions were used as follows:

- Pipette 25 μ l of each standard or unknown sample replicate into a microplate well.
- Add 200 μ l of the working reagent, used for the colorimetric detection of protein, to each well and mix plate thoroughly on a plate shaker for 30 s.
- Cover plate and incubate at 37 °C for 30 min.
- Measure the absorbance at 562 nm on a plate reader.

Afterwards, the samples were incubated at 70 °C for 10 min for complete protein denaturation and finally cooled on ice.

7.1.2. Immunoblotting

Proteins were separated by their mass in a SDS-polyacrylamide gel using electrophoresis under denaturing conditions. Afterwards, they were transferred to a nitrocellulose membrane for antibody detection. For this purpose, the following protocol was performed:

- Mix 25 μ g of protein with loading buffer (Thermo Fisher Scientific Inc., Waltham, MA, USA) at a 4:1 ratio and load samples into the wells of a 10% Bis-Tris gel (Thermo Fisher Scientific Inc., Waltham, MA, USA) which is used for the separation of small- to medium-sized proteins.
- Perform gel electrophoresis using 80 V for 5 min and 180 V for 40 min.
- Transfer proteins from the gel to a nitrocellulose membrane setting a program of 30 V for 90 min.
- Block membrane in 1XPBS containing 5% BSA for 1 h at RT.
- Primary antibody was diluted in 1XPBS with 3% BSA and 0.1% Tween20 (final volume of 5 ml) for 1 h at RT and used for incubation of the membrane overnight at 4 °C with agitation (**Table 1**).
- The membrane was then washed three times with TTBS (Annex II) for 5 min each wash.

- Dilute the peroxidase-conjugated secondary antibody in 1X PBS with 3% BSA and 0.1% Tween20, add it to the membrane and incubate it 1 h at RT (**Table 1**).
- Wash the membrane again three times with TTBS for 5 min each time.
- Cover the membrane with the chemiluminescence solution containing the peroxidase substrates (Millipore, Darmstadt, Germany) and incubate for 1 min.
- Measure the luminescence signal with the high-sensitivity detection system ChemiDoc XRS (Bio-Rad, Hercules, CA, USA).

Table 1. Primary and secondary antibodies used for protein analysis by Western Blot.

Antibody	Company	Reference	Host	Concentration
Anti-H4K16Ac	Active Motif	39929	Rabbit	1:1000
Anti-H3K4ox	-	-	Rabbit	1:1000
Anti-γH2AX	Millipore	05-636	Mouse	1:1000
Anti-p21	Abcam	Ab109520	Rabbit	1:1000
Anti-H3K4me3	Millipore	07-473	Rabbit	1:1000
Anti-H3K9Me3	Millipore	07-442	Rabbit	1:500
Anti-MOF	Abcam	Ab200660	Mouse	1:1000
Anti-H3	Abcam	Ab1791	Rabbit	1:15000
Anti-GAPDH	Abcam	Ab9484	Mouse	1:1000
Anti-mouse (HRP)	Millipore	12-349	Goat	1:5000
Anti-rabbit (HRP)	Millipore	12-384	Goat	1:5000

Antibody against H3K4ox was kindly provided by Sandra Peiró's laboratory at *Vall d'Hebron Institut d'Oncologia* (Barcelona, Spain) where it was generated. The specificity of the antibody was confirmed after a quality control (Cebrià-Costa et al., 2019).

7.2. Immunocytochemistry

To assess both the localization and the endogenous expression levels of the proteins of interest, the immunofluorescence technique was used. This method is based on the use of fluorophores to visualize the location of bound antibodies. To perform immunofluorescent stainings, the following procedures were applied.

7.2.1. Cell fixation

Cells were seeded on coverslip in p35 plates. Before fixation, the medium was completely removed from the plates and the cells were washed twice with 1XPBS for 5 min each wash. For fixation 1XPBS was removed and 1 ml of 4% PFA was added. After an incubation of 15 min at RT, cells were washed twice with 1XPBS for 5 min each wash. Cells were stored at 4 °C in 1XPBS with 0.2% sodium azide or directly used for immunofluorescence.

7.2.2. Double immunofluorescence for γ H2AX and 53BP1

γ H2AX and 53BP1 are detected as discrete foci in the cell nuclei. γ H2AX foci are considered to be good surrogates of DSBs, thus the combined analysis of γ H2AX and 53BP1 foci by immunofluorescence is a reliable and efficient approach for a detailed study of the formation and repair of DSBs (Rothkamm et al., 2015). Instead, the histone marks H4K16Ac and H3K4ox are detected as a pan-nuclear staining. For the immunodetection of the mentioned proteins, cells were permeabilized with 0.5% Triton X-100 in 1XPBS for 15 min at RT. The permeabilization solution was removed and the cells were washed three times with 1XPBS for 5 min each time. To detect H4K16Ac and H3K4ox, an antigen retrieval treatment was applied at this point of the protocol. The retrieval treatment allows to unmask antigenic sites by disrupting the protein cross-links, and it was carried out by incubating the cells with Target Retrieval Solution (Agilent, Santa Clara, CA, USA) for 1 h at 65 °C. Then, cells were blocked for 1 h with 0.5% BSA-0.15% glycine in 1XPBS. The primary antibodies anti-

γ H2AX, anti-53BP, anti-H4K16Ac and anti-H3K4ox, alone or combined, were also diluted in the blocking solution and were then added to the cells (for antibody specifications see **Table 2**). Cells were incubated overnight at 4 °C with the primary antibodies and then washed three times with 0.1% Tween-20 in 1XPBS. The secondary antibody solution containing the Cy3-conjugated anti-mouse or the Alexa 488-conjugated anti-rabbit diluted in the blocking solution was then added to the cells (for antibody specifications see **Table 2**). After 1 h incubation at RT in the dark, the cells were washed three times with 0.1% Tween-20 in 1XPBS for 5 min each wash. Then, coverslips were rinsed in distilled water, alcoholically dehydrated (75%, 80% and 100% EtOH) and mounted on microscope slides using the Vectashield Mounting Medium for fluorescence (Vector Laboratories, Burlingame, CA, USA) supplemented with 0.25 μ g/ml of DAPI.

7.2.3. Triple immunofluorescence for γ H2AX, 53BP1 and H4K16Ac

A triple staining for the combined detection of γ H2AX, 53BP1 and H4K16Ac was performed. For this type of immunofluorescence, cells were fixed applying the same protocol described above (for antibodies specifications see **Table 2**). The rest of the steps for the triple immunostaining were as follows:

- Permeabilize cells with 0.5% Triton X-100 in 1XPBS for 15 min at RT.
- Wash the cells twice with 1XPBS for 5 min each time.
- Block the cells for 1 h with 0.5% BSA-0.15% glycine in 1XPBS.
- Incubate cells overnight at 4 °C with primary antibody solution containing anti- γ H2AX (mouse) and anti-53BP1 (rabbit).
- Cells were washed three times with 0.1% Tween-20 in 1XPBS for 5 min each time.
- Incubate cells for 1 h at RT with secondary antibody solution containing the Alexa488-conjugated anti-mouse (dilution: 1:500) and the Alexa 594-conjugated anti-rabbit (dilution: 1:500).

- Wash cells three times with 0.1% Tween-20 in 1XPBS for 5 min each time.
- Re-incubate cells for 1 h at RT with the secondary antibody solution containing Alexa488-conjugated anti-mouse and the Alexa 594-conjugated anti-rabbit to occupy the maximum number of epitopes.
- Incubate cells overnight at 4 °C with primary antibody solution containing the anti-H4K16Ac diluted in blocking solution.
- Wash cells three times with 0.1% Tween-20 in 1XPBS for 5 min each time.
- Incubate cells for only 30 min at RT with secondary antibody solution containing Alexa 532-conjugated anti-rabbit.
- Wash cells three times with 0.1% Tween-20 in 1XPBS for 5 min each time.
- Rinse cells briefly with distilled water, alcoholically dehydrate them and apply the counterstain with DAPI at a final concentration of 0.25 µg/ml in Vectashield Mounting Medium.

Table 2. Primary and secondary antibodies used for protein detection by immunofluorescence staining.

Antibody	Company	Reference	Host	Concentration
Anti-γH2AX	Millipore	05-636	Mouse	1:1000
Anti-53BP1	Abcam	Ab21083	Rabbit	1:2000
Anti-H4K16Ac	Active Motif	39929	Rabbit	1:200
Anti-H3K4ox	-	-	Rabbit	1:50
Anti-mouse (Cy3)	Jackson	115-165-146	Goat	1:1000
Anti-rabbit (488)	Thermo Fisher	A-11034	Goat	1:500
Anti-mouse (A488)	Jackson	115-545-205	Goat	1:1000
Anti-rabbit (A594)	Thermo Fisher	A-11037	Goat	1:500
Anti-rabbit (A532)	Thermo Fisher	A-11009	Goat	1:1000

7.2.4. Immunofluorescence analysis

In order to analyze the immunofluorescence preparations, images were acquired using an Olympus BX61 epifluorescent microscope (Olympus, Hamburg, Germany). This microscope was equipped with a CV-M4+CL camera (JAI, Grosswallstadt, Germany) and with Cytovision software (Applied Imaging, Newcastle, UK). All the measurements from the acquired images were obtained after blind analysis.

To quantify γ H2AX and 53BP1 foci, images from slides with γ H2AX and 53BP1 immunofluorescence were captured with a 100x objective using predefined settings. First, each cell nucleus was identified, and the image was captured using the DAPI channel. Afterwards, images from γ H2AX and 53BP1 foci in each nucleus were sequentially acquired using the red and green channels. At least 100 cells were analyzed for each condition or treatment.

For 53BP1/ γ H2AX colocalization analysis, the number of γ H2AX foci within each nucleus was counted. Then, the presence or absence of 53BP1 foci at these γ H2AX foci was examined. To individually count foci, the Cell Counter plug-in from the Fiji software was used (Schindelin et al., 2012).

In the present study, fluorescence intensity quantification was also performed. To compare fluorescence intensity levels from different immunostainings, identical image acquisition settings and exposure times were applied. For H4K16Ac and H3K4ox immunostaining, channels were sequentially collected, being the DAPI channel the first one to be acquired followed by the green channel that marked H4K16Ac or H3K4ox.

To analyze the fluorescence intensity levels of H4K16Ac and H3K4ox in cell nuclei, the analysis of the acquired images was performed using a self-designed macro program based on previous Image J plugins that automates a series of Image J commands (Gavet and Pines, 2010). The macro code is detailed in the Annex II. By creating this macro, we could analyze the

fluorescence levels of H4K16Ac or H3K4ox in each analyzed nucleus. Before applying the macro, colocalization between DAPI signal and H4K16Ac or H3K4ox was checked. Then, the nucleus shape was selected in the image from the green channel corresponding to H4K16Ac or H3K4ox signaling. Subsequently, the integrated density (the product of the area and the mean gray value) was measured in the selected area. In addition, a random region from outside of the nucleus was automatically selected and its fluorescence intensity was measured. This background measurement was subtracted to the fluorescence intensity of the nucleus of interest.

To graphically plot the fluorescence intensity measurements, the corrected total cell fluorescence (CTCF) was calculated with the following formula (Gavet and Pines, 2010):

$$\text{CTCF} = \text{Integrated Density} - [\text{Area of selected cell} \times \text{Fluorescence mean of background measurements}]$$

8. Statistics

For the statistical analysis of the data, different tests were applied using the GraphPad Prism 6 software (GraphPad Software, La Jolla California, USA).

Mann-Whitney test was conducted to compare differences between two independent groups when the dependent variable was continuous, but not normally distributed. To establish the differences among three or more independent groups on a continuous dependent variable with non-normal distribution, the Kruskal-Wallis test was selected. If the Kruskal-Wallis test produced a significant p-value, Dunn's post-hoc test was conducted for pairwise multiple comparison, in order to discern which pair combinations were significantly different.

Welch's t-test was applied when comparing gene expression levels between two independent groups with small to moderate sample size. To compare gene expression levels among three or more independent groups with small to

moderate sample size ,one-way ANOVA was used. If the one-way ANOVA test resulted in a significant p-value, Tukey's post-hoc test was applied for pairwise multiple comparison.

The statistically significant level was defined as significant (*) for a $p < 0.05$, very significant (**) for $p < 0.01$ and highly significant (***) for $p < 0.001$.





Results

1. Establishment of aging models

Physiological aging is a multifactorial process which results from the complex interactions among different molecular mechanisms (López-Otín et al., 2013). To uncover the basic causes of aging, age-associated mechanisms have been investigated in various model organisms and systems. In fact, *in vitro* studies have become the basis for most of the current knowledge about the molecular mechanisms of human aging (Lidzbarsky et al., 2018). For this reason, two of these cellular models of aging were established to study the contribution of age-associated epigenetic alterations to the DNA damage repair response. Once established, the characterization of these two cellular models was performed to ensure its suitability to develop the aims of the present research.

1.1. Establishment of an oncogene-induced senescence model

Senescence is a stable cell cycle arrest induced in response to telomere attrition after serial cultivation, or to different stressors like aberrant oncogenic signalling (Campisi, 2013). The irreversible cell cycle arrest of senescent cells is considered a cellular manifestation of organismal aging, suggesting that senescent cells deplete tissues of replication-competent cells needed for homeostasis, repair and regeneration (López-Otín et al., 2013). Given that with advanced age, senescent cells accumulate in tissues, the study of senescence could lead to a deeper understanding of aging phenotype. Hence, inducible models of OIS allow to evaluate the molecular causes and effectors of senescent state.

OIS was firstly observed in normal human fibroblasts which expressed activated *RAS* (Serrano et al., 1997) and, in fact, the OIS model used in this study is based on the well-characterized *Estrogen Receptor:RAS* (ER:RAS) inducible retroviral vector carrying *H-RAS*^{G12V} (Tarutani et al., 2003; Innes and Gil, 2019). In this system, immortalized human diploid BJ fibroblasts expressing

human telomerase reverse transcriptase (hTERT) were infected with a vector expressing a *ER:RAS* fusion. In this construct, *H-RAS*^{G12V} is fused to a mutant form of the estrogen receptor ligand binding domain. Treatment with 4-OHT, the active metabolite of tamoxifen that binds to ER, induces the activation of the *ER:RAS* fusion. Thus, the expression of *RAS* upon 4-OHT treatment causes *ER:RAS* BJ^{hTERT} fibroblasts to undergo senescence. *ER:RAS* BJ^{hTERT} fibroblasts were kindly provided by Maite Huarte's laboratory at *Centro de Investigación Médica Aplicada* (Pamplona, Spain).

Upon 8 days of 4-OHT treatment, the effects of *RAS* expression on BJ fibroblasts were monitored by analysing different senescence markers. BJ fibroblasts treated with 4-OHT displayed changes in morphology, becoming flat and enlarged (**Figure 17**). A flattened appearance and often irregular-shape nuclei are typical features of senescent cells (Wang and Dreesen, 2018). On the contrary, no morphology changes were detected in the untreated BJ fibroblasts (**Figure 17**). Furthermore, a decrease in cellular density was observed in BJ fibroblasts treated with 4-OHT compared with untreated BJ fibroblasts, pointing out that BJ cells treated with 4-OHT become growth-arrested, whereas control cells continued proliferating (**Figure 17**).

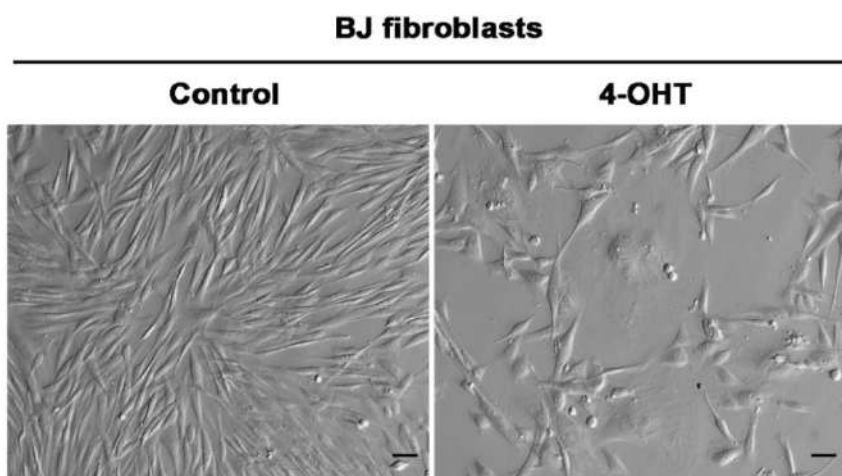


Figure 17. *ER:RAS* BJ fibroblasts culture characterization. Representative pictures showing the morphology of BJ fibroblasts in control conditions and after 4-OHT treatment. Scale bar: 10 μ m.

Cells were also stained to identify SA- β -Gal activity which is the most widely used biomarker for senescent cells. β -galactosidase is overexpressed in senescent cells resulting in the accumulation of the endogenous lysosomal β -galactosidase (Itahana et al., 2013). Following *RAS* activation, a significant higher percentage (60.25%) of BJ fibroblasts displayed SA- β -Gal activity compared to untreated fibroblasts (2.85%) (Figure 18).

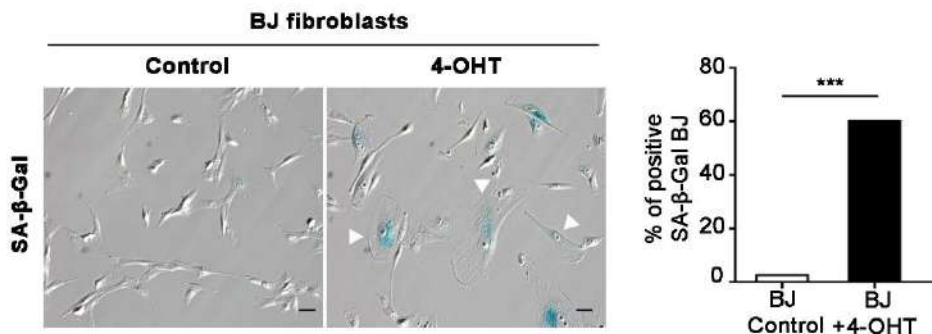


Figure 18. SA- β -Gal staining. Images showing SA- β -Gal activity and percentage of positive SA- β -Gal BJ fibroblasts in control conditions and after 4-OHT treatment. Arrowheads indicate the typical flattened shape of senescent cells. Scale bar: 10 μ m. P-value indicates the Chi-square test significant level: *** p <0.001.

We also analyzed the expression of some senescence effectors by western blot. Senescence is associated with the increased expression of the cyclin-dependent kinase inhibitor p21 which promotes cell cycle arrest (Muller, 2009). After 4-OHT treatment, *RAS* activation caused a marked increase in the expression of p21. Transcriptional changes are known to occur during senescence (Hernandez-Segura et al., 2017) thus we examined the effects of 4-OHT treatment on H3K4me3 (an active transcription mark) and H3K4me3(repressive transcription mark) (Li et al., 2007). The results showed that treatment of BJ fibroblasts with 4-OHT led to a global decrease of H3K4me3 levels which was accompanied by a slight increase of H3K4me3levels, suggesting that OIS does reduce transcriptional activity of the cells (Figure 19A).

In this line, senescence-associated heterochromatic foci (SAHF), which are transcriptionally silenced DNA regions that are enriched in senescent cells (Parry and Narita, 2016), were also detected by nuclear staining with DAPI. (Figure 19B).

Another characteristic of senescent cells is the accumulation of DNA damage, as the number of γ H2AX foci increases in senescent cells in most tissues and species (Campisi and d'Adda di Fagagna, 2007; d'Adda di Fagagna, 2008). In agreement with this fact, immunostaining against γ H2AX showed a higher number of γ H2AX foci in 4-OHT-treated BJ fibroblasts than in untreated cells (Figure 19B, 19C). Taking these results together, the senescence state mediated by *RAS* activation was confirmed in *ER:RAS* BJ fibroblasts, reinforcing these cells as an appropriate model to study cellular senescence.

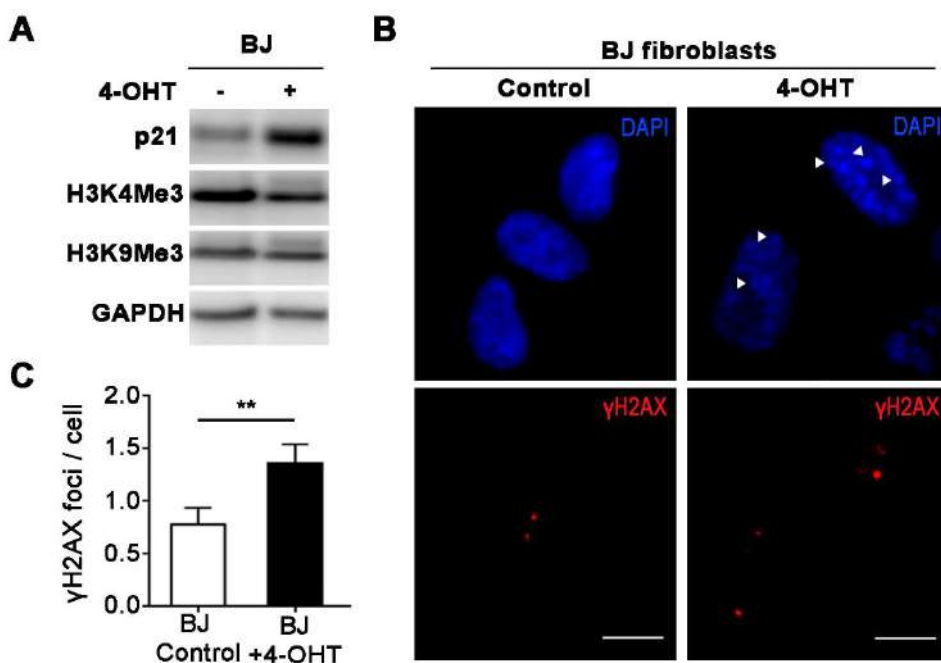


Figure 19. Senescence markers in *ER:RAS* BJ fibroblasts. (A) Western blot analysis of total protein levels of p21, H3K4me3 and H3K9me3 in control and 4-OHT-treated BJ fibroblasts. GAPDH was used as loading control. (B) Staining of cell nuclei with DAPI (blue) and immunofluorescence of γ H2AX (Cy3, red) in control and 4-OHT-treated BJ fibroblasts. Scale bar: 10 μ m. (C) Mean number of γ H2AX foci per cell in control and 4-OHT-treated BJ fibroblasts. SAHF are indicated by arrowheads. Error bars indicate SEM. P-value indicates the Mann Whitney test significant level: ** $p < 0.01$.

1.2. Establishment of an *in vitro* aging model

Normal somatic cells that are serially cultured are a well-studied model that mimics the cellular and molecular changes occurred during aging (Mainzer et al., 2018). The limited lifespan of cultured normal human fibroblasts *in vitro*, which depends on the age of the donor, has led to their extensive use as a model system to study human cellular aging (Phipps et al., 2007; Dekker et al., 2009; Boraldi et al., 2010; Tigges et al., 2014).

In this study, an *in vitro* cellular aging model based on the growing of primary human dermal fibroblasts (HDFs) in culture for some weeks was established. HDFs have a limited growth potential and reach their replicative limit after 30 passages in culture (Sedelnikova et al., 2004). HDFs with less than 10 passages in culture were considered young or early passage (EP) cells. Instead, old or late passage (LP) HDFs refer to those fibroblasts with more than 20 passages in culture. Serial culture of HDFs was accompanied by characteristic morphology changes as culture passages increased. EP HDFs displayed the typical spindle shape of adherent fibroblasts while LP HDFs lost its original morphology showing enlarged cell size and increased number of vacuoles (**Figure 20A**). To confirm the gradual loss of replicative potential with culture time, we established the growth curve of HDFs (**Figure 20B**). The results showed that the number of HDFs suffered from a reduction in the first 24 h after passage which was more evident in LP HDFs. From 24 to 96 h, EP HDFs displayed normal exponential growth while LP HDFs showed lower proliferation. Therefore, at 96 h of culture, accumulated LP HDFs were approximately half the number of EP HDFs (**Figure 20B**). Morphological changes and diminution of replicative capability of HDFs in culture coincide with the extensively described features of cellular aging (DiLoreto and Murphy, 2015).

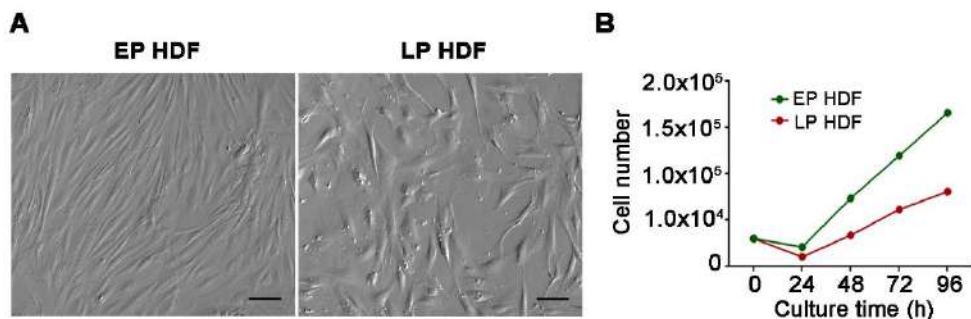


Figure 20. Characterization of HDFs culture. (A) Morphology of HDFs at EP and LP in culture. Scale bar: 10 μ m (B) Growth curves of EP HDFs (green) and LP HDFs (red).

To analyze whether there were differences in cell cycling between EP and LP HDFs, a cell cycle analysis was performed using flow cytometry. Analysis on cell cycle profile did not show significant differences in the distribution of cells throughout the different cell cycle phases between EP and LP HDFs (**Figure 21**). In both EP and LP HDFs, most of the cells were in G1 phase, and the proportion of cells in S phase was very similar between EP and LP HDFs. The number of cells in G2 was slightly higher in EP HDFs than in LP HDFs, which may explain the reduced proliferation rate of LP HDFs compared to EP HDFs.

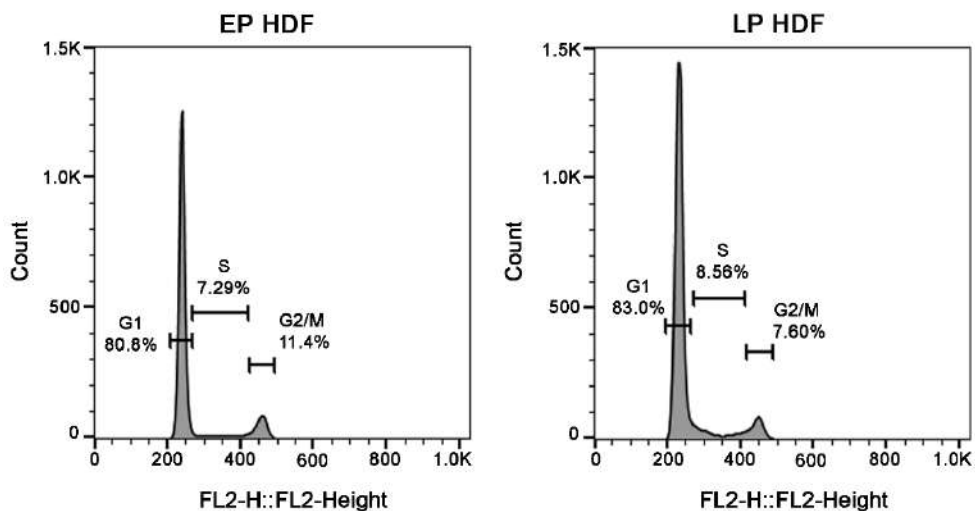


Figure 21. Flow cytometry analysis for cell cycle distribution of EP and LP HDFs. Representative diagram of cell cycle distribution of EP and LP HDFs. The percentages of cells in G1, S and G2/M are shown.

2. Evaluation of H3K4ox in cellular aging models

Post-translational modifications on the histone tail domain include acetylations, methylations, phosphorylations, ubiquitinations, sumoylations, glycosylations, etc. (Kouzarides, 2007; Lawrence et al., 2016). Recently, the K4-oxidated histone H3 form (H3K4ox), resulting from the deamination of H3K4me3 by the oxidase LOXL2, has been described as a novel epigenetic mark (Herranz et al., 2016). This modification has been found in heterochromatin regions and linked to the modulation of the DNA damage response pathway in triple-negative breast cancer cells (Cebrià-Costa et al., 2019). Considering that the aging process is accompanied by rearrangements of heterochromatin and impairments in the DDR, we aimed to study H3K4ox dynamics during aging. For this purpose, we employed the previously established models of OIS and cellular *in vitro* aging.

2.1. Analysis of H3K4ox, *LOXL2* and *LOXL1* in OIS and *in vitro* aging

To measure the global levels of H3K4ox in OIS, BJ fibroblasts in control conditions and after senescence induction were used. In addition, global levels of H3K4ox were also assayed in *in vitro* aged HDFs. Western blot analysis showed that global H3K4ox levels suffered from a strong decrease in senescent BJ fibroblasts compared to control BJ fibroblasts. Similarly, global H3K4ox levels were lower in LP HDFs compared to EP HDFs. However, the reduction of H3K4ox with culture time was found to be subtler than the one observed in OIS (**Figure 22A**).

Since LOXL2 has been described as the main oxidase involved in H3K4ox generation (Herranz et al., 2016), *LOXL2* expression levels were also analyzed in OIS and in *in vitro* aging by RT-qPCR. Senescent BJ fibroblasts displayed a lower amount of *LOXL2* mRNA compared to control BJ fibroblasts which correlated with the reduced levels of H3K4ox previously found. However,

LOXL2 expression remained unchanged between EP and LP HDFs (Figure 22B). Apart from *LOXL2*, expression level of *LOXL1*, another member of the LOX family that also conserves the C-terminal amine oxidase catalytic domain (Iturbide et al., 2015) was examined. As it occurred with *LOXL2*, *LOXL1* expression levels were significantly decreased in senescent BJ fibroblast compared to control BJ fibroblasts. In this case and differently from *LOXL2* expression, LP HDFs showed a reduced amount of *LOXL1* mRNA compared to EP HDFs (Figure 22C).

Therefore, OIS in BJ fibroblasts and *in vitro* aging of HDFs are associated with a reduction of global H3K4ox levels that correlates with decreased expression of both *LOXL1* and *LOXL2* in OIS and of *LOXL1* in *in vitro* aging. It is worth mentioning that these alterations were more evident in OIS than in *in vitro* aging, suggesting that oxidation events are significant during senescence and subtler during *in vitro* aging.

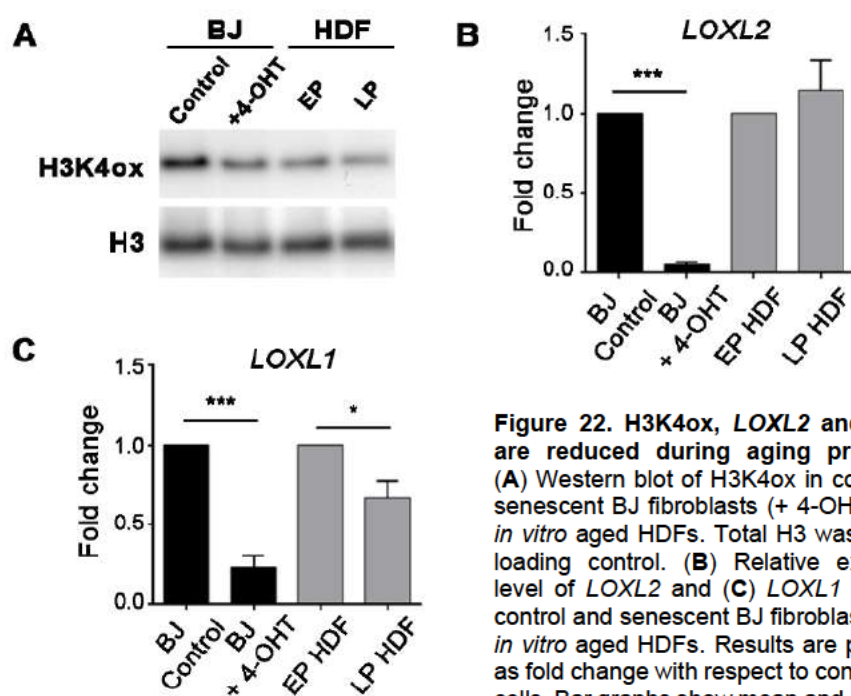


Figure 22. H3K4ox, *LOXL2* and *LOXL1* are reduced during aging processes. (A) Western blot of H3K4ox in control and senescent BJ fibroblasts (+ 4-OHT) and in *in vitro* aged HDFs. Total H3 was used as loading control. (B) Relative expression level of *LOXL2* and (C) *LOXL1* mRNA in control and senescent BJ fibroblasts and in *in vitro* aged HDFs. Results are presented as fold change with respect to control or EP cells. Bar graphs show mean and error bars SEM. P-values indicate the Student's t-test significance levels: * $p < 0.01$, *** $p < 0.001$.

2.2. Analysis of H3K4ox in heterochromatin regions

H3K4ox has been observed to concentrate mainly in heterochromatin regions suggesting a role of this mark in chromatin compaction (Cebrià-Costa et al., 2019). Reduced H3K4ox levels would lead to a more accessible chromatin state resulting in a sustained activation of the DDR (Cebrià-Costa et al., 2019). The results obtained in BJ fibroblasts showing a reduction of H3K4ox levels during senescence might reflect the restructuring of heterochromatic regions associated to senescence (Parry and Narita, 2016). Should this be the case, immunofluorescence could help to detect the nuclear sites in which oxidation events were enriched. Thus, we analyzed the presence of H3K4ox in SAHF by means of H3K4ox immunofluorescence staining combined with DAPI nuclear staining in BJ control and senescent fibroblasts.

Immunofluorescence experiments confirmed that H3K4ox showed a nuclear localization (**Figure 23A**). In addition, and in line with the western blot analysis, global H3K4ox levels were significantly reduced in BJ senescent fibroblast compared to BJ control cells (**Figure 23B**).

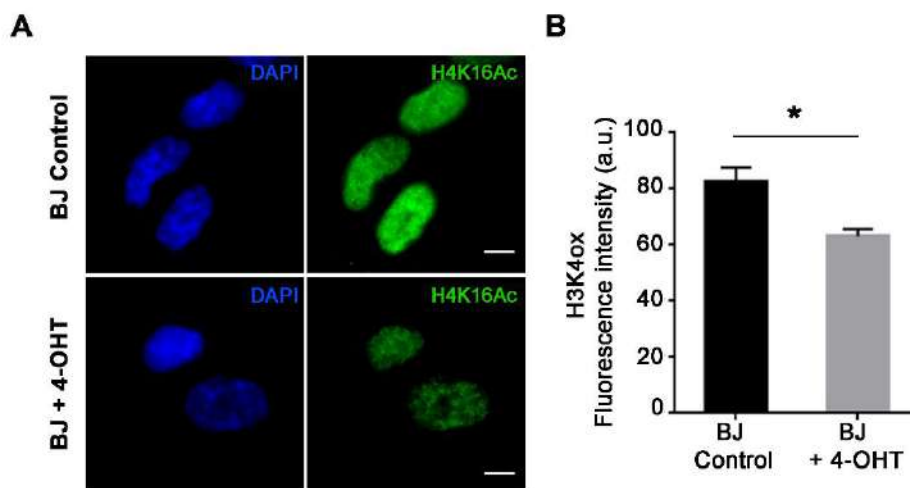


Figure 23. Nuclear localization of H3K4ox. (A) Immunostaining of H3K4ox (A488, green) in control and senescent (+ 4-OHT) BJ fibroblasts. Cell nuclei were stained with DAPI (blue). Scale bar: 10 μ m. (B) Quantification of H3K4ox fluorescence intensity in control and senescent BJ fibroblasts. Bar graph displays the mean fluorescence intensity per cell. Error bars indicate SEM. P-values indicate the Mann-Whitney test significance levels: * $p < 0.05$. A.u.: arbitrary units.

The identification of SAHF by DAPI staining in BJ senescent fibroblasts allowed the quantification of H3K4ox levels in these specific heterochromatin regions. Interestingly, H3K4ox levels were higher in SAHF than in the rest of the nucleus (**Figure 24A**). In fact, a significant increase of H3K4ox was observed in SAHF when compared to global levels of H3K4ox either in BJ control or BJ senescent fibroblasts (**Figure 24B**). Therefore, results showed that although global levels of H3K4ox were reduced after OIS, the analysis of H3K4ox restricted to SAHF confirmed a correlation between enhanced levels of H3K4ox and heterochromatin regions.

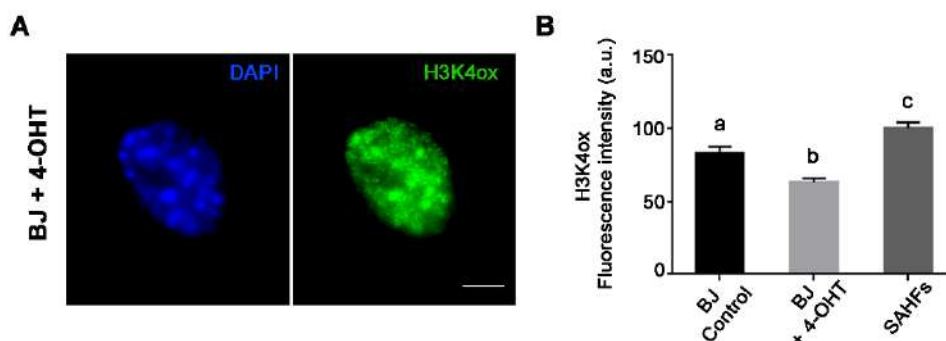


Figure 24. H3K4ox levels are enriched in SAHF. (A) Representative picture of H3K4ox immunostaining (A488, green) showing SAHF in BJ senescent (+ 4-OHT) fibroblasts. Cell nuclei were stained with DAPI (blue). Scale bar: 10 μ m. (B) Quantification of H3K4ox fluorescence intensity in control, senescent BJ fibroblasts and in SAHF. Bar graph displays the mean fluorescence intensity per cell. Error bars indicate SEM. Statistically significant differences are indicated by different letters (Kruskal-Wallis test with Dunn's correction). A.u.: arbitrary units.

Accumulation of H3K4ox in highly compacted heterochromatin regions was detected after CHIP-seq experiments in human breast cancer MDA-MB-231 cell line (Cebrià-Costa et al., 2019). Specifically, H3K4ox peaks were found within specific heterochromatin regions and lamina-associated domains that were subsequently validated by CHIP-qPCR (Cebrià-Costa et al., 2019). Thus, we next studied whether these heterochromatinic regions (Hits 1-5) were also oxidized in BJ senescent fibroblasts. CHIP-qPCR results showed that the selected hits were not overrepresented in BJ senescent fibroblasts, concluding that the MDA-MB-231-heterochromatin-enriched regions were not oxidized in BJ senescent fibroblasts (**Figure 25**). Moreover, the results showed that all the

regions analyzed in BJ senescent fibroblasts displayed reduced H3K4ox levels compared to control BJ cells. Thus, the presence of oxidation marks in these specific chromatin sites was different in MDA-MB-231 cells, senescent and control fibroblasts, suggesting that H3K4ox-enriched regions might be cell type-specific. Overall, the results here reported confirm the relationship between H3K4ox and heterochromatin: (1) SAHF of senescent BJ fibroblasts are especially H3K4ox-enriched sites, and (2) H3K4ox changes seems to be more relevant during OIS than in *in vitro* aging, which could correlate with the different heterochromatinization state of senescent and *in vitro* aged cells.

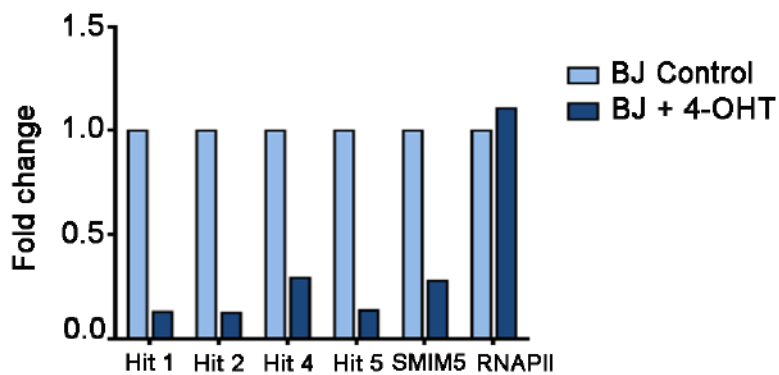


Figure 25. H3K4ox enriched regions are cell type specific. H3K4ox ChIP-qPCR for selected chromatin regions (Hit1 to Hit 5 and SMIM5) in control and senescent (+ 4-OHT) BJ fibroblasts. The sequence of RNA pol II promoter (RNAPII) was used as negative control. Data of qPCR amplifications were normalized to the input and to total H3 for H3K4ox and expressed as fold change relative to the data obtained in control BJ fibroblasts, which was set as 1.

3. Evaluation of H4K16 acetylation in cellular aging models

Histone acetylation is one of the best characterized and well-studied histone modifications. The addition of an acetyl group to lysine residues on the histones influences chromatin state by neutralizing the basic charge at unmodified lysine residues (Bannister and Kouzarides, 2011). Research in aging has reported changes in acetylation patterns in aged cells and tissues (Lu et al., 2011; Peleg et al., 2016); however, there is no universal acetylation state associated to aging. Due to its relevance in the recruitment of DDR proteins to DNA damaged sites and its dynamic pattern, H4K16Ac could be a promising histone mark linking aging to DNA repair regulation.

3.1. Analysis of H4K16Ac pattern in OIS

Cellular senescence has been associated with the reduction of active histone modifications such as lysine acetylation, which is known to contribute to DNA compaction during senescence (Parry and Narita, 2016; Peleg et al., 2016). To test whether H4K16Ac was reduced in OIS, immunofluorescence staining for H4K16Ac was performed in BJ fibroblasts in control conditions and after senescence induction (**Figure 26A**). For both cases, H4K16Ac analysis was restricted to the nuclei where colocalization with DAPI nuclear staining could be detected. Results showed how H4K16Ac levels were clearly decreased in BJ senescent fibroblasts compared to control BJ fibroblasts (**Figure 26A**). Indeed, quantitative fluorescence intensity measurements of H4K16Ac staining indicated a significant decrease of H4K16Ac signaling in BJ senescent fibroblasts in comparison to BJ control cells (**Figure 26B**). In addition, to confirm the immunofluorescence results, western blot analysis of H4K16Ac was carried out in control and senescent BJ fibroblasts. Consistently with immunofluorescence findings, western blot analysis showed lower levels of H4K16Ac in BJ senescent fibroblasts compared to control ones (**Figure 26C**).

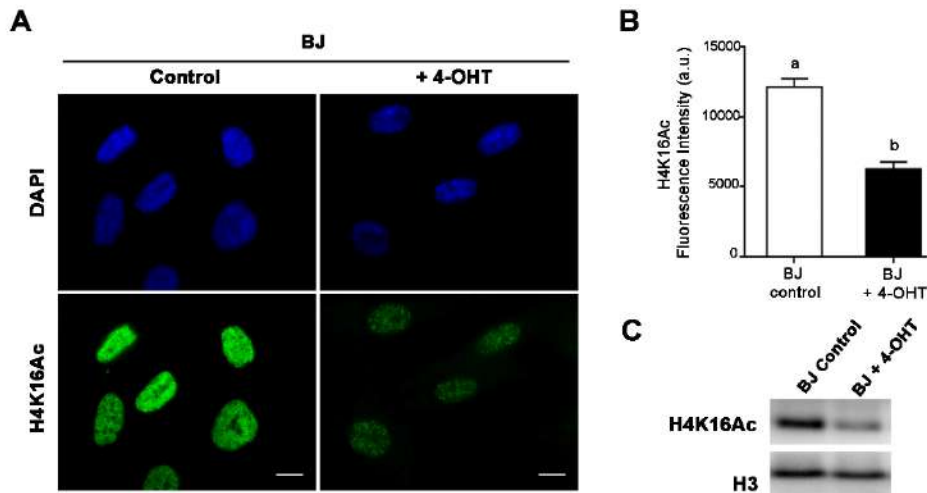


Figure 26. Age-associated reduction of H4K16Ac levels in senescent BJ fibroblasts. (A) Immunofluorescence staining of cell nuclei with H4K16Ac (A488, green) in control and in senescent (+ 4-OHT) BJ fibroblasts. Scale bar = 10 μ m. DAPI (blue) was used to counterstain cell nuclei. (B) Mean of corrected total cell fluorescence intensity of H4K16Ac in control and in senescent BJ fibroblasts. Error bars indicate SEM. Statistically significant differences are indicated by different letters (Mann-Whitney test). A.u.: arbitrary units (C) Western blot analysis of H4K16Ac in control and in senescent BJ fibroblasts. Total H3 was used as a loading control.

To gain insight into the molecular mechanism underlying H4K16Ac reduction with cellular senescence, the expression of *MOF*, the principal H4K16 histone acetyltransferase (Smith et al., 2005; Taipale et al., 2005), and the main H4K16 deacetylases, *SIRT1* and *SIRT2* (Vaquero et al., 2007a), were analyzed by RT-qPCR. Moreover, we also examined by RT-qPCR the expression of *TIP60*, the other histone acetyltransferase of H4K16 (Tang et al., 2013), and the expression of general histone deacetylases *HDAC1* and *HDAC2* (Miller et al., 2010).

In BJ fibroblasts, *MOF* mRNA levels remained unchanged after senescence induction. No significant differences were observed in *SIRT2* mRNA levels between BJ control and BJ senescent fibroblasts. However, *SIRT1* expression levels were significantly higher in BJ senescent fibroblasts than in their normal counterparts (Figure 27A). Regarding the expression of *TIP60*, *HDAC1* and *HDAC2*, no differences were detected between control and senescent BJ fibroblast for any of the mentioned genes (Figure 27B). Hence, the higher

expression levels of *SIRT1* during senescence seemed to indicate that diminution in H4K16Ac might be caused by an increased deacetylation activity performed by *SIRT1*.

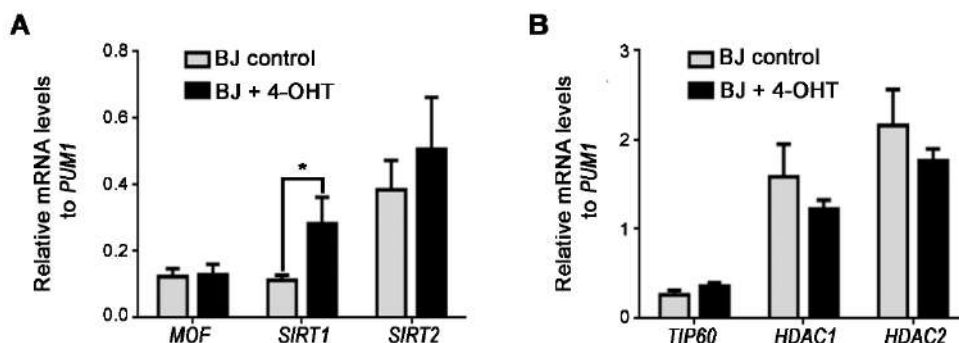


Figure 27. *SIRT1* is increased in OIS. (A) Relative expression levels of *MOF*, *SIRT1* and *SIRT2* with respect to housekeeping gene *PUM1* in control and senescent (+ 4-OHT) BJ fibroblasts. (B) Relative expression levels of *TIP60*, *HDAC1* and *HDAC2* with respect to housekeeping gene *PUM1* in control and senescent BJ fibroblasts. Bar graphs show mean and error bars indicate SEM. P-values indicate the Welch's t-test significance levels: *p<0.05.

3.2. Analysis of H4K16Ac pattern during *in vitro* aging

Next, global H4K16Ac levels were also measured during *in vitro* aging. To address this purpose, immunofluorescence of H4K16Ac was performed in HDFs at EP and LP. Similar to BJ senescent fibroblasts, immunostainings showed that LP HDFs exhibited less H4K16Ac than EP HDFs (**Figure 28A**). Supporting these evidences, quantitative fluorescence intensity measurements of H4K16Ac immunostaining displayed a significant decrease of H4K16Ac in LP HDFs compared to EP HDFs (**Figure 28B**). In order to validate these results, western blot analysis of H4K16Ac was also performed in *in vitro* aged HDFs. In accordance with immunofluorescence observations, western blot analysis showed lower H4K16Ac levels in LP HDFs compared to EP HDFs (**Figure 28C**).

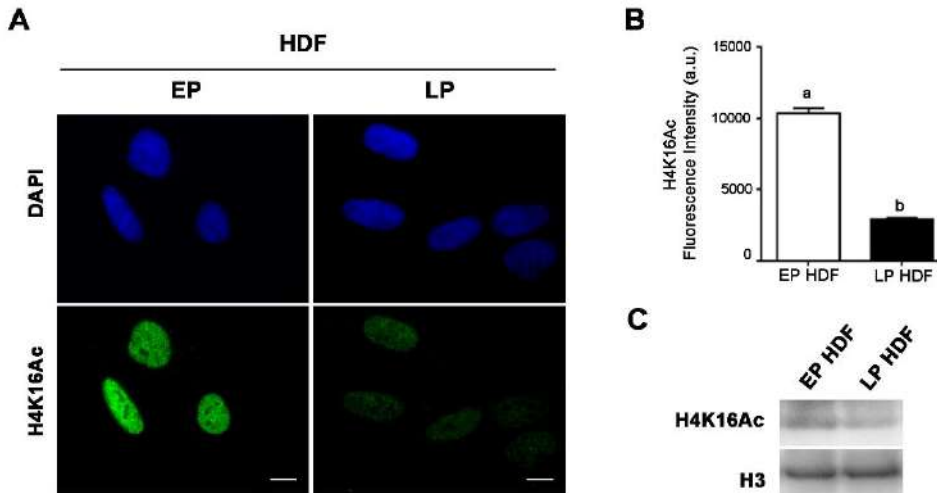


Figure 28. Age-associated reduction of H4K16Ac levels in *in vitro* aged HDFs. (A) Immunofluorescence staining of cell nuclei with H4K16Ac (A488, green) in EP and LP HDFs. Scale bar = 10 µm. DAPI (blue) was used to counterstain cell nuclei. (B) Mean of corrected total cell fluorescence intensity of H4K16Ac in *in vitro* aged HDFs. Error bars indicate SEM and statistically significant differences are indicated by different letters (Mann-Whitney test). A.u.: arbitrary units. (C) Western blot analysis of H4K16Ac in *in vitro* aged HDFs. Total H3 was used as a loading control.

To study the nature of the reduction of H4K16Ac with *in vitro* aging, *MOF*, *SIRT1* and *SIRT2*, as well as the expression of *TIP60*, *HDAC1* and *HDAC2* were analyzed by RT-qPCR. Contrary to OIS, *SIRT1* and *SIRT2* mRNA levels remained constant in the *in vitro* aging model. Nevertheless, *MOF* expression decreased with time in culture, being significantly reduced in LP HDFs compared to EP HDFs (**Figure 29A**). On the other hand, expression of *TIP60*, *HDAC1* and *HDAC2* did not significantly change during *in vitro* aging as it also occurred in OIS (**Figure 29B**). Taken together, these results identify decreased H4K16 acetylation as a common marker across different cellular aging models. Nevertheless, the mechanisms involved in age-related H4K16Ac reduction were differently altered in cellular senescence and *in vitro* aging. While in OIS, reduction in H4K16Ac might be caused by enhanced deacetylation activity due to increased *SIRT1* levels, reduction of H4K16Ac during *in vitro* aging could be consequence of diminished acetylation activity due to decreased *MOF* levels.

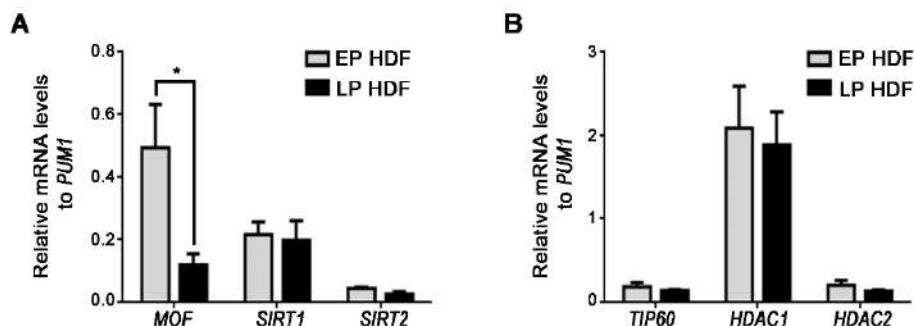


Figure 29. *MOF* is decreased during *in vitro* aging. (A) Relative expression levels of *MOF*, *SIRT1* and *SIRT2* with respect to housekeeping gene *PUM1* in *in vitro* aged HDFs. (B) Relative expression levels of *TIP60*, *HDAC1* and *HDAC2* with respect to housekeeping gene *PUM1* in *in vitro* aged HDFs. Bar graphs show mean and error bars indicate SEM. P-values indicate the Welch's t-test significance levels: * $p < 0.05$.

4. Contribution of H4K16 acetylation to DSB repair in *in vitro* aging

Accumulation of DSBs during *in vitro* cellular aging has been observed in different cell types (Sedelnikova et al., 2008; Hernández et al., 2013). The accumulation of these type of unrepaired lesions has been associated with a delay in 53BP1 recruitment to DSB sites that would impair proper DNA repair (Hernández et al., 2013). In this regard, it has been described that H4K16Ac plays a prominent role in the regulation of 53BP1 foci formation by impeding the binding of 53BP1 to H4K20me2 at short times after DNA damage induction (Hsiao and Mizzen, 2013; Tang et al., 2013). The changes of H4K16Ac levels in *in vitro* aged cells confirmed H4K16Ac as an age-related histone mark and led us to hypothesize that these alterations could impact on DNA damage repair efficiency with age. Thus, the influence of H4K16 acetylation status on age-associated DSB repair efficiency and 53BP1 recruitment ability was investigated.

4.1. H4K16 acetylation state after DSB induction

The dynamic pattern of H4K16Ac associated with DNA damage induction, makes H4K16Ac a DNA damage responsive histone mark (Miller et al., 2010; Hsiao and Mizzen, 2013; Tang et al., 2013). In order to investigate whether these changes were altered by the *in vitro* aging process, acetylation of H4K16 was analyzed after DSB induction in EP and LP HDFs.

Hence, H4K16Ac levels were analyzed in EP and LP HDFs at 30 min, 120 min and 24 h after exposure to 5 Gy of γ -rays. For this purpose, western blot analysis of H4K16Ac and γ H2AX, as a marker of DSBs, was performed (**Figure 30**). Results showed that in both EP and LP HDFs, γ H2AX levels strongly increased at 30 and 120 min post-irradiation (PI) indicating the presence of unresolved DSBs. At 24 h PI, γ H2AX levels returned to pre-irradiation levels, probably as consequence of DNA repair. Regarding H4K16Ac, western blot analysis in EP HDFs showed a decrease of H4K16Ac levels immediately after irradiation (30 min) followed by a recovery up to control levels at longer times (120 min and 24 h). Instead, LP HDFs displayed an overall lower level of H4K16Ac than EP cells and showed no changes with time after DNA damage induction.

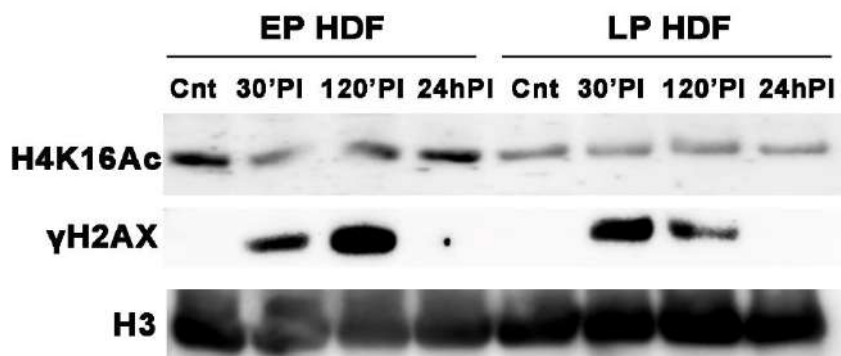


Figure 30. H4K16 acetylation shows different behaviors in early and late passage HDFs after DSB induction. Western blot analysis of H4K16Ac and γ H2AX in EP and LP HDFs at 30 min, 120 min and 24 h PI with 5 Gy. Total H3 was used as a loading control.

To confirm these data, analysis of H4K16 acetylation levels after DSB induction was also performed in EP and LP HDFs by immunofluorescence (**Figure 31A**). Cells were exposed to 2 Gy of γ -rays and H4K16Ac levels were analyzed at 30 and 120 min PI. All values of fluorescence intensity were normalized with respect to the control value obtained before irradiation (**Figure 31B**). In EP HDFs, levels of H4K16 acetylation dropped at short PI times, but at 120 min after irradiation H4K16Ac levels recovered and reached values similar to control H4K16Ac levels. However, in LP HDFs, levels of H4K16 acetylation slightly increased after irradiation but they ended up reaching control values.

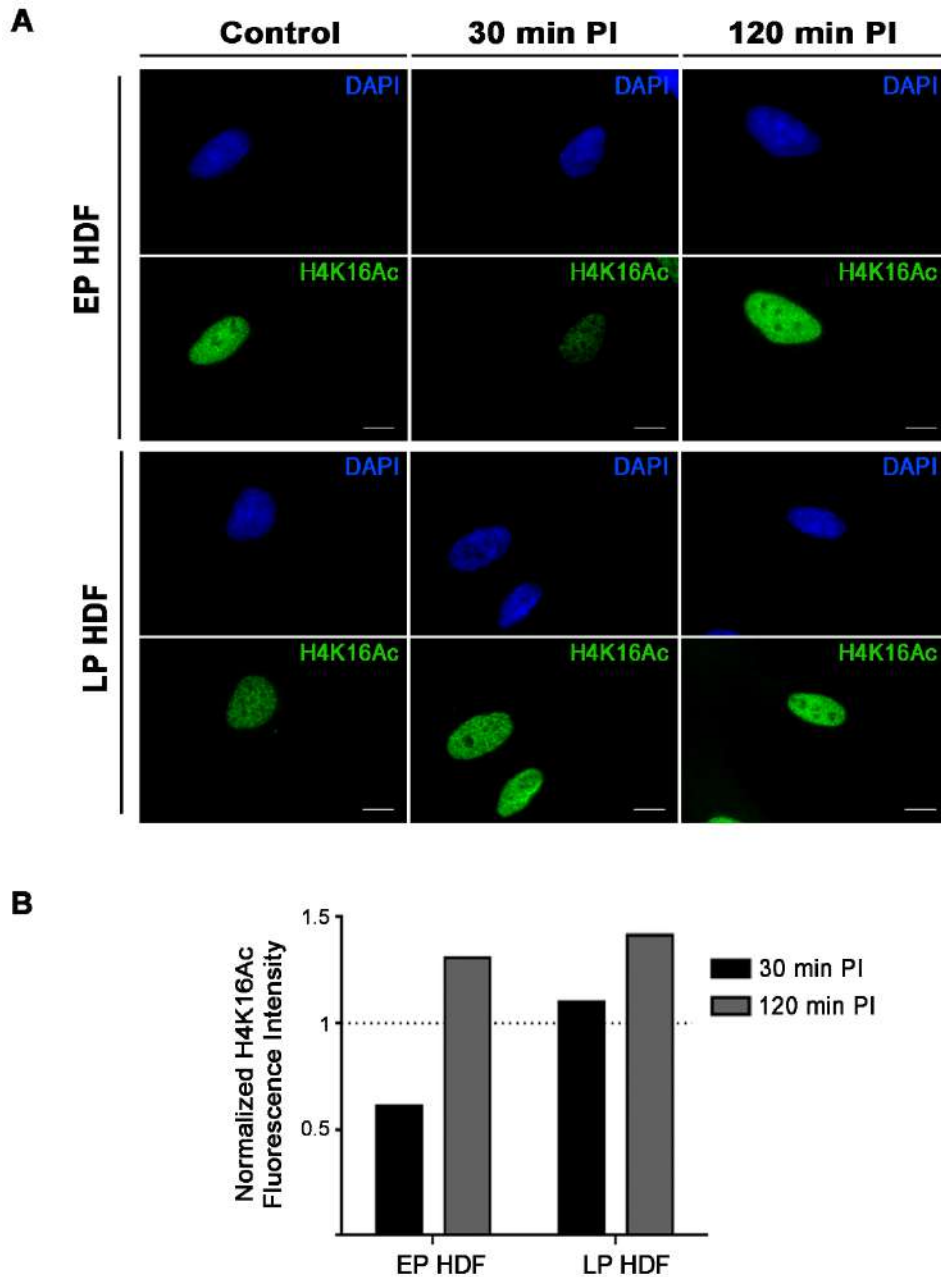


Figure 31. Validation of the different H4K16Ac dynamics after DSB induction in EP and LP HDFs by immunofluorescence. (A) Representative pictures of immunofluorescence staining of H4K16Ac (A488, green) in EP and LP HDFs at 30 min and 120 min PI with 2 Gy. Cell nuclei were stained with DAPI (Blue). Scale bar = 10 μ m. (B) Quantification of fluorescence intensity of H4K16Ac staining in EP and LP HDFs at 30 min and 120 min PI with 2 Gy. Means of corrected total cell fluorescence intensity of H4K16Ac were normalized with respect to the value obtained before irradiation which was given a value of 1.

According to the results described in section 3.2., diminution of H4K16Ac levels during *in vitro* aging correlated with diminution in *MOF* expression levels. Therefore, to investigate whether the different H4K16Ac dynamics after DBS induction observed in EP and LP HDFs were also correlated with changes in *MOF* expression, RT-qPCR was performed at different PI times (**Figure 32**). EP and LP HDFs were exposed to 2 Gy of γ -rays and *MOF* expression levels were analyzed at 30 and 120 min post-irradiation. RT-qPCR results showed that *MOF* mRNA levels followed the same tendency as H4K16Ac in EP and LP cells after irradiation. In EP HDFs, *MOF* expression was significantly reduced at short times PI (30 min) and recovered to control conditions at longer times (120 min). However, in LP HDFs, *MOF* expression was generally lower than in EP cells and showed no significant variations after irradiation.

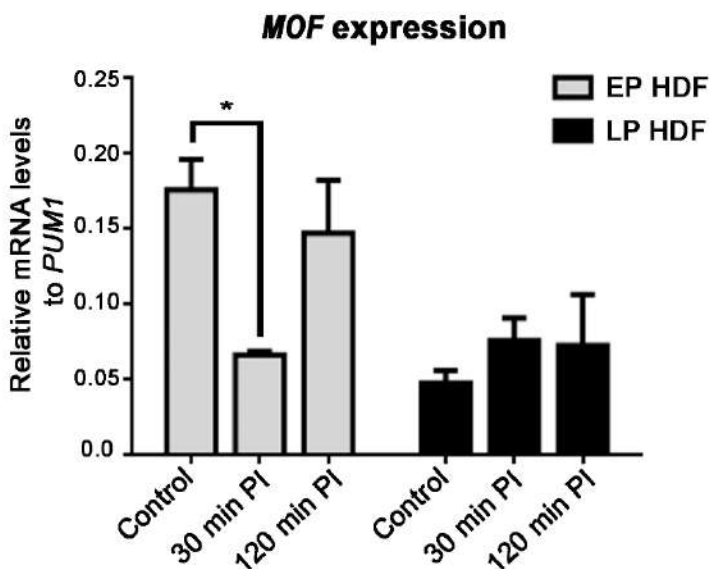


Figure 32. MOF expression varies in early and late passage HDFs after DSB induction. Relative expression level of *MOF* with respect to housekeeping gene *PUM1* in EP and LP HDFs at 30 min and 120 min PI after 2 Gy irradiation. Bar graphs show mean and error bars indicate SEM. P-values indicate the significance levels of the one-way ANOVA with Tukey's correction test: * $p < 0.05$.

Altogether, these findings indicate that while H4K16Ac levels are higher in EP cells and respond to DSB induction with a biphasic pattern, they are always lower in LP cells, in which they remain mostly unaltered in response to radiation. It is worth noting that in both cases H4K16Ac followed the same behavior as *MOF*. These results confirm H4K16Ac as a DNA damage responsive mark with dynamics that differ in an age-dependent manner.

4.2. Analysis of H4K16Ac levels and its involvement in 53BP1 recruitment

Considering that H4K16Ac behavior differs between EP and LP HDFs after DNA damage induction, it is possible that these age-associated changes could affect the DDR efficiency. For this purpose, we analyzed γ H2AX foci formation, as an indirect measure of DSBs, and assessed the presence of 53BP1 foci at these γ H2AX foci along with H4K16Ac levels in the whole nucleus before and after treating EP and LP HDFs with the DSB inducer bleocin. To measure these parameters, H4K16Ac, γ H2AX and 53BP1 immunodetection were performed in parallel in both bleocin-treated and untreated HDFs over different culture passages.

In the case of untreated HDFs, a gradual decrease of 53BP1/ γ H2AX colocalization ratio was detected as the number of culture passages increased (**Figure 33A, 33C**). Colocalization analysis revealed that the ratio between 53BP1 and γ H2AX was almost 0.9 in the earliest passage (p5) while it decreased down to 0.4 in the latest passage HDFs (p30) (**Figure 33C**). Consequently, recruitment of 53BP1 to γ H2AX foci suffered from a reduction of about 50% with *in vitro* aging. Regarding H4K16Ac levels, they significantly decreased between EP (p5, p10 and p15) and LP HDFs (p20, p25 and p30) (**Figure 33B, 33D**). Therefore, the decrease in H4K16Ac levels correlated with a reduction in 53BP1 recruitment to basal γ H2AX-labelled DSBs with *in vitro* aging in HDFs (p-value=0.020; $R^2=0.778$) (**Figure 33E**).

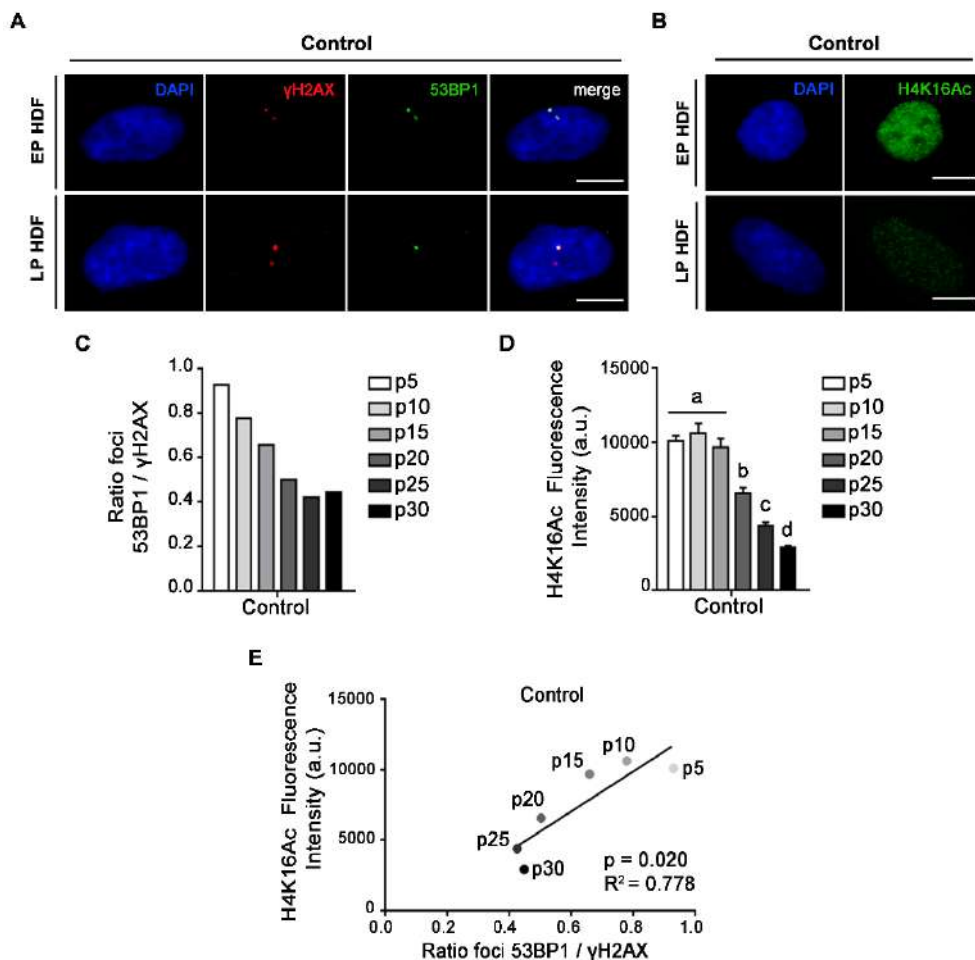


Figure 33. Age-associated impairments in 53BP1 recruitment to basal DSBs correlate with decreased levels of H4K16 acetylation. (A) Double immunofluorescence detection of γ H2AX (Cy3, red) and 53BP1 (A488, green) foci in EP and LP HDFs in control conditions. Merged panel shows colocalization of 53BP1 with γ H2AX foci. Cell nuclei were stained with DAPI (blue). Scale bar = 10 μ m. (B) Immunofluorescence staining of cell nuclei with H4K16Ac (A488, green) in EP and LP HDFs in control conditions. Cell nuclei were stained with DAPI (blue). Scale bar = 10 μ m. (C) Ratios of 53BP1 and γ H2AX foci colocalization in control HDFs at different culture passages (p5-p30). (D) Mean of corrected total cell fluorescence intensity of H4K16Ac in control HDFs at different culture passages (p5 to p30). Error bars indicate SEM and statistically significant differences are indicated by different letters (Kruskal-Wallis test with Dunn's correction). A.u.: arbitrary units. (E) Correlation between H4K16Ac fluorescence intensity and 53BP1/ γ H2AX foci colocalization ratio of HDFs at different culture passages (p5-p30). Correlation coefficient (R^2) and p-value were obtained after a linear regression analysis.

Then, analysis of H4K16Ac levels and 53BP1/ γ H2AX colocalization ratio in EP and LP HDFs was performed after DSB induction with radiomimetic bleocin. Strikingly, the colocalization ratio of 53BP1/ γ H2AX foci after a 1h bleocin treatment was ~ 0.7 in both early and late passage HDFs (**Figure 34A, 34C**). Thus, after DSBs induction the 53BP1/ γ H2AX ratio slightly decreased in EP cells while it slightly increased in LP cells, smoothing the differences existing among passages in control conditions (**Figure 34C**). Considering H4K16Ac levels, a very similar pattern to the one observed for the colocalization ratio of 53BP1/ γ H2AX was obtained. After DSB induction with bleocin, H4K16Ac levels tended to decrease in EP HDFs and to increase in LP HDFs compared to untreated EP and LP HDFs (**Figure 34B, 34D**). Thus, after DSBs induction, H4K16Ac levels seemed to reach a steady state, whose value was common for EP and LP HDFs. Consequently, after bleocin treatment, no linear correlation between the colocalization ratio of 53BP1/ γ H2AX and H4K16Ac levels was found during HDFs *in vitro* aging (p -value=0.788; $R^2=0.022$) (**Figure 34E**).

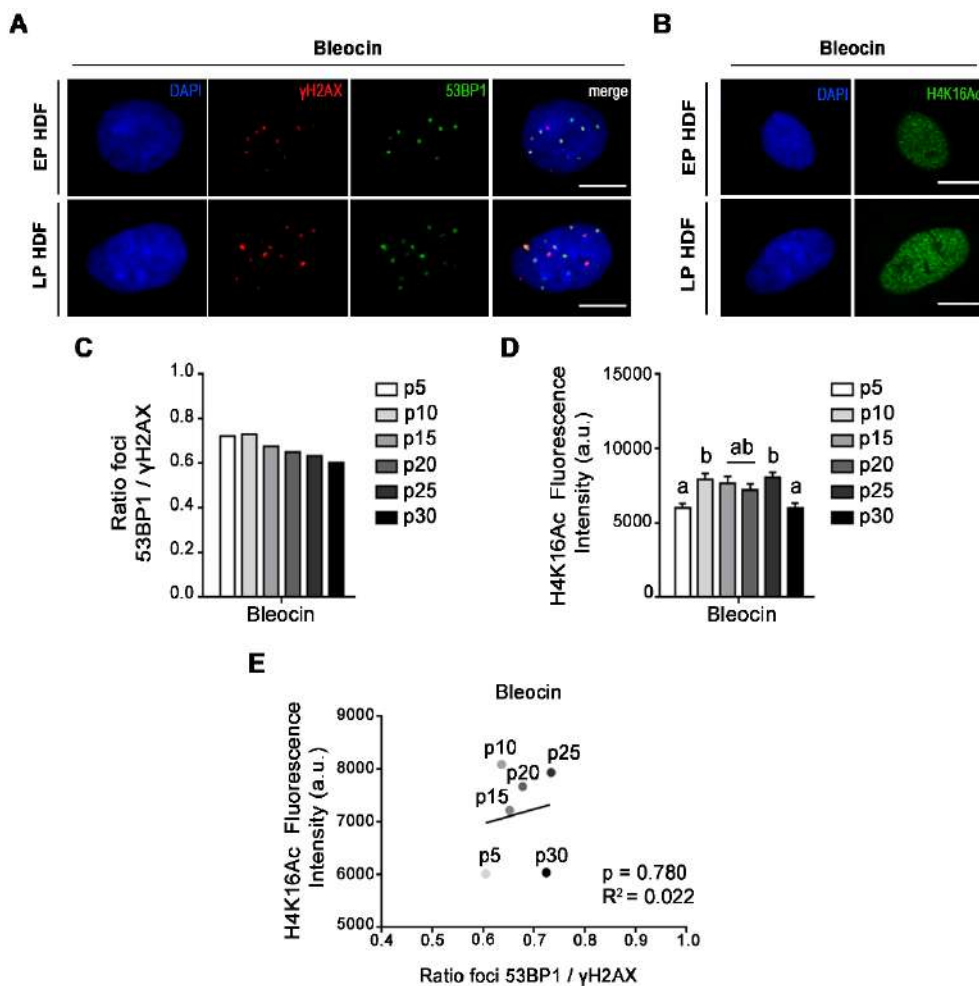


Figure 34. Aged HDFs display an increase in both 53BP1/ γ H2AX colocalization and H4K16Ac levels after DSB induction. (A) Double immunofluorescence detection of γ H2AX (Cy3, red) and 53BP1 (A488, green) foci in EP and LP HDFs after bleocin treatment. Cell nuclei were stained with DAPI (blue). Merged panel shows 53BP1 foci colocalizing with γ H2AX foci. Scale bar = 10 μ m. (B) Immunofluorescence staining of cell nuclei with H4K16Ac (A488, green) in EP and LP HDFs after bleocin treatment. Scale bar = 10 μ m. (C) Ratios of 53BP1 and γ H2AX foci colocalization in bleocin-treated HDFs at different culture passages (p5-p30). (D) Mean of corrected total cell fluorescence intensity of H4K16Ac in bleocin-treated HDFs at different culture passages (p5 to p30). Error bars indicate SEM and statistically significant differences are indicated by different letters (Kruskal-Wallis test with Dunn's correction). A.u.: arbitrary units. (E) Correlation between H4K16Ac fluorescence intensity and 53BP1/ γ H2AX foci colocalization ratio of HDFs at different culture passages (p5-p30). Correlation coefficient (R^2) and p-value were obtained after a linear regression analysis.

To confirm that the increase of 53BP1/ γ H2AX colocalization ratio in LP HDFs after DNA damage induction was independent from the source of the DNA damage, an analysis of 53BP1- γ H2AX colocalization ratio by using 2 Gy of γ -rays irradiation as DSB source was carried out (**Figure 35A, 35B**). Supporting the previous evidences obtained after bleocin treatment 53BP1/ γ H2AX colocalization ratio barely changed after irradiation exposure in EP HDFs (p10); however, it increased in LP HDFs in comparison to control conditions.

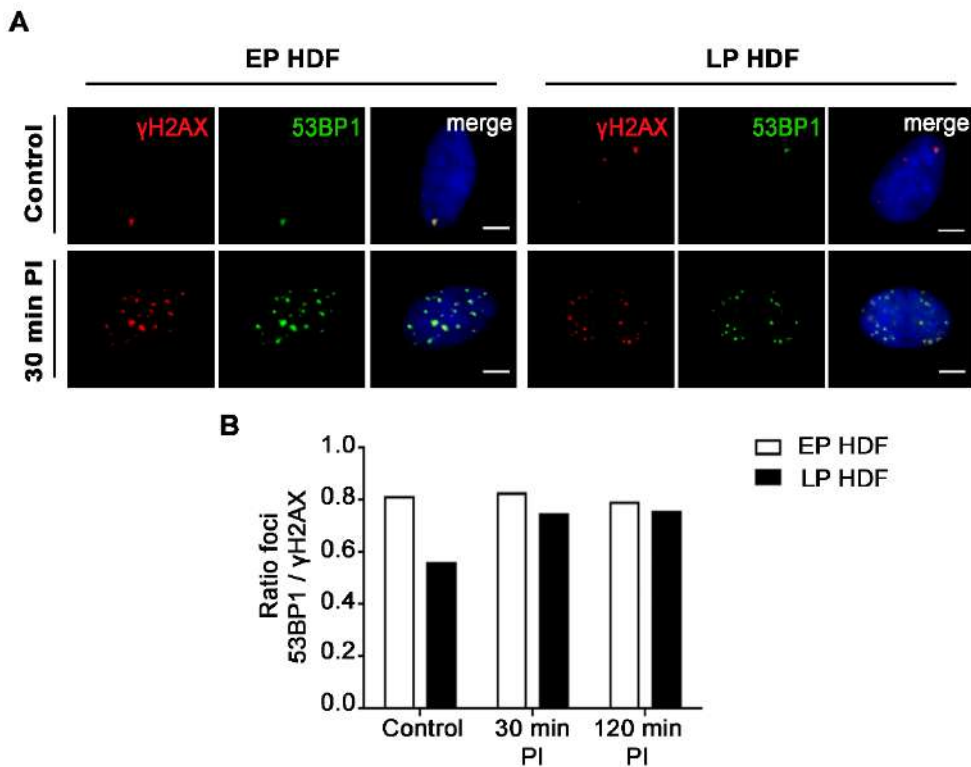


Figure 35. 53BP1 recruitment is differently affected in early and late passage HDFs after γ irradiation. (A) Double immunofluorescence detection of γ H2AX (Cy3, red) and 53BP1 (A488, green) foci in EP and LP HDFs in control conditions and 30 min PI with 2 Gy. Merged panel shows γ H2AX foci colocalizing with 53BP1 foci. Cell nuclei were stained with DAPI (blue). Scale bar = 2.5 μ m. (B) Ratios of 53BP1 and γ H2AX foci colocalization in EP and LP HDFs in control conditions and at 30 min and 120 min PI with 2 Gy.

Taken together, the data obtained suggest that the proper recruitment of 53BP1 to newly generated DSBs might require a specific level of H4K16Ac. This could explain why after DNA damage induction, the increased recruitment of 53BP1 to γ H2AX foci in LP HDFs is associated with an increase in H4K16 acetylation up to a similar level to that of EP cells.

4.3. Effects of H4K16 hyperacetylation on 53BP1 recruitment

After DSBs induction aged HDFs displayed an increased colocalization ratio of 53BP1 and γ H2AX which was accompanied by an increase in H4K16Ac levels. Since enhanced 53BP1 recruitment seemed to be correlated with higher levels of H4K16Ac in LP HDFs, we hypothesized that hyperacetylation of H4K16 could improve 53BP1 recruitment after DSB generation. To elucidate this question, 53BP1/ γ H2AX colocalization was analyzed after bleocin-mediated induction of DSBs in hyperacetylated HDFs. To hyperacetylate HDFs, cells were firstly treated with trichostatin A (TSA), which is a HDAC class I, II and IV inhibitor (Kim and Bae, 2011). Then, H4K16Ac, γ H2AX and 53BP1 immunodetections were parallelly performed in EP and LP HDFs.

Firstly, it was confirmed that the levels of H4K16Ac were significantly higher in HDFs treated with TSA in comparison to untreated HDFs (**Figure 36A, 36B**). It is worth mentioning that the increase in H4K16 acetylation levels was less pronounced in LP cells than in EP HDFs. Regarding 53BP1/ γ H2AX colocalization analysis, and contrary to what we expected, the colocalization ratio of 53BP1/ γ H2AX foci was reduced in all culture passages of TSA-treated cells after DSB induction with bleocin (**Figure 36C**).

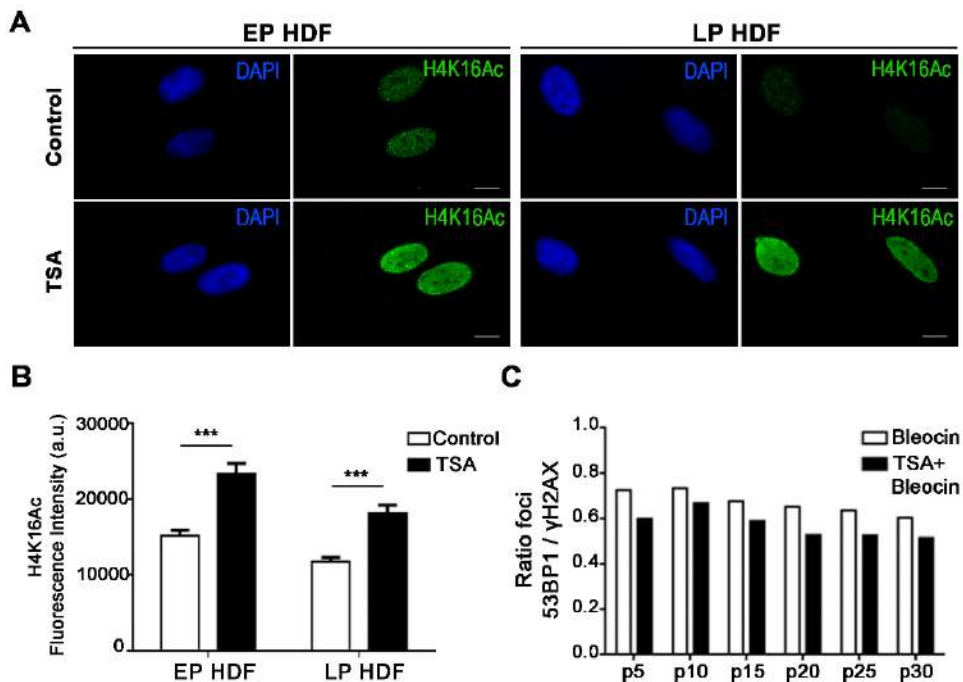


Figure 36. H4K16 hyperacetylation after TSA treatment does not increase 53BP1 recruitment following DSB induction. (A) Immunofluorescence staining of cell nuclei with H4K16Ac (A488, green) in EP and LP HDFs in control conditions and after TSA treatment. DAPI (blue) was used to stain cell nuclei. Scale bar = 10 μ m. (B) Mean of corrected total cell fluorescence intensity of H4K16Ac in control and TSA-treated EP and LP HDFs. Error bars indicate SEM and statistically significant differences are indicated with asterisks (Mann-Whitney test; *** p <0.001). A.u.: arbitrary units. (C) Ratios of 53BP1 and γ H2AX foci colocalization in bleocin and TSA+bleocin-treated HDFs at different culture passages (p5-p30).

TSA is a general inhibitor of HDACs, while sirtuins are the major HDACs involved in H4K16Ac deacetylation (Vaquero et al., 2007a). Therefore, it was tested whether specific inhibition of sirtuins would render different results regarding the 53BP1/ γ H2AX colocalization ratio. For this purpose, cells were treated with nicotinamide (NAM), a specific inhibitor of sirtuins (Avalos et al., 2005), before DSB induction with bleocin. Again, and as expected, the levels of H4K16Ac were significantly higher in NAM-treated HDFs in comparison to control HDFs and both EP and LP cells reached similar levels of H4K16 acetylation (Figure 37A, 37B). After NAM treatment and DSB induction, 53BP1/ γ H2AX colocalization ratio did not change (Figure 37C). When cells were treated with both hyperacetylators NAM and TSA, in agreement with the

results obtained after TSA treatment, the 53BP1/ γ H2AX ratio dropped again in both EP and in LP cells (**Figure 37C**).

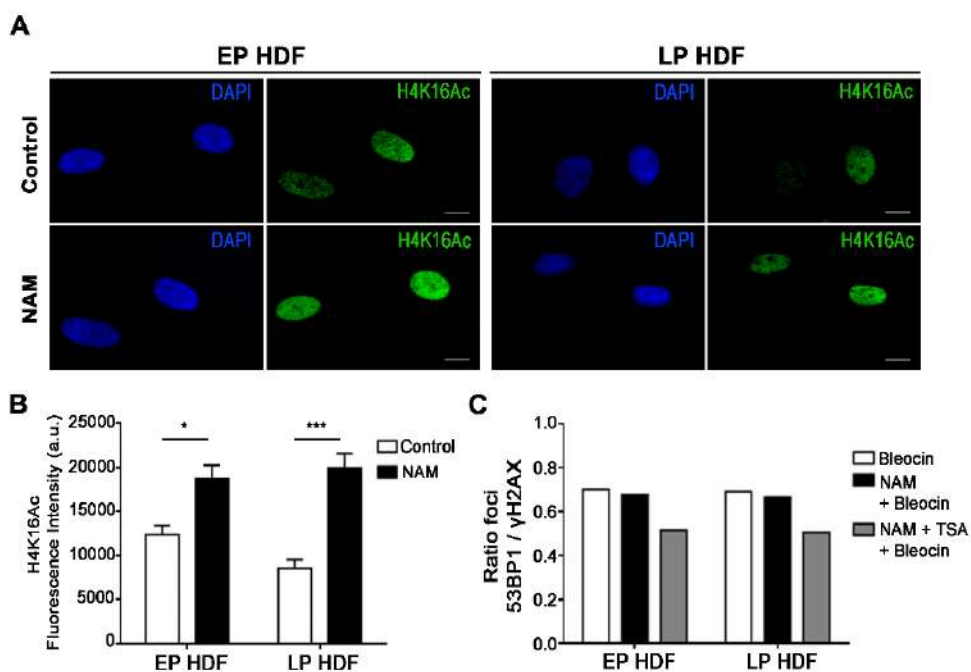


Figure 37. H4K16 hyperacetylation due to NAM treatment does not improve 53BP1 recruitment following DSB induction. (A) Immunofluorescence staining of cell nuclei with H4K16Ac (A488, green) in EP and LP HDFs in control conditions and NAM treatment. DAPI (blue) was used to stain cell nuclei. Scale bar = 10 μ m. (B) Mean of corrected total cell fluorescence intensity of H4K16Ac in control and NAM-treated EP and LP HDFs. Error bars indicate SEM and asterisks indicate statistically significant differences (Mann-Whitney test; *** p <0.001; * p <0.05). A.u.: arbitrary units. (C) Ratios of 53BP1/ γ H2AX foci colocalization in EP and LP HDFs treated with bleocin, NAM+bleocin and NAM+TSA+bleocin.

These results suggest that hyperacetylation leads to different effects depending on the agent used: while TSA treatment diminishes the 53BP1/ γ H2AX colocalization ratio in EP and LP HDFs, this parameter is not affected by NAM treatment. Nevertheless, our findings show that in neither case, artificial hyperacetylation of H4K16 improves the 53BP1/ γ H2AX ratio. Instead, the results support the notion that after DSB induction H4K16Ac reaches a specific level which is optimum for a proper recruitment of 53BP1 to DSBs. To reach this value, acetylation levels are only slightly downregulated in EP cells, while

in LP cells acetylation levels must increase in order to ensure a proper recruitment of 53BP1 to DSBs after DNA damage induction.

4.4. Effects of H4K16 hypoacetylation on 53BP1 recruitment

As hyperacetylation did not improve 53BP1 recruitment at γ H2AX neither in control conditions nor after DSB induction in LP HDFs, the need for a specific acetylation level for an appropriate recruitment of 53BP1 to DSBs was tested under hypoacetylation conditions. In this scenario, an impaired recruitment of 53BP1 to γ H2AX-labelled DSBs would be expected. In order to induce a global reduction of H4K16 acetylation, we silenced endogenous *MOF* using a lentiviral vector expressing a short hairpin RNA (shRNA) that targeted *MOF* (shMOF). *MOF* is the major acetyltransferase of H4K16 (Smith et al., 2005; Taipale et al., 2005) and our previous results identified changes in *MOF* expression to be directly associated with the age-related reduction of H4K16Ac during *in vitro* aging.

Once cells were infected with shMOF, silencing of *MOF* was checked with different approaches. Using RT-qPCR, we confirmed that both EP and LP HDFs infected with shMOF showed down-regulation of *MOF* expression levels compared to those cells infected with the control shRNA scramble (shScramble) (**Figure 38A**). In addition, western blot analysis showed reduced levels of *MOF* in HDFs after *MOF* depletion in comparison to the scramble control (**Figure 38B**). Besides, H4K16Ac levels were evaluated in HDFs transduced with shScramble and shMOF by immunofluorescence. Consistent with the fact that *MOF* is the major acetyltransferase of H4K16 in mammals, lower levels of H4K16Ac were observed after *MOF* inhibition in EP and LP HDFs compared to the scramble control (**Figure 38C**).

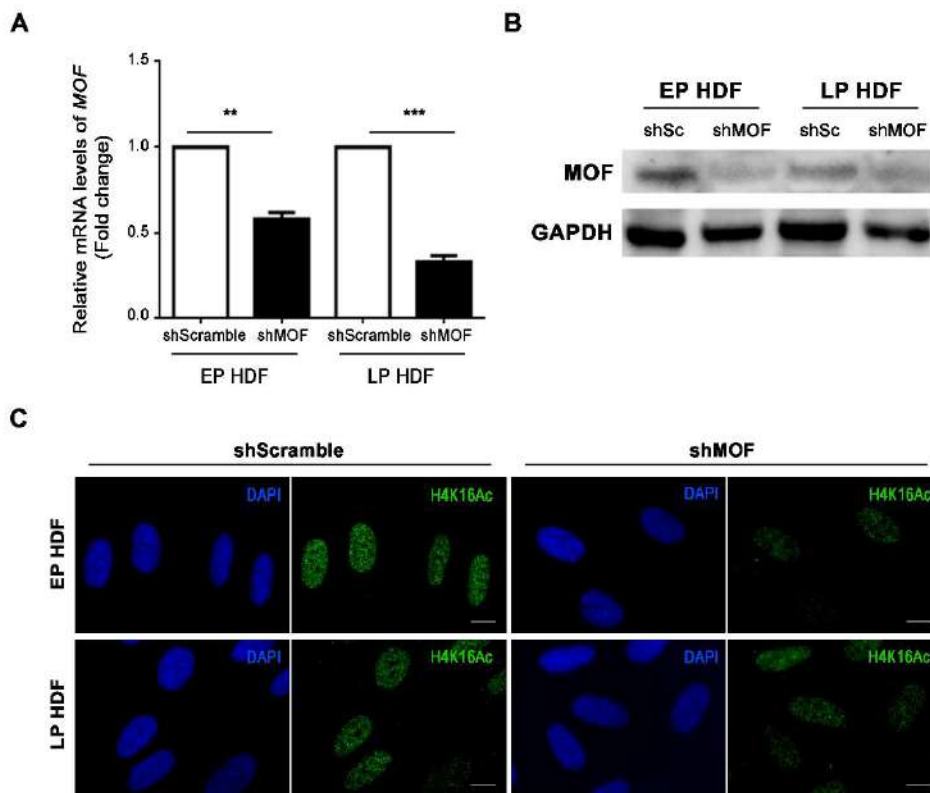


Figure 38. Validation of *MOF* depletion in EP and LP HDFs infected with *MOF* shRNA. (A) Relative expression level of *MOF* in EP and LP HDFs infected with shScramble and shMOF. Data are presented as fold change with respect to shScramble cells. Bar graphs show mean. Error bars indicate SEM. Asterisks indicate significant p-values obtained from Welch's t-test (** $p < 0.01$, *** $p < 0.001$). (B) Western blot analysis of *MOF* in EP and LP HDFs infected with shScramble (shSc) and shMOF. GAPDH was used as a loading control. (C) Immunofluorescence staining of cell nuclei with DAPI (blue) and H4K16Ac (A488, green) in EP and LP HDFs infected with shScramble and shMOF. Scale bar = 10 μ m.

To examine the effect of *MOF* silencing, and thus the effect of subsequent hypoacetylation of H4K16 on 53BP1 recruitment efficiency, 53BP1/ γ H2AX colocalization ratio was assessed by a triple immunostaining of 53BP1, γ H2AX and H4K16Ac. These analysis were firstly performed EP and LP HDFs transduced with shScramble and shMOF in control conditions. As expected, infected cells with shMOF showed significantly reduced levels of H4K16Ac compared to control cells infected with shScramble (Figure 39A, 39B). Regarding DSBs, a significantly increased number of γ H2AX foci was observed both in EP and LP *MOF*-depleted HDFs, which was not accompanied by an

equivalent increase of 53BP1 foci (**Figure 39A, 39C**). As a consequence, the 53BP1/ γ H2AX colocalization ratio was certainly decreased after *MOF* depletion in EP and LP HDFs (**Figure 39C**). These findings show that *MOF* depletion results in increased generation of DSBs that are not able to properly recruit 53BP1, suggesting that *MOF* silencing could lead to impairments in 53BP1 recruitment.

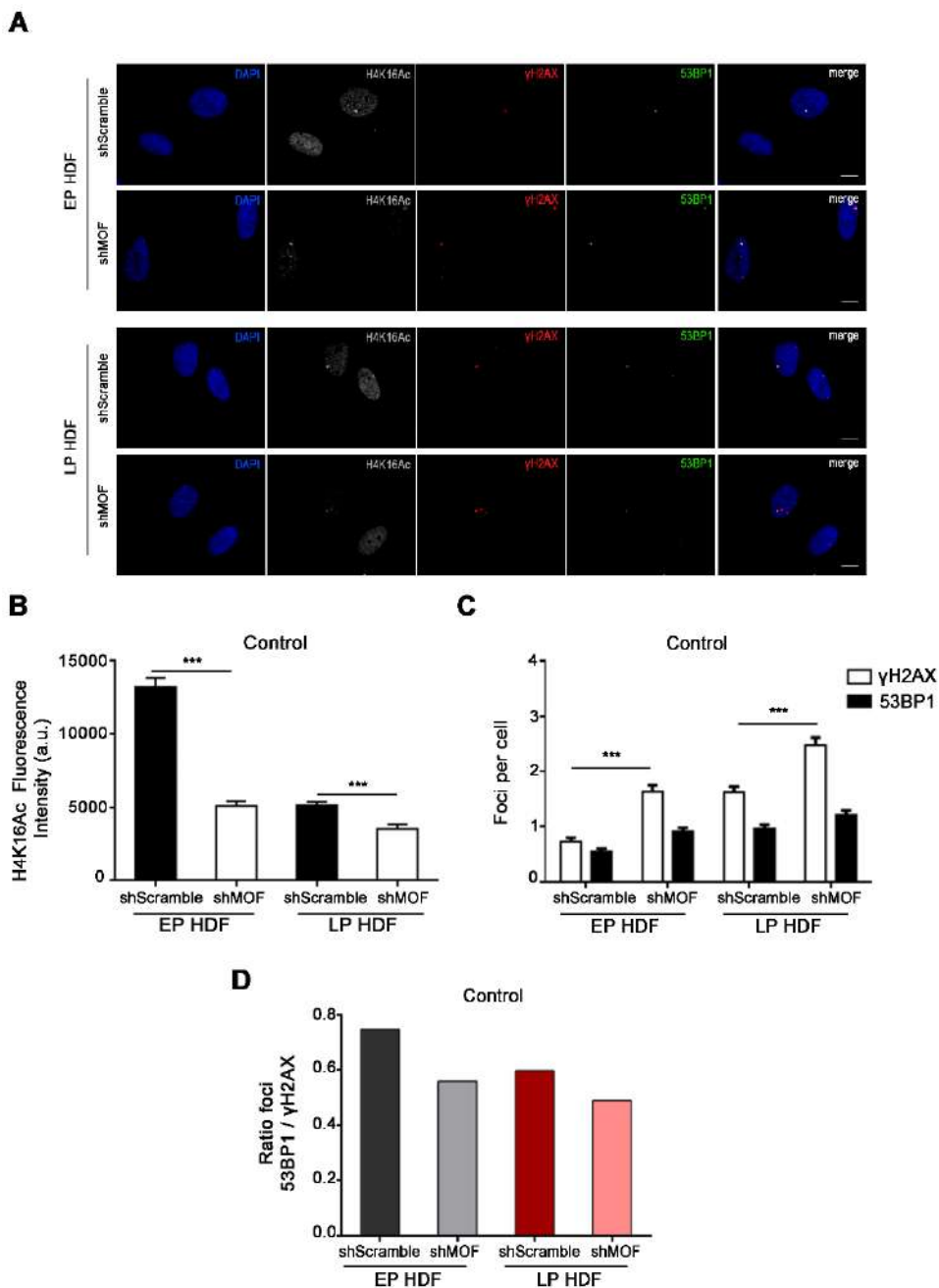


Figure 39. *MOF* depletion results in increased DSB induction in EP and LP HDFs. (A) Triple immunofluorescence staining of H4K16Ac (A532, grey), γ H2AX (A594, red) and 53BP1 (A488, green) in EP and LP HDFs infected with shScramble and shMOF in control conditions. Merged panel shows colocalization of 53BP1 and γ H2AX foci. DAPI (blue) was used to label cell nuclei. Scale bar = 10 μ m. (B) Mean of corrected total cell fluorescence intensity of H4K16Ac in EP and LP HDFs infected with shScramble and shMOF. Error bars indicate SEM and asterisks indicate statistically significant differences (Mann-Whitney test; *** p <0.001). (Continue on the next page)

(C) Mean number of γ H2AX and 53BP1 foci per cell in EP and LP HDFs infected with shScramble and shMOF in control conditions. Error bars indicate SEM and asterisks indicate statistically significant differences (Mann-Whitney test; *** $p < 0.001$). (D) Ratios of 53BP1 and γ H2AX foci colocalization in EP and LP HDFs infected with shScramble and shMOF in control conditions.

In order to further examine the effect of *MOF* depletion on 53BP1 recruitment, we analyzed 53BP1/ γ H2AX colocalization ratio after inducing DSBs with bleocin. Firstly, shMOF infection was confirmed after analyzing H4K16Ac levels by immunofluorescence in control and *MOF*-depleted HDFs (**Figure 40A**). Infected cells with shMOF showed significantly lower levels of H4K16Ac compared to control cells which were infected with shScramble (**Figure 40B**). Following 1 h treatment with bleocin, we evaluated the number of induced γ H2AX foci together with the recruitment of 53BP1 to these γ H2AX foci. After bleocin treatment, the number of induced γ H2AX foci was similarly increased in both control and *MOF*-depleted EP and LP HDFs (**Figure 40C**). This bleocin-associated induction of DSBs masked the *MOF* depletion-related increase of γ H2AX foci that was previously observed in control conditions. Nonetheless, 53BP1 recruitment to bleocin-induced γ H2AX was significantly different in *MOF*-depleted compared to control cells. Those cells with depleted *MOF* showed reduced number of 53BP1 foci in comparison to their control counterparts (**Figure 40C**). This phenomenon occurred in both EP and LP HDFs. Taking these results into account, reduced 53BP1/ γ H2AX colocalization ratios were observed in EP and LP HDFs after *MOF* inhibition. Reduction of 53BP1/ γ H2AX colocalization ratios after *MOF* silencing was more prominent in LP HDFs (**Figure 40D**).

Altogether these findings show that artificial reduction of H4K16Ac levels by *MOF* inhibition leads to a decreased recruitment of 53BP1 to γ H2AX foci. These results reinforce the need of reaching a specific H4K16Ac level to activate a fully operative DDR. Consequently, the accumulation of unrepaired DSBs with age could at least be partly explained by the age-associated reduction of H4K16Ac levels below the optimum level required for an appropriate recruitment of 53BP1.

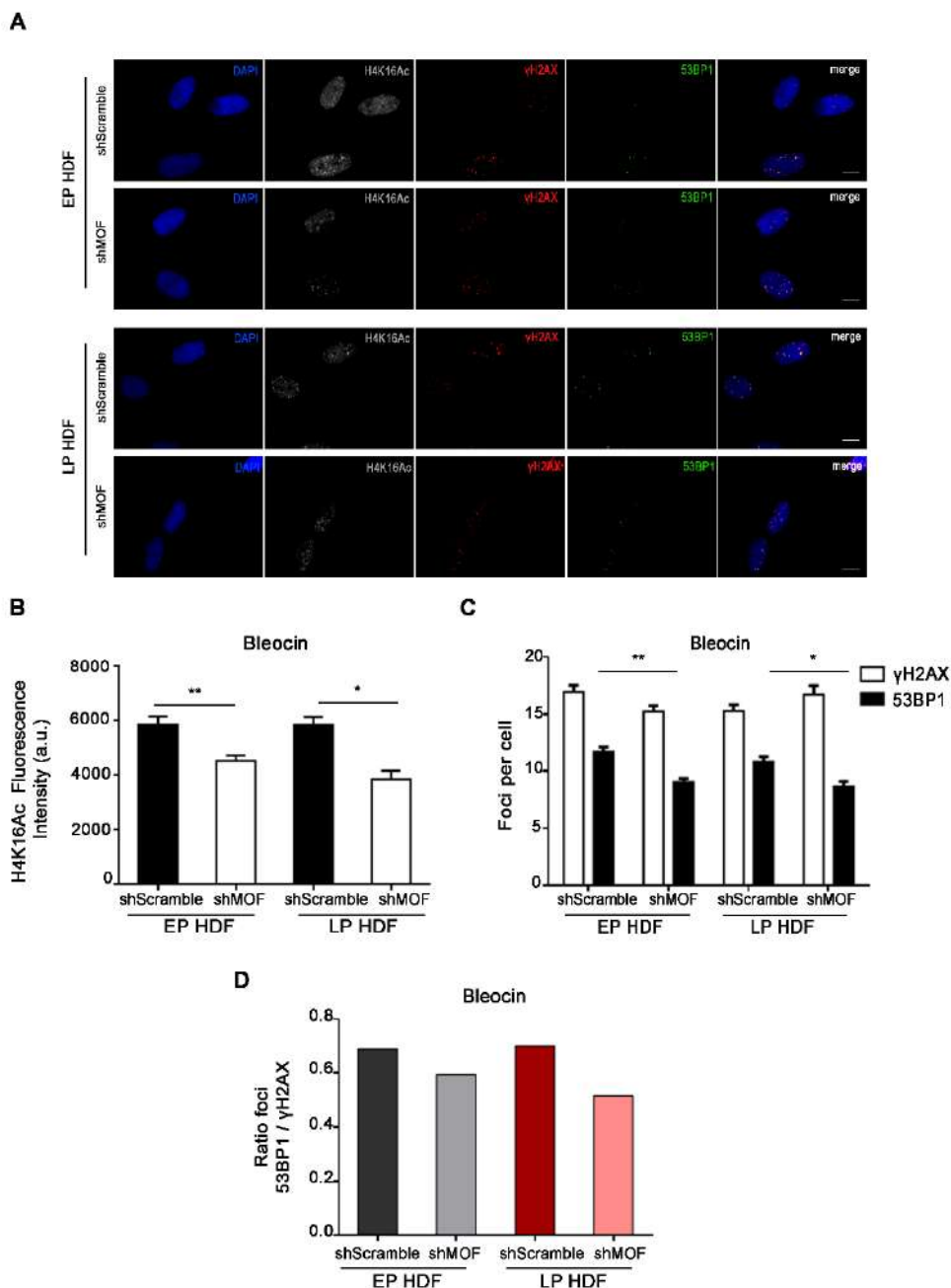


Figure 40. 53BP1 recruitment to induced DSBs is reduced after *MOF* depletion in EP and LP HDFs. (A) Triple immunofluorescence staining of H4K16Ac (A532, grey), γ H2AX (A594, red) and 53BP1 (A488, green) in EP and LP HDFs infected with shScramble and shMOF after bleocin treatment. Merged panel shows colocalization of 53BP1 foci with γ H2AX foci. DAPI (blue) was used to label cell nuclei. Scale bar = 10 μ m. (Continue on the next page)

(B) Mean of corrected total cell fluorescence intensity of H4K16Ac in EP and LP HDFs infected with shScramble and shMOF after bleocin treatment. Error bars indicate SEM and asterisks indicate statistically significant differences (Mann-Whitney test; * $p < 0.05$, ** $p < 0.01$). **(C)** Mean number of γ H2AX and 53BP1 foci per cell in EP and LP HDFs infected with shScramble and shMOF after bleocin treatment. Error bars indicate SEM and asterisks indicate statistically significant differences (Mann-Whitney test; * $p < 0.05$, ** $p < 0.01$). **(D)** Ratios of 53BP1 and γ H2AX foci colocalization in EP and LP HDFs infected with shScramble and shMOF after bleocin treatment.





Discussion

DNA damage has been identified as one of the major drivers of the aging process (López-Otín et al., 2013; Moskalev et al., 2013). Among the distinct DNA lesions, DSBs are difficult to remove and pose a considerable threat because joining of illegitimate ends may occur. Indeed, the accumulation of unrepaired DSBs with age can lead to adverse consequences such as cell death or cancer-causing genome rearrangements (Gorbunova and Seluanov, 2016; White and Vijg, 2016). The relevance of DSB repair to aging is confirmed by the fact that mutations in multiple genes involved in DSB repair lead to a premature aging phenotype (Bohr, 2002). For instance, mice with disruption in NHEJ genes Ku80 (Vogel et al., 1999) and DNA-PKcs (Espejel et al., 2004) have a significantly shortened life span and exhibit early onset of classical aging pathologies. These evidences together support a relationship between defective DSB repair and age.

Since DNA is packed with core histones into higher levels of chromatin structure, the events related to DNA repair should be regulated within the layers of chromatin (Krishnan et al., 2011b). Recent efforts have demonstrated that during DNA repair, histone modifications act in concert to allow the access of the DNA repair machinery to DNA damage sites (Krishnan et al., 2011b). One such histone mark that is critical for the maintenance of chromatin structure and the efficient repair of DSBs is H4K16Ac. Interestingly, the age-associated changes of H4K16Ac (Krishnan et al., 2011a) and its involvement in 53BP1 recruitment to DSB sites (Hsiao and Mizzen, 2013; Tang et al., 2013) insinuate a key role for this histone mark in the regulation of DSB repair during aging. Similarly, preliminary data suggests a possible role of the novel epigenetic mark H3K4ox in DDR through chromatin state regulation (Cebrià-Costa, 2017).

This study describes how the novel epigenetic mark H3K4ox changes in an age-dependent manner and establishes H4K16Ac as a DNA damage responsible mark that is essential for proper DSB repair during aging.

To better understand the implications of this study, the different results obtained are discussed below.

1. Evaluation of cellular aging models

Given the heterogeneity and complexity of the aging phenotype in humans, *in vitro* studies have been extensively used as reliable approach to investigate the mechanisms of aging (Lidzbarsky et al., 2018). The biggest question of *in vitro* studies is whether cell culture adequately reflects *in vivo* conditions and, thus, the translation of results to a whole organism. Cells in culture and those in an intact organism display different metabolic needs and growth conditions. Moreover, cultured cells impair the dynamic cross-talk between cells and the extracellular matrix. To compensate for the main *in vitro* limitation, researchers turn to *in vivo* studies, in which cells from aged animals or humans are used (Lidzbarsky et al., 2018). Nonetheless, significant disadvantages of *in vivo* studies include the expensive costs of animal models, the longer experimental timescales and the fact that *in vivo* models are not always available. Also, depending on the cell type, the obtained cells may require a brief time of culture exposing them to culture-associated stress (Arantes-Rodrigues et al., 2013). Thus, each aging model has its drawbacks and its advantages, and researchers use the most convenient or available models for their work.

In this thesis we have used an OIS model and an *in vitro* aging model of fibroblasts that have accumulated extensive passaging but have not yet reached senescence. Fibroblasts have been widely used as an *in vitro* model of aging since replicative senescence was firstly described in fibroblasts by Hayflick and Moorehead (1961). Also, the use of BJ fibroblasts carrying an inducible *ER:RAS* vector constitutes a widely-extended tool for dissecting the molecular mechanisms regulating senescence (Tarutani et al., 2003; Innes and Gil, 2019).

Because many works regarding age-associated variations in epigenetic factors have been performed in senescent fibroblasts (Narita et al., 2003; Fraga and Esteller, 2007; Sidler et al., 2017), we established an OIS model in order to validate the methods used to measure H4K16Ac variations in our work. We validated the successful induction of RAS-mediated senescence by the identification of some senescence-associated biomarkers like elevated SA- β -gal activity, upregulation of the cell cycle regulator p21, downregulation of the epigenetic mark H3K4me3, typically associated with active transcription (Li et al., 2007), formation of SAHF and persistent DNA damage, identified by the increased frequency of γ H2AX foci. Consequently, these results confirm our inducible model of OIS as an easily exploitable tool for a better understanding of senescent phenotypes that ultimately promote aging.

While *in vitro* senescent cells are almost homogeneous populations, in *in vivo* aged tissues, senescent cells do coexist with young cells and with aged cells that have undergone many passages but have yet to reach senescence. For this reason, serial culture of HDFs was used as a model that partially mimics the cellular and molecular changes associated with aging. The proliferation limit of HDFs and their gradual acquirement of the aging phenotype are commonly associated with the *in vivo* lifespan of the organism (Rubin, 1997; Tigges et al., 2014). Taking into account that HDFs reach their replicative limit after 30 passages in culture (Sedelnikova et al., 2004), an age-related distinction between EP and LP HDFs was established based on the number of culture passages, morphology and replicative rate. EP HDFs, with less than 10 passages in culture, showed the characteristic spindle shape of adherent fibroblasts. On the other hand, LP HDFs, with more than 20 culture passages, displayed increased cell size and vacuoles together with a loss of replicative potential with increasing passage.

Although results obtained from *in vitro* studies should be viewed with caution when translated to a whole organismal aging, we consider OIS and *in vitro*

aging of HDFs as reliable and relatively simple strategies to investigate the conserved pathways involved in aging.

2. H3K4ox is an age-dependent epigenetic mark

Once OIS and *in vitro* aged HDFs were established and validated as cellular models of aging, we were able to study the age-associated behavior of the novel epigenetic mark H3K4ox.

Recent research on the chemical reactions occurring on H3 has revealed that the deamination of H3K4me3 by the oxidases LOXL2 or LOXL1 results in the formation of H3K4ox, an epigenetic histone mark with unknown physiological function (Herranz et al., 2016). Specifically, H3K4ox is enriched in heterochromatic regions, where it favours their characteristic condensed state (Cebrià-Costa et al., 2019). Considering that aging has been largely associated with changes in heterochromatin distribution (Oberdoerffer and Sinclair, 2007), H3K4ox emerges as an interesting histone mark whose pattern and distribution are worth evaluating during aging processes. Moreover, it has been observed that forcing chromatin decondensation by depletion of LOXL2, and consequently lowering H3K4ox levels, leads to increased number of γ H2AX and 53BP1 (Cebrià-Costa et al., 2019), suggesting H3K4ox to participate in the DDR.

Firstly, our results showed a global reduction of H3K4ox during senescence and *in vitro* aging. This reduction was more evident in senescent fibroblasts than in *in vitro* aged HDFs. Accordingly, the expression levels of *LOXL2* and *LOXL1* suffered from a strong decrease in senescent fibroblasts while in *in vitro* aged HDFs only *LOXL1* expression was reduced. The downregulation of only one oxidase during *in vitro* aging may explain the subtler reduction of H3K4ox observed in aged HDFs. Thus, the oxidase responsible for this reduction may vary between age-related processes, remarking their distinct nature.

Since H3K4ox has been connected to structural changes in heterochromatin that lead to a more compacted chromatin and a less efficient DDR, one would expect higher oxidation levels during aging and senescence. Contrary to what predicted, our results showed a global reduction of H3K4ox levels during senescence and *in vitro* aging. This could be explained considering the age-related heterochromatin redistribution model that associates aging with a decrease in global heterochromatin levels and with an increase in heterochromatin formation at specific loci (Oberdoerffer and Sinclair, 2007; Tsurumi and Li, 2012). These alterations to higher-order chromatin structure during senescence result in the formation of specialized domains of heterochromatin, the so-called SAHF (Parry and Narita, 2016). In this regard, we observed that H3K4ox was specifically enriched in SAHF compared to the rest of the nucleus; thus confirming the link of this mark with heterochromatic regions of highly condensed DNA. Because SAHF are thought to contribute to the senescence phenotype by packaging proliferative genes into repressed heterochromatic domains (Zhang et al., 2007; Parry and Narita, 2016), the presence of H3K4ox in SAHF suggests an association of this mark with gene silencing. In fact, SAHF are characterized by the exclusion of euchromatin marks such as H3K4me3 (Narita et al., 2003), which could be explained by the oxidation of the residue.

Interestingly, LOXL2-dependent H3K4me3 oxidation is crucial for the chromatin reorganization during other cellular events such as the transition from epithelial to mesenchymal (EMT) state (Millanes-Romero et al., 2013). It has been demonstrated that upon induction of EMT, LOXL2 is recruited to pericentromeric regions to oxidize H3 which in turns represses the transcription of long non-coding major satellites, leading to chromatin redistribution and acquisition of mesenchymal traits (Casanova et al., 2013; Millanes-Romero et al., 2013). Therefore, although not demonstrated, it is possible that oxidation of H3K4 at SAHF might be repressing the transcription of proliferative genes. Finally, EMT has been related, among other processes, to metastasis and

cancer progression. In this regard, high levels of LOXL2 and the corresponding enrichment of H3K4ox have been observed in different triple negative breast cancer cell lines (Cebrià-Costa et al., 2019), which agrees with the aberrant expression of LOLX2 described in various tumours (Barker et al., 2012; Cano et al., 2012; Ahn et al., 2013).

It is worth mentioning that although H3K4ox is primarily enriched in heterochromatin domains, data obtained thus far suggest that the exact H3K4ox-enriched regions might be cell type-specific. This would explain why the heterochromatin-enriched regions with large fraction of H3K4ox identified in breast cancer cells were not overrepresented in senescent fibroblasts.

Therefore, our findings confirm the relationship between heterochromatin regions and H3K4ox, conferring it a potential role in SAHF assembly and gene silencing during senescence. Moreover, variations of LOXL1, LOXL2 and H3K4ox in OIS and in *in vitro* aging, suggest H3K4me3 oxidation as a promising age-associated epigenetic modification, probably with a more relevant role in OIS than in *in vitro* aging. Finally, the presumed influence of H3K4ox on the DDR points the study of the age-associated role of H3K4ox in DDR regulation as an interesting topic for future research.

3. Loss of H4K16 acetylation in OIS and in *in vitro* aging

Acetylation of H4K16 has been extensively associated with aging. In aging model organisms, decreased H4K16Ac by depletion of the acetyltransferase Sas2 extends the replicative lifespan of normal and senescent yeast strains (Dang et al., 2009; Kozak et al., 2010). However, in the case of mammalian aging, the studies performed so far have reached ambiguous conclusions. While replicative senescent fibroblasts display H4K16Ac enrichment over promoter regions of expressed genes (Rai et al., 2014), global loss of H4K16Ac has been observed in both replicative and oncogene-induced senescence in

human fibroblasts (Contrepolis et al., 2012). Similarly, global H4K16 hypoacetylation has been associated with an early cellular senescence phenotype in a mouse model of premature aging (Krishnan et al., 2011a). Consistently, global deacetylation of H4K16 occurs in the liver, heart and bone marrow of normal old mice (Krishnan et al., 2011a) and an age-dependent decrease of H4K16 acetylation has been also demonstrated in oocytes from aged mice (Manosalva and González, 2009). In line with these findings, our results in human fibroblasts demonstrated a global reduction of H4K16Ac levels in OIS and during *in vitro* aging. Given that H4K16Ac regulation depends on the cell cycle, with high levels of H4K16Ac in S and G2 phase decreasing before cells enter mitosis (Vaquero et al., 2006), it is worth mentioning that analysis of the cell cycle showed homogenous distributions of the cell cycle phases between EP and LP HDFs, being most of the cells in G1 phase. Since no significant differences were observed in the cell cycle distribution between EP and LP HDFs, we discarded that the observed age-associated alterations in H4K16Ac come as consequence of its cell-cycle dependent regulation.

Interestingly, our results showed a relation between H4K16Ac levels and the highly developed SAHF of oncogene-induced senescent fibroblasts. Acetylation of H4K16 is key in the regulation of chromatin compaction and gene expression (Akhtar and Becker, 2000; Shogren-Knaak, 2006): while H4K16 deacetylation is usually related to transcriptional silencing and heterochromatin formation, acetylation of H4K16 is generally associated with transcriptional activation (Vaquero et al., 2007a). Since chromatin rearrangements and SAHF formation are hallmarks of senescence (Zhang et al., 2007; Parry and Narita, 2016), deacetylation of H4K16 has been proposed to contribute to SAHF-associated DNA compaction and to the silencing of proliferation-promoting genes in senescent cells (Contrepolis et al., 2012).

Taken all these results together, it seems clear that deacetylation of H4K16 is a common hallmark of both OIS and *in vitro* aging. However, our findings

suggest that this H4K16Ac reduction is established through different molecular mechanisms in each process. During OIS, we noticed increased deacetylase activity due to higher expression levels of sirtuins, especially of *SIRT1*, while the expression levels of *MOF*, the principal acetyltransferase of H4K16, were unaltered. These results agree with the function of SIRT1 in the formation and maintenance of chromatin. SIRT1-mediated H4K16 deacetylation favors facultative heterochromatin formation (Vaquero et al., 2007b; Bosch-Presegue and Vaquero, 2011), thus it is reasonable to think that increased SIRT1 may also promote SAHF formation or maintenance in cells undergoing OIS. Furthermore, SIRT1 has been found to promote replicative senescence in response to chronic genotoxic stress in mouse fibroblasts (Chua et al., 2005).

In the case of *in vitro* aging and contrary to OIS, sirtuins expression remained unchanged while acetyltransferase activity was reduced due to decreased *MOF* expression. Supporting these results, the knockdown of *MOF* results in decreased H4K16Ac and exacerbation of the premature aging phenotype in mouse fibroblasts (Krishnan et al., 2011a).

In addition to sirtuins and *MOF*, we also checked the expression levels of other enzymes that have been directly associated with H4K16 acetylation regulation. The acetyltransferase TIP60 mainly acetylates lysines 5, 8, and 12 of nucleosomal H4 (Steunou et al., 2014); however, it has also been described to target H4K16 during the DDR (Tang et al., 2013). On the other hand, histone deacetylases HDAC1 and HDAC2, whose specific histone substrates have not been yet elucidated (Seto and Yoshida, 2014), seem to be involved in deacetylation of H4K16 shortly after DSB induction (Miller et al., 2010; Hsiao and Mizzen, 2013; Tang et al., 2013). Consistent with their role in the DDR rather than in aging, no differences were detected in the expression levels of *TIP60*, *HDAC1* and *HDAC2*, in neither cellular model. These results reinforce *MOF* and sirtuins as the major enzymes responsible for H4K16Ac regulation during aging processes.

Overall, our findings together with previous data very likely suggest that the reduction of global H4K16Ac in OIS and in *in vitro* aging depends on the expression levels of *SIRT1* and *MOF* respectively, thus highlighting the distinct nature of OIS and *in vitro* aging.

4. Age-associated role of H4K16 acetylation in 53BP1 recruitment to DSBs

As it was previously shown, H4K16Ac alterations in different aging models might be very likely related to the regulation of chromatin structure. Considering that the proper conformation of chromatin is essential for the recruitment of DNA repair proteins to DSBs, it has been proposed that H4K16Ac creates an open-chromatin environment, favorable to the recognition and repair of DSBs (Krishnan et al., 2011a). Thus, we hypothesized that the age-related alterations of H4K16Ac could lead to a defective DDR during aging.

Remarkably, we observed that following DSB induction with γ -rays, EP HDFs responded by diminishing their H4K16Ac levels immediately after irradiation to later recover their basal levels. The same tendency was observed for *MOF* expression levels confirming its role as the main responsible acetyltransferase for variation of H4K16Ac levels, also after DNA damage induction. The biphasic behavior of H4K16Ac after DSB induction displayed by EP HDFs has also been detected in other DNA repair competent cell types, like laser-microirradiated U2OS cells (Miller et al., 2010) or U2OS cells after extensive culture in the continued presence of bleocin (Hsiao and Mizzen, 2013). On the contrary, LP HDFs, thus, *in vitro* aged cells with presumed defects in the DDR, showed a slight increase in H4K16Ac levels both at short and long post-irradiation times. Again, we observed the same tendency in *MOF* expression levels. These results confirm H4K16Ac as a DNA damage responsive mark and unveil a distinct behavior of H4K16Ac in young and in *in vitro* aged HDFs.

4.1. Age-related alterations in 53BP1 recruitment correlate with changes in H4K16Ac

Several studies have described the important role of H4K16Ac in the balance between NHEJ and HR pathways by regulating the binding of the 53BP1 Tudor domain to H4K20me2 at DSB sites (Hsiao and Mizzen, 2013; Tang et al., 2013). The distinct kinetics of H4K16Ac after DSB induction and the reported alterations in 53BP1 recruitment to DSBs during *in vitro* and *in vivo* cellular aging (Hernández et al., 2013; Anglada, 2018), led us to investigate the relationship between age-related H4K16Ac changes and 53BP1 recruitment during *in vitro* aging.

First, it is important to mention that *in vitro* aging of HDFs was accompanied by an increased number of basal γ H2AX foci. These results are consistent with previous findings reporting an increased frequency of γ H2AX signaling in *in vitro* aged cells (Sedelnikova et al., 2004, 2008; Hernández et al., 2013; Pustovalova et al., 2016). Also cells from aged human donors present an increased frequency of genome reorganizations and γ H2AX foci with increasing age (Sedelnikova et al., 2008; Rube et al., 2011; Titus et al., 2013; Kalfalah et al., 2015; Anglada et al., 2019). The reasons behind this accumulation might be an age-associated repair defect related to the ability of age cells to recruit repair proteins, like 53BP1, to the damage sites.

In this regard, LP HDFs also displayed a decrease in 53BP1 recruitment to DSBs sites compared to EP HDFs. These results are in agreement with previous descriptions of impaired 53BP1 recruitment to γ H2AX foci in *in vitro* and *in vivo* aged human mammary epithelial cells (Hernández et al., 2013; Anglada, 2018), suggesting that impairments in 53BP1 recruitment might function as a sensitive molecular marker of aging in different cell types. Increased basal DSBs and decreased 53BP1 recruitment to these DSBs in LP HDFs were accompanied by significantly lower levels of H4K16Ac than in EP cells. Strikingly, after DSB induction with bleocin or γ -rays, H4K16Ac levels

experienced an immediate reduction in EP HDFs and a rapid increase in LP HDFs. The same tendency was observed regarding 53BP1 recruitment to γ H2AX-labelled DSBs after bleocin treatment. We hypothesize that the colocalization ratio reached a maximum value of 0.7 after bleocin treatment- instead of values near 1 in control conditions- both in EP and LP HDFs due to the continuous presence of bleocin in the cell media, constantly inducing DSBs. It is likely that the most recently induced DSBs have not been yet able to recruit enough DNA repair proteins. In fact, after DSB induction with γ -rays, a punctual and finite or discontinuous source of DNA damage, the colocalization ratio remained stable in EP HDFs and increased in LP HDFs compared to control conditions. Nevertheless, independently from the DSB source, H4K16Ac reached a similar steady value in EP and LP HDFs and 53BP1/ γ H2AX colocalization ratios also converged in all passages. Hence, 53BP1 recruitment to γ H2AX-labelled DSBs improved in LP HDFs after DSB induction and this correlated with an increase of H4K16Ac. Similar to this observation, higher levels of H4K16Ac facilitate 53BP1 recruitment after DSB induction in cellular models of premature aging such as *Zmpste24*^{-/-} cells (Krishnan et al., 2011a). Taken together, these data seem to disclose a correlation between global levels of H4K16Ac and 53BP1 recruitment during *in vitro* aging.

H4K16 acetylation has been recently proposed to limit 53BP1 association with DSBs by reducing its binding affinity towards H4K20me2, which would favor DNA repair by HR (Hsiao and Mizzen, 2013; Tang et al., 2013). Nonetheless, our results show that transient hypoacetylation of H4K16 cannot be the only factor influencing 53BP1 recruitment to DSBs. If that was the case, LP HDFs, which remain mostly in G1 phase and display a constant hypoacetylation state when compared to EP HDFs, would not exhibit 53BP1 recruitment defects as shown in this study and in previous works (Hernández et al., 2013; Anglada, 2018). In a recent work, Tang and coworkers (2013) described H4K16 deacetylation after DNA damage induction as a rapid, transient and DSB-localized event in U2OS cells, which are DNA repair competent cells. To this

extent, we observed an equivalent behavior in EP HDFs, which are also DNA repair competent cells: they reduced their H4K16 acetylation levels after DSB induction. Instead, in *in vitro* aged HDFs, we identified a basal H4K16 hypoacetylation which rapidly raised after DSB induction. Hence, EP and LP HDFs ultimately reach very similar H4K16Ac levels after DSB induction. We propose that this steady state level might be the optimal one for proper 53BP1 recruitment to DSBs.

4.2. A specific level of H4K16Ac is required for a proper 53BP1 recruitment

To gain insight into the relationship between H4K16 acetylation levels and 53BP1 recruitment during *in vitro* aging, we analyzed the effects of hyper- and hypoacetylation of H4K16 on the recruitment of 53BP1. Since following DSB induction, aged HDFs displayed an increase in both 53BP1/γH2AX colocalization and H4K16Ac levels, we reasoned that hyperacetylation might improve 53BP1 recruitment to bleocin-induced DSBs during *in vitro* aging. For this purpose, we used trichostatin A (Kim and Bae, 2011) and nicotinamide (Avalos et al., 2005) to inhibit HDAC1 and HDAC2 (class I HDAC) and sirtuins, all of them involved in H4K16 deacetylation (Vaquero et al., 2007a; Miller et al., 2010).

Contrary to what might be expected, hyperacetylation using both nicotinamide and trichostatin A failed to ameliorate the recruitment of 53BP1 before and after DSB induction in neither young nor aged HDFs. Instead, a global reduction of H4K16Ac by *MOF* silencing did reduce 53BP1 recruitment to DSBs. Depletion of *MOF* was more efficient in LP than in EP HDFs. However, it is worth mentioning that the initial expression of *MOF* and the levels of H4K16Ac were lower in LP HDFs than in EP HDFs which reinforces the age-associated reduction of *MOF* expression and H4K16Ac levels that we observed in other experiments. Silencing of *MOF* instead of *TIP60* was chosen since *MOF* has been described to have major role in H4K16 acetylation (Smith et al., 2005;

Taipale et al., 2005) and, in agreement with this, we did not observe significant changes in *TIP60* expression during *in vitro* aging.

MOF silencing resulted in an overall increase of basal DSBs with limited 53BP1 recruitment, being this defect more pronounced after DSB induction. This might be explained if we consider that 53BP1 should be recruited not only to the bleocin-induced DSBs but also to the *MOF* depletion-related DSBs. Accordingly, other studies have described that *MOF* depletion down-regulates H4K16 acetylation and impairs the recruitment of MDC1 as well as other downstream proteins, such as 53BP1 and BRCA1 to damaged sites (Li et al., 2010; Sharma et al., 2010); however, it does not affect their gene expression neither the total amount of DDR proteins. These observations imply that *MOF*-dependent H4K16 acetylation is able to alter the DDR performance through modifications at the chromatin level (Li et al., 2010; Sharma et al., 2010). Therefore, given the relevance of H4K16Ac, its reduction by *MOF* depletion could explain the decrease in 53BP1 foci formation. Consistently with this observation, *MOF* overexpression in a mouse model of premature aging leads to enhanced global H4K16 acetylation levels and improved 53BP1 recruitment to DSB sites (Krishnan et al., 2011a). These evidences and the fact that hyperacetylation with trichostatin A or nicotinamide did not improve recruitment of 53BP1, suggest *MOF*, through H4K16 acetylation, to play a prominent role in the recruitment of 53BP1 to DSB sites. Nevertheless, further experiments, such as *MOF* overexpression in aged cells, should be performed to confirm this theory.

In summary, with the data reported in this study we propose a model of H4K16Ac regulation with age and in response to DNA damage that contributes to the proper recruitment of DNA repair effector 53BP1 to the DSB sites. According to this model (**Figure 41**) following DSB induction, H4K16Ac reaches a specific and stable level for the appropriate recruitment of 53BP1 to DSB sites. In young cells, this level is rapidly achieved by slightly lowering their basal H4K16Ac levels. Nevertheless, aged cells display lower levels of basal

H4K16Ac that might impede them to reach the optimum H4K16Ac level for proper 53BP1 recruitment. Consequently, the present study suggests that a linear relationship between epigenetic status, DNA repair and aging might be too simplistic to assume. Indeed, these evidences constitute the basis for a future research study in which the role of H4K16Ac as a key mediator between DNA repair and chromatin structure could shed some light on the molecular mechanisms governing organismal aging.

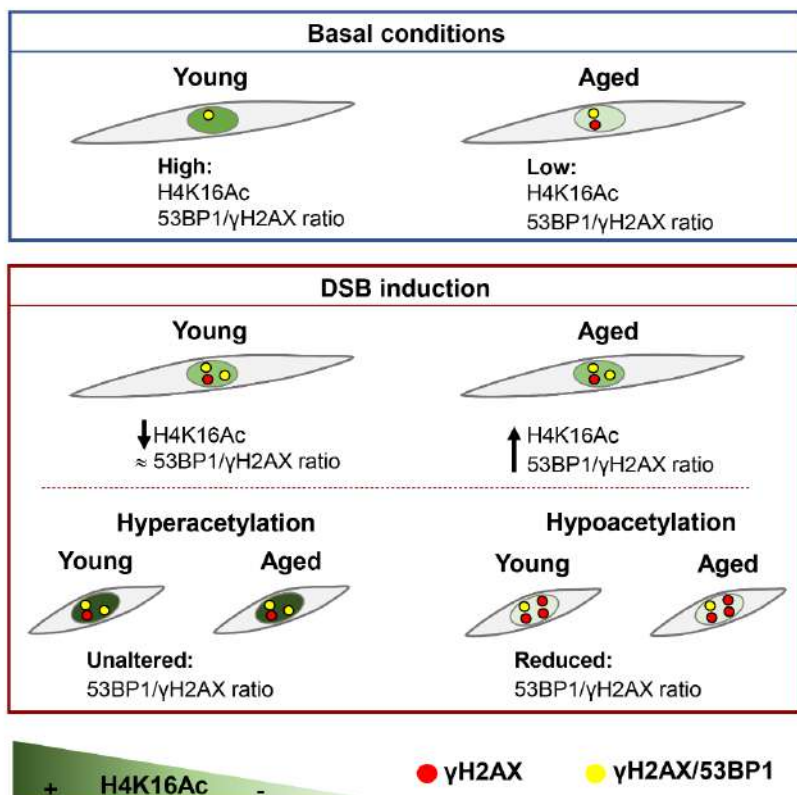


Figure 41. Age-associated dynamics of H4K16Ac after DSB induction. In basal conditions, H4K16Ac levels and 53BP1/γH2AX colocalization ratio are higher in young than in aged HDFs. After DSB induction, the H4K16Ac levels slightly decrease in young cells while they increase in aged cells. Regarding 53BP1/γH2AX colocalization ratio, it barely changes after DSB induction in young HDFs; however, it increases in aged HDFs in comparison to control conditions. As a result, H4K16Ac levels and 53BP1/γH2AX colocalization ratios converge in all passages. Independently from the culture passage, hyperacetylation prior to DSB induction does not improve 53BP1/γH2AX colocalization ratio. In contrast, H4K16 hypoacetylation impairs 53BP1 recruitment to γH2AX-labelled DSBs, reducing the 53BP1/γH2AX colocalization ratio in young and aged HDFs. Consequently, after DSB induction, H4K16Ac reaches a specific level which is required for an appropriate recruitment of 53BP1 to DSB sites.



Conclusions

1. H3K4ox levels decrease in oncogene-induced senescent cells and in *in vitro* aged cells most probably due to a reduction of the oxidizers LOXL1 and LOX2, which suggests that H3K4ox is an age-associated histone mark.
2. In oncogene-induced senescent cells, H3K4ox is locally enriched in SAHF where it may have a potential role in their assembly during senescence.
3. H4K16 acetylation decreases in oncogene-induced senescent cells and in *in vitro* aged cells, although the mechanisms underlying this age-associated reduction vary in both processes. While in OIS, sirtuins expression is enhanced, in *in vitro* aging, the expression of the acetyltransferase MOF is reduced.
4. In basal conditions and compared to young fibroblasts, *in vitro* aged fibroblasts display a decreased recruitment of 53BP1 to DSBs that correlates with a reduction of H4K16 acetylation levels.
5. Following DSB induction, H4K16 acetylation slightly decreases in young fibroblasts while it increases in *in vitro* aged cells, smoothing the differences existing among passages in control conditions. A similar tendency is observed regarding 53BP1 recruitment to DSBs. Consequently, H4K16Ac and 53BP1 recruitment reach similar levels in young and in *in vitro* aged fibroblasts.
6. Hyperacetylation of H4K16 does not improve the recruitment of 53BP1 to DSBs while MOF-mediated H4K16 hypoacetylation reduces it. Therefore, after DNA damage induction, H4K16Ac reaches a specific and stable level required for an appropriate recruitment of 53BP1 to DSB sites.



References

- Ahn, S.G. et al. (2013). LOXL2 expression is associated with invasiveness and negatively influences survival in breast cancer patients. *Breast Cancer Res. Treat.* *141*, 89–99.
- Ahnesorg, P. et al. (2006). XLF Interacts with the XRCC4-DNA Ligase IV Complex to Promote DNA Nonhomologous End-Joining. *Cell* *124*, 301–313.
- Akhtar, A., and Becker, P.B. (2000). Activation of transcription through histone H4 acetylation by MOF, an acetyltransferase essential for dosage compensation in *Drosophila*. *Mol. Cell* *5*, 367–375.
- Anglada, T. (2018). Contribució de BRCA1 i 53BP1 a la reparació dels trencaments del DNA: efecte de l'edat. Universitat Autònoma de Barcelona.
- Anglada, T. et al. (2019). Delayed γ H2AX foci disappearance in mammary epithelial cells from aged women reveals an age-associated DNA repair defect. *Aging (Albany, NY)*. *11*, 1510–1523.
- Aparicio, T. et al. (2014). DNA double-strand break repair pathway choice and cancer. *DNA Repair (Amst)*. *19*, 169–175.
- Aplan, P.D. (2006). Causes of oncogenic chromosomal translocation. *Trends Genet.* *22*, 46.
- Arantes-Rodrigues, R. et al. (2013). In vitro and in vivo experimental models as tools to investigate the efficacy of antineoplastic drugs on urinary bladder cancer. *Anticancer Res.* *33*, 1273–1296.
- Avalos, J.L. et al. (2005). Mechanism of Sirtuin Inhibition by Nicotinamide: Altering the NAD⁺ Cosubstrate Specificity of a Sir2 Enzyme. *Mol. Cell* *17*, 855–868.
- Bakkenist, C.J., and Kastan, M.B. (2003). DNA damage activates ATM through intermolecular autophosphorylation and dimer dissociation. *Nature* *421*, 499–506.

Baldehyron, C. et al. (2011). HP1alpha recruitment to DNA damage by p150CAF-1 promotes homologous recombination repair. *J. Cell Biol.* 193, 81–95.

Bannister, A.J., and Kouzarides, T. (2011). Regulation of chromatin by histone modifications. *Cell Res.* 21, 381–395.

Barker, H.E. et al. (2012). The rationale for targeting the LOX family in cancer. *Nat. Rev. Cancer* 12, 540–552.

Baumann, P. et al. (1996). Human Rad51 protein promotes ATP-dependent homologous pairing and strand transfer reactions in vitro. *Cell* 87, 757–766.

Becker, J.S. et al. (2016). H3K9me3-Dependent Heterochromatin: Barrier to Cell Fate Changes. *Trends Genet.* 32, 29–41.

Bednar, J. et al. (1998). Nucleosomes, linker DNA, and linker histone form a unique structural motif that directs the higher-order folding and compaction of chromatin. *Proc. Natl. Acad. Sci. U. S. A.* 95, 14173–14178.

Bekker-Jensen, S., and Mailand, N. (2010). Assembly and function of DNA double-strand break repair foci in mammalian cells. *DNA Repair (Amst).* 9, 1219–1228.

Ben-Avraham, D. et al. (2012). Epigenetic genome-wide association methylation in aging and longevity. *Epigenomics* 4, 503–509.

Ben-Porath, I., and Weinberg, R.A. (2005). The signals and pathways activating cellular senescence. *Int. J. Biochem. Cell Biol.* 37, 961–976.

Berkovich, E. et al. (2007). Roles of ATM and NBS1 in chromatin structure modulation and DNA double-strand break repair. *Nat. Cell Biol.* 9, 683–690.

Best, B.P. (2009). Nuclear DNA Damage as a Direct Cause of Aging. *Rejuvenation Res.* 12, 199–208.

Bhargava, R. et al. (2018). C-NHEJ without indels is robust and requires

- synergistic function of distinct XLF domains. *Nat. Commun.* 9, 2484.
- Blackford, A.N., and Jackson, S.P. (2017). ATM, ATR, and DNA-PK: The Trinity at the Heart of the DNA Damage Response. *Mol. Cell* 66, 801–817.
- Bohr, V.A. (2002). Human premature aging syndromes and genomic instability. *Mech. Ageing Dev.* 123, 987–993.
- Boraldi, F. et al. (2010). Comparison of ex vivo and in vitro human fibroblast ageing models. *Mech. Ageing Dev.* 131, 625–635.
- Bosch-Presegue, L., and Vaquero, A. (2011). The Dual Role of Sirtuins in Cancer. *Genes Cancer* 2, 648–662.
- Bothmer, A. et al. (2011). Regulation of DNA End Joining, Resection, and Immunoglobulin Class Switch Recombination by 53BP1. *Mol. Cell* 42, 319–329.
- Botuyan, M.V. et al. (2006). Structural Basis for the Methylation State-Specific Recognition of Histone H4-K20 by 53BP1 and Crb2 in DNA Repair. *Cell* 127, 1361–1373.
- Brandsma, I., and Gent, D.C. (2012). Pathway choice in DNA double strand break repair: observations of a balancing act. *Genome Integr.* 3, 9.
- Bree, R.T. et al. (2004). The switch from survival responses to apoptosis after chromosomal breaks. *DNA Repair (Amst)*. 3, 989–995.
- Brunet, A., and Berger, S.L. (2014). Epigenetics of Aging and Aging-related Disease. *Journals Gerontol. Ser. A Biol. Sci. Med. Sci.* 69, S17–S20.
- Burma, S. et al. (2001). ATM Phosphorylates Histone H2AX in Response to DNA Double-strand Breaks. *J. Biol. Chem.* 276, 42462–42467.
- Bustin, S.A. et al. (2009). The MIQE guidelines: minimum information for publication of quantitative real-time PCR experiments. *Clin. Chem.* 55, 611–622.

Campisi, J. (2013). Aging, Cellular Senescence, and Cancer. *Annu. Rev. Physiol.* 75, 685–705.

Campisi, J., and d'Adda di Fagagna, F. (2007). Cellular senescence: when bad things happen to good cells. *Nat. Rev. Mol. Cell Biol.* 8, 729–740.

Cano, A. et al. (2012). LOXL2 in epithelial cell plasticity and tumor progression. *Futur. Oncol.* 8, 1095–1108.

Casanova, M. et al. (2013). Heterochromatin Reorganization during Early Mouse Development Requires a Single-Stranded Noncoding Transcript. *Cell Rep.* 4, 1156–1167.

Cebrià-Costa, J.P. et al. (2019). LOXL2-mediated H3K4 oxidation reduces chromatin accessibility in triple-negative breast cancer cells. *Oncogene* 1–43.

Chang, H.H.Y. et al. (2017). Non-homologous DNA end joining and alternative pathways to double-strand break repair. *Nat. Rev. Mol. Cell Biol.* 18, 495–506.

Chapman, J.R. et al. (2012). Playing the End Game: DNA Double-Strand Break Repair Pathway Choice. *Mol. Cell* 47, 497–510.

Chapman, J.R. et al. (2013). RIF1 is essential for 53BP1-dependent nonhomologous end joining and suppression of DNA double-strand break resection. *Mol. Cell* 49, 858–871.

Chen, L. et al. (2008). Cell Cycle-dependent Complex Formation of BRCA1·CtIP·MRN Is Important for DNA Double-strand Break Repair. *J. Biol. Chem.* 283, 7713–7720.

Childs, B.G. et al. (2015). Cellular senescence in aging and age-related disease: from mechanisms to therapy. *Nat. Med.* 21, 1424.

Christensen, B.C. et al. (2009). Aging and Environmental Exposures Alter Tissue-Specific DNA Methylation Dependent upon CpG Island Context. *PLoS Genet.* 5, e1000602.

- Chua, K.F. et al. (2005). Mammalian SIRT1 limits replicative life span in response to chronic genotoxic stress. *Cell Metab.* 2, 67–76.
- Contrepois, K. et al. (2012). Deacetylation of H4-K16Ac and heterochromatin assembly in senescence. *Epigenetics Chromatin* 5, 15.
- Craxton, A. et al. (2015). XLS (c9orf142) is a new component of mammalian DNA double-stranded break repair. *Cell Death Differ.* 22, 890–897.
- d’Adda di Fagagna, F. (2008). Living on a break: cellular senescence as a DNA-damage response. *Nat. Rev. Cancer* 8, 512–522.
- Dang, W. et al. (2009). Histone H4 lysine 16 acetylation regulates cellular lifespan. *Nature* 459, 802–807.
- Debacq-Chainiaux, F. et al. (2009). Protocols to detect senescence-associated beta-galactosidase (SA- β gal) activity, a biomarker of senescent cells in culture and in vivo. *Nat. Protoc.* 4, 1798–1806.
- DeFazio, L.G. et al. (2002). Synapsis of DNA ends by DNA-dependent protein kinase. *EMBO J.* 21, 3192–3200.
- Dekker, P. et al. (2009). Stress-induced responses of human skin fibroblasts in vitro reflect human longevity. *Aging Cell* 8, 595–603.
- DiLoreto, R., and Murphy, C.T. (2015). The cell biology of aging. *Mol. Biol. Cell* 26, 4524–4531.
- Downs, J.A., and Jackson, S.P. (2004). A means to a DNA end: the many roles of Ku. *Nat. Rev. Mol. Cell Biol.* 5, 367–378.
- Eltsov, M. et al. (2008). Analysis of cryo-electron microscopy images does not support the existence of 30-nm chromatin fibers in mitotic chromosomes in situ. *Proc. Natl. Acad. Sci.* 105, 19732–19737.
- Escribano-Díaz, C. et al. (2013). A Cell Cycle-Dependent Regulatory Circuit Composed of 53BP1-RIF1 and BRCA1-CtIP Controls DNA Repair Pathway

Choice. *Mol. Cell* 49, 872–883.

Espejel, S. et al. (2004). Shorter telomeres, accelerated ageing and increased lymphoma in DNA-PKcs-deficient mice. *EMBO Rep.* 5, 503–509.

Feng, L. et al. (2013). RIF1 Counteracts BRCA1-mediated End Resection during DNA Repair. *J. Biol. Chem.* 288, 11135–11143.

Feng, L. et al. (2015). Cell cycle-dependent inhibition of 53BP1 signaling by BRCA1. *Cell Discov.* 1, 15019.

Fradet-Turcotte, A. et al. (2013). 53BP1 is a reader of the DNA-damage-induced H2A Lys 15 ubiquitin mark. *Nature* 499, 50–54.

Fraga, M.F., and Esteller, M. (2007). Epigenetics and aging: the targets and the marks. *Trends Genet.* 23, 413–418.

Freitas, A.A., and de Magalhães, J.P. (2011). A review and appraisal of the DNA damage theory of ageing. *Mutat. Res. Mutat. Res.* 728, 12–22.

Funayama, R., and Ishikawa, F. (2007). Cellular senescence and chromatin structure. *Chromosoma* 116, 431–440.

Fyodorov, D. V. et al. (2017). Emerging roles of linker histones in regulating chromatin structure and function. *Nat. Rev. Mol. Cell Biol.* 19, 192–206.

Garm, C. et al. (2013). Age and gender effects on DNA strand break repair in peripheral blood mononuclear cells. *Aging Cell* 12, 58–66.

Gavet, O., and Pines, J. (2010). Progressive Activation of CyclinB1-Cdk1 Coordinates Entry to Mitosis. *Dev. Cell* 18, 533–543.

Gilbert, N. et al. (2004). Chromatin Architecture of the Human Genome. *Cell* 118, 555–566.

Goodarzi, A.A., and Jeggo, P.A. (2012). The Heterochromatic Barrier to DNA Double Strand Break Repair: How to Get the Entry Visa. *Int. J. Mol. Sci.* 13, 11844–11860.

- Gorbunova, V., and Seluanov, A. (2016). DNA double strand break repair, aging and the chromatin connection. *Mutat. Res. Mol. Mech. Mutagen.* 788, 2–6.
- Gorisch, S.M. et al. (2005). Histone acetylation increases chromatin accessibility. *J. Cell Sci.* 118, 5825–5834.
- Grawunder, U. et al. (1998). DNA ligase IV binds to XRCC4 via a motif located between rather than within its BRCT domains. *Curr. Biol.* 8, 873–876.
- Gregg, S.Q. et al. (2012). A mouse model of accelerated liver aging caused by a defect in DNA repair. *Hepatology* 55, 609–621.
- Grundy, G.J. et al. (2016). The Ku-binding motif is a conserved module for recruitment and stimulation of non-homologous end-joining proteins. *Nat. Commun.* 7, 11242.
- Gupta, A. et al. (2005). Involvement of Human MOF in ATM Function. *Mol. Cell. Biol.* 25, 5292–5305.
- Harper, J.W., and Elledge, S.J. (2007). The DNA Damage Response: Ten Years After. *Mol. Cell* 28, 739–745.
- Hayflick, L., and Moorhead, P.S. (1961). The serial cultivation of human diploid cell strains. *Exp. Cell Res.* 25, 585–621.
- Helleday, T. et al. (2007). DNA double-strand break repair: From mechanistic understanding to cancer treatment. *DNA Repair (Amst).* 6, 923–935.
- Her, J. et al. (2016). Factors forming the BRCA1-A complex orchestrate BRCA1 recruitment to the sites of DNA damage. *Acta Biochim. Biophys. Sin. (Shanghai).* 48, 658–664.
- Her, J., and Bunting, S.F. (2018). How cells ensure correct repair of DNA double-strand breaks. *J. Biol. Chem.* 293, 10502–10511.
- Hernandez-Segura, A. et al. (2017). Unmasking Transcriptional Heterogeneity

in Senescent Cells. *Curr. Biol.* 27, 2652.

Hernández, L. et al. (2013). Increased mammogram-induced DNA damage in mammary epithelial cells aged in vitro. *PLoS One* 8, e63052.

Herranz, N. et al. (2016). Lysyl oxidase-like 2 (LOXL2) oxidizes trimethylated lysine 4 in histone H3. *FEBS J.* 283, 4263–4273.

Hoeijmakers, J.H.J. (2001). Genome maintenance mechanisms for preventing cancer. *Nature* 411, 366–374.

Hoeijmakers, J.H.J. (2009). DNA Damage, Aging, and Cancer. *N. Engl. J. Med.* 361, 1475–1485.

Hsiao, K.Y., and Mizzen, C.A. (2013). Histone H4 deacetylation facilitates 53BP1 DNA damage signaling and double-strand break repair. *J. Mol. Cell Biol.* 5, 157–165.

Huertas, P., and Jackson, S.P. (2009). Human CtIP Mediates Cell Cycle Control of DNA End Resection and Double Strand Break Repair. *J. Biol. Chem.* 284, 9558–9565.

Hustedt, N., and Durocher, D. (2017). The control of DNA repair by the cell cycle. *Nat. Cell Biol.* 19, 1–9.

Innes, A.J., and Gil, J. (2019). IMR90 ER:RAS: A cell model of oncogene-induced senescence. In: *Methods in Molecular Biology*, 83–92.

Itahana, K. et al. (2013). Colorimetric detection of senescence-associated β galactosidase. *Methods Mol. Biol.* 965, 143–156.

Iturbide, A. et al. (2015). A new role for LOX and LOXL2 proteins in transcription regulation. *FEBS J.* 282, 1768–1773.

Jackson, S.P., and Bartek, J. (2009). The DNA-damage response in human biology and disease. *Nature* 461, 1071–1078.

Jenuwein, T., and Allis, C.D. (2001). Translating the Histone Code. *Science*

(80-). 293, 1074–1080.

Jette, N., and Lees-Miller, S.P. (2015). The DNA-dependent protein kinase: A multifunctional protein kinase with roles in DNA double strand break repair and mitosis. *Prog. Biophys. Mol. Biol.* 117, 194–205.

Ju, Y. et al. (2006). Decreased expression of DNA repair proteins Ku70 and Mre11 is associated with aging and may contribute to the cellular senescence. *Exp. Mol. Med.* 38, 686–693.

Jungmichel, S., and Stucki, M. (2010). MDC1: The art of keeping things in focus. *Chromosoma* 119, 337–349.

Kalfalah, F. et al. (2015). Structural chromosome abnormalities, increased DNA strand breaks and DNA strand break repair deficiency in dermal fibroblasts from old female human donors. *Aging (Albany, NY)*. 7, 110–122.

Karagiannis, T.C. et al. (2007). Disparity of histone deacetylase inhibition on repair of radiation-induced DNA damage on euchromatin and constitutive heterochromatin compartments. *Oncogene* 26, 3963–3971.

Kim, H., and Bae, S. (2011). Histone deacetylase inhibitors: molecular mechanisms of action and clinical trials as anti-cancer drugs. *Am. J. Transl. Res.* 3, 166–179.

Kim, J.-A. et al. (2007). Heterochromatin is refractory to γ -H2AX modification in yeast and mammals. *J. Cell Biol.* 178, 209–218.

Kornberg, R.D., and Lorch, Y. (1999). Twenty-Five Years of the Nucleosome, Fundamental Particle of the Eukaryote Chromosome. *Cell* 98, 285–294.

Kouzarides, T. (2007). Chromatin Modifications and Their Function. *Cell* 128, 693–705.

Kozak, M.L. et al. (2010). Inactivation of the Sas2 histone acetyltransferase delays senescence driven by telomere dysfunction. *EMBO J.* 29, 158–170.

Krishnan, V. et al. (2011a). Histone H4 lysine 16 hypoacetylation is associated with defective DNA repair and premature senescence in Zmpste24-deficient mice. *Proc. Natl. Acad. Sci. U. S. A.* 108, 12325–12330.

Krishnan, V. et al. (2011b). “Relax and Repair” to restrain aging. *Aging (Albany, NY)*. 3, 943–954.

Kruhlak, M.J. et al. (2006). Changes in chromatin structure and mobility in living cells at sites of DNA double-strand breaks. *J. Cell Biol.* 172, 823–834.

Kuilman, T. et al. (2010). The essence of senescence. *Genes Dev.* 24, 2463–2479.

Kumaraswamy, E., and Shiekhhattar, R. (2007). Activation of BRCA1/BRCA2-Associated Helicase BACH1 Is Required for Timely Progression through S Phase. *Mol. Cell. Biol.* 27, 6733–6741.

Kuo, M., and Allis, C.D. (1999). In Vivo Cross-Linking and Immunoprecipitation for Studying Dynamic Protein:DNA Associations in a Chromatin Environment. *Methods* 19, 425–433.

Lavin, M.F. (2007). ATM and the Mre11 complex combine to recognize and signal DNA double-strand breaks. *Oncogene* 26, 7749–7758.

Lawrence, M. et al. (2016). Lateral Thinking: How Histone Modifications Regulate Gene Expression. *Trends Genet.* 32, 42–56.

Lempiäinen, H., and Halazonetis, T.D. (2009). Emerging common themes in regulation of PIKKs and PI3Ks. *EMBO J.* 28, 3067–3073.

Li, B. et al. (2007). The Role of Chromatin during Transcription. *Cell* 128, 707–719.

Li, M., and Rossi, J.J. (2008). Lentiviral Vector Delivery of siRNA and shRNA Encoding Genes into Cultured and Primary Hematopoietic Cells. In: *Methods in Molecular Biology (Clifton, N.J.)*, 287–300.

- Li, X. et al. (2009). PCNA is required for initiation of recombination-associated DNA synthesis by DNA polymerase delta. *Mol. Cell* 36, 704–713.
- Li, X. et al. (2010). MOF and H4 K16 Acetylation Play Important Roles in DNA Damage Repair by Modulating Recruitment of DNA Damage Repair Protein Mdc1. *Mol. Cell. Biol.* 30, 5335–5347.
- Li, Z. et al. (2016). Impaired DNA double-strand break repair contributes to the age-associated rise of genomic instability in humans. *Cell Death Differ.* 23, 1765–1777.
- Lidzbarsky, G. et al. (2018). Genomic Instabilities, Cellular Senescence, and Aging: In Vitro, In Vivo and Aging-Like Human Syndromes. *Front. Med.* 5, 104.
- López-Otín, C. et al. (2013). The Hallmarks of Aging. *Cell* 153, 1194–1217.
- Lou, Z. et al. (2006). MDC1 Maintains Genomic Stability by Participating in the Amplification of ATM-Dependent DNA Damage Signals. *Mol. Cell* 21, 187–200.
- Lovejoy, C.A., and Cortez, D. (2009). Common mechanisms of PIKK regulation. *DNA Repair (Amst)*. 8, 1004–1008.
- Lu, J. et al. (2011). Protein acetylation and aging. *Aging (Albany NY)* 3, 911.
- Luger, K. et al. (1997). Crystal structure of the nucleosome core particle at 2.8 Å resolution. *Nature* 389, 251–260.
- Luijsterburg, M.S., and van Attikum, H. (2011). Chromatin and the DNA damage response: the cancer connection. *Mol. Oncol.* 5, 349–367.
- Lujambio, A. (2016). To clear, or not to clear (senescent cells)? That is the question. *BioEssays* 38, S56–S64.
- Lukas, C. et al. (2004). Mdc1 couples DNA double-strand break recognition by Nbs1 with its H2AX-dependent chromatin retention. *EMBO J.* 23, 2674–2683.
- Ma, Y. et al. (2002). Hairpin opening and overhang processing by an Artemis/DNA-dependent protein kinase complex in nonhomologous end joining

and V(D)J recombination. *Cell* 108, 781–794.

Maegawa, S. et al. (2010). Widespread and tissue specific age-related DNA methylation changes in mice. *Genome Res.* 20, 332–340.

Maeshima, K. et al. (2010). Chromatin structure: does the 30-nm fibre exist in vivo? *Curr. Opin. Cell Biol.* 22, 291–297.

Mahaney, B.L. et al. (2009). Repair of ionizing radiation-induced DNA double-strand breaks by non-homologous end-joining. *Biochem. J.* 417, 639–650.

Mailand, N. et al. (2007). RNF8 Ubiquitylates Histones at DNA Double-Strand Breaks and Promotes Assembly of Repair Proteins. *Cell* 131, 887–900.

Mainzer, C. et al. (2018). In vitro epidermis model mimicking IGF-1-specific age-related decline. *Exp. Dermatol.* 27, 537–543.

Mäkiniemi, M. et al. (2001). BRCT Domain-containing Protein TopBP1 Functions in DNA Replication and Damage Response. *J. Biol. Chem.* 276, 30399–30406.

Maloisel, L. et al. (2008). DNA Polymerase δ Is Preferentially Recruited during Homologous Recombination To Promote Heteroduplex DNA Extension. *Mol. Cell. Biol.* 28, 1373–1382.

Mandavilli, B.S., and Rao, K.S. (1996). Accumulation of DNA damage in aging neurons occurs through a mechanism other than apoptosis. *J. Neurochem.* 67, 1559–1565.

Manjunath, N. et al. (2009). Lentiviral delivery of short hairpin RNAs. *Adv. Drug Deliv. Rev.* 61, 732–745.

Manosalva, I., and González, A. (2009). Aging Alters Histone H4 Acetylation and CDC2A in Mouse Germinal Vesicle Stage Oocytes. *Biol. Reprod.* 81, 1164–1171.

Mao, Z. et al. (2012). Sirtuin 6 (SIRT6) rescues the decline of homologous

recombination repair during replicative senescence. *Proc. Natl. Acad. Sci. U. S. A.* *109*, 11800–11805.

Mattioli, F. et al. (2012). RNF168 Ubiquitinates K13-15 on H2A/H2AX to Drive DNA Damage Signaling. *Cell* *150*, 1182–1195.

Mazin, A. V. et al. (2010). Rad54, the motor of homologous recombination. *DNA Repair (Amst)*. *9*, 286–302.

Michan, S., and Sinclair, D. (2007). Sirtuins in mammals: insights into their biological function. *Biochem. J.* *404*, 1–13.

Millanes-Romero, A. et al. (2013). Regulation of Heterochromatin Transcription by Snail1/LOXL2 during Epithelial-to-Mesenchymal Transition. *Mol. Cell* *52*, 746–757.

Miller, K.M. et al. (2010). Human HDAC1 and HDAC2 function in the DNA-damage response to promote DNA nonhomologous end-joining. *Nat. Struct. Mol. Biol.* *17*, 1144–1151.

Misteli, T. (2007). Beyond the Sequence: Cellular Organization of Genome Function. *Cell* *128*, 787–800.

Misteli, T., and Soutoglou, E. (2009). The emerging role of nuclear architecture in DNA repair and genome maintenance. *Nat. Rev. Mol. Cell Biol.* *10*, 243–254.

Mitchell, S.J. et al. (2015). Animal Models of Aging Research: Implications for Human Aging and Age-Related Diseases. *Annu. Rev. Anim. Biosci.* *3*, 283–303.

Moskalev, A.A. et al. (2013). The role of DNA damage and repair in aging through the prism of Koch-like criteria. *Ageing Res. Rev.* *12*, 661–684.

Muller, M. (2009). Cellular Senescence: Molecular Mechanisms, *In Vivo* Significance, and Redox Considerations. *Antioxid. Redox Signal.* *11*, 59–98.

Nakamura, A.J. et al. (2010). The complexity of phosphorylated H2AX foci

formation and DNA repair assembly at DNA double-strand breaks. *Cell Cycle* 9, 389–397.

Nakamura, K. et al. (2019). H4K20me0 recognition by BRCA1–BARD1 directs homologous recombination to sister chromatids. *Nat. Cell Biol.* 21, 311–318.

Narita, M. et al. (2003). Rb-Mediated Heterochromatin Formation and Silencing of E2F Target Genes during Cellular Senescence. *Cell* 113, 703–716.

Nick McElhinny, S.A. et al. (2005). A Gradient of Template Dependence Defines Distinct Biological Roles for Family X Polymerases in Nonhomologous End Joining. *Mol. Cell* 19, 357–366.

Oberdoerffer, P., and Sinclair, D.A. (2007). The role of nuclear architecture in genomic instability and ageing. *Nat. Rev. Mol. Cell Biol.* 8, 692–702.

Olins, D.E., and Olins, A.L. (2003). Chromatin history: our view from the bridge. *Nat. Rev. Mol. Cell Biol.* 4, 809–814.

Pagès, V., and Fuchs, R.P. (2002). How DNA lesions are turned into mutations within cells? *Oncogene* 21, 8957–8966.

Pandita, T.K., and Richardson, C. (2009). Chromatin remodeling finds its place in the DNA double-strand break response. *Nucleic Acids Res.* 37, 1363–1377.

Panier, S., and Boulton, S.J. (2014). Double-strand break repair: 53BP1 comes into focus. *Nat. Rev. Mol. Cell Biol.* 15, 7–18.

Panier, S., and Durocher, D. (2013). Push back to respond better: regulatory inhibition of the DNA double-strand break response. *Nat. Rev. Mol. Cell Biol.* 14, 661–672.

Pannicke, U. et al. (2004). Functional and biochemical dissection of the structure-specific nuclease ARTEMIS. *EMBO J.* 23, 1987–1997.

Pannunzio, N.R. et al. (2018). Nonhomologous DNA end-joining for repair of DNA double-strand breaks. *J. Biol. Chem.* 293, 10512–10523.

- Parry, A.J., and Narita, M. (2016). Old cells, new tricks: chromatin structure in senescence. *Mamm. Genome* 27, 320–331.
- Paull, T.T. et al. (2000). A critical role for histone H2AX in recruitment of repair factors to nuclear foci after DNA damage. *Curr. Biol.* 10, 886–895.
- Paull, T.T., and Gellert, M. (1998). The 3' to 5' exonuclease activity of Mre 11 facilitates repair of DNA double-strand breaks. *Mol. Cell* 1, 969–979.
- Pedro de Magalhães, J. (2004). From cells to ageing: a review of models and mechanisms of cellular senescence and their impact on human ageing. *Exp. Cell Res.* 300, 1–10.
- Peleg, S. et al. (2016). The Metabolic Impact on Histone Acetylation and Transcription in Ageing. *Trends Biochem. Sci.* 41, 700–711.
- Phipps, S.M.O. et al. (2007). Aging cell culture: methods and observations. *Methods Mol. Biol.* 371, 9–19.
- Pokhrel, N. et al. (2017). Monitoring Replication Protein A (RPA) dynamics in homologous recombination through site-specific incorporation of non-canonical amino acids. *Nucleic Acids Res.* 45, 9413–9426.
- Polo, S.E., and Jackson, S.P. (2011). Dynamics of DNA damage response proteins at DNA breaks: a focus on protein modifications. *Genes Dev.* 25, 409–433.
- Pustovalova, M. et al. (2016). Accumulation of spontaneous γ H2AX foci in long-term cultured mesenchymal stromal cells. *Aging (Albany, NY)*. 8, 3498–3506.
- Rai, T.S. et al. (2014). HIRA orchestrates a dynamic chromatin landscape in senescence and is required for suppression of neoplasia. *Genes Dev.* 28, 2712–2725.
- Ramsden, D.A. (2011). Polymerases in nonhomologous end joining: building a bridge over broken chromosomes. *Antioxid. Redox Signal.* 14, 2509–2519.

Rogakou, E.P. et al. (1998). DNA double-stranded breaks induce histone H2AX phosphorylation on serine 139. *J. Biol. Chem.* *273*, 5858–5868.

Rothkamm, K. et al. (2015). DNA damage foci: Meaning and significance. *Environ. Mol. Mutagen.* *56*, 491–504.

Roy, R. et al. (2011). BRCA1 and BRCA2: different roles in a common pathway of genome protection. *Nat. Rev. Cancer* *12*, 68–78.

Rübe, C.E. et al. (2011). Accumulation of DNA damage in hematopoietic stem and progenitor cells during human aging. *PLoS One* *6*, e17487.

Rubin, H. (1997). Cell aging in vivo and in vitro. *Mech. Ageing Dev.* *98*, 1–35.

de Ruijter, A.J.M. et al. (2003). Histone deacetylases (HDACs): characterization of the classical HDAC family. *Biochem. J.* *370*, 737–749.

Russell, B. et al. (2011). Chromosome Breakage Is Regulated by the Interaction of the BLM Helicase and Topoisomerase II α . *Cancer Res.* *71*, 561–571.

Sabarinathan, R. et al. (2016). Nucleotide excision repair is impaired by binding of transcription factors to DNA. *Nature* *532*, 264–267.

San Filippo, J. et al. (2008). Mechanism of Eukaryotic Homologous Recombination. *Annu. Rev. Biochem.* *77*, 229–257.

Sartori, A.A. et al. (2007). Human CtIP promotes DNA end resection. *Nature* *450*, 509–514.

Scher, M.B. et al. (2007). SirT3 is a nuclear NAD⁺-dependent histone deacetylase that translocates to the mitochondria upon cellular stress. *Genes Dev.* *21*, 920–928.

Schindelin, J. et al. (2012). Fiji: an open-source platform for biological-image analysis. *Nat. Methods* *9*, 676–682.

Schneider, A. et al. (2013). Acetyltransferases (HATs) as Targets for

- Neurological Therapeutics. *Neurotherapeutics* 10, 568–588.
- Sedelnikova, O.A. et al. (2004). Senescing human cells and ageing mice accumulate DNA lesions with unreparable double-strand breaks. *Nat. Cell Biol.* 6, 168–170.
- Sedelnikova, O.A. et al. (2008). Delayed kinetics of DNA double-strand break processing in normal and pathological aging. *Aging Cell* 7, 89–100.
- Seluanov, A. et al. (2004). DNA end joining becomes less efficient and more error-prone during cellular senescence. *Proc. Natl. Acad. Sci.* 101, 7624–7629.
- Seluanov, A. et al. (2007). Changes in the level and distribution of Ku proteins during cellular senescence. *DNA Repair (Amst)*. 6, 1740–1748.
- Serrano, M. et al. (1997). Oncogenic ras Provokes Premature Cell Senescence Associated with Accumulation of p53 and p16INK4a. *Cell* 88, 593–602.
- Seto, E., and Yoshida, M. (2014). Erasers of Histone Acetylation: The Histone Deacetylase Enzymes. *Cold Spring Harb. Perspect. Biol.* 6, a018713.
- Shaltiel, I.A. et al. (2015). The same, only different - DNA damage checkpoints and their reversal throughout the cell cycle. *J. Cell Sci.* 128, 607–620.
- Sharma, G.G. et al. (2010). MOF and Histone H4 Acetylation at Lysine 16 Are Critical for DNA Damage Response and Double-Strand Break Repair. *Mol. Cell. Biol.* 30, 3582–3595.
- Shiloh, Y. (2003). ATM and related protein kinases: safeguarding genome integrity. *Nat. Rev. Cancer* 3, 155–168.
- Shogren-Knaak, M. (2006). Histone H4-K16 Acetylation Controls Chromatin Structure and Protein Interactions. *Science (80-.)*. 311, 844–847.
- Shogren-Knaak, M., and Peterson, C.L. (2006). Switching on Chromatin: Mechanistic Role of Histone H4-K16 Acetylation. *Cell Cycle* 5, 1361–1365.
- Sidler, C. et al. (2017). Epigenetic Regulation of Cellular Senescence and

Aging. *Front. Genet.* **8**, 138.

Sims, R.J., and Reinberg, D. (2008). Is there a code embedded in proteins that is based on post-translational modifications? *Nat. Rev. Mol. Cell Biol.* **9**, 815–820.

Smith, E., and Shilatifard, A. (2010). The Chromatin Signaling Pathway: Diverse Mechanisms of Recruitment of Histone-Modifying Enzymes and Varied Biological Outcomes. *Mol. Cell* **40**, 689.

Smith, E.R. et al. (2005). A human protein complex homologous to the *Drosophila* MSL complex is responsible for the majority of histone H4 acetylation at lysine 16. *Mol. Cell. Biol.* **25**, 9175–9188.

Sobhian, B. et al. (2007). RAP80 Targets BRCA1 to Specific Ubiquitin Structures at DNA Damage Sites. *Science (80-.)*. **316**, 1198–1202.

Solinger, J.A. et al. (2001). Rad54 protein stimulates heteroduplex DNA formation in the synaptic phase of DNA strand exchange via specific interactions with the presynaptic Rad51 nucleoprotein filament¹¹Edited by M. Belfort. *J. Mol. Biol.* **307**, 1207–1221.

Sterner, D.E., and Berger, S.L. (2000). Acetylation of Histones and Transcription-Related Factors. *Microbiol. Mol. Biol. Rev.* **64**, 435.

Steunou, A. et al. (2014). Regulating Chromatin by Histone Acetylation. In: *Fundamentals of Chromatin*, New York, NY: Springer New York, 147–212.

Stracker, T.H. et al. (2007). The carboxy terminus of NBS1 is required for induction of apoptosis by the MRE11 complex. *Nature* **447**, 218–221.

Strahl, B.D., and Allis, C.D. (2000). The language of covalent histone modifications. *Nature* **403**, 41–45.

Stucki, M. et al. (2005). MDC1 Directly Binds Phosphorylated Histone H2AX to Regulate Cellular Responses to DNA Double-Strand Breaks. *Cell* **123**, 1213–

1226.

Stucki, M., and Jackson, S.P. (2006). γ H2AX and MDC1: Anchoring the DNA-damage-response machinery to broken chromosomes. *DNA Repair (Amst)*. *5*, 534–543.

Sukup-Jackson, M.R. et al. (2014). Rosa26-GFP Direct Repeat (RaDR-GFP) Mice Reveal Tissue- and Age-Dependence of Homologous Recombination in Mammals In Vivo. *PLoS Genet*. *10*, e1004299.

Sun, Y. et al. (2005). A role for the Tip60 histone acetyltransferase in the acetylation and activation of ATM. *Proc. Natl. Acad. Sci*. *102*, 13182–13187.

Suwaki, N. et al. (2011). RAD51 paralogs: Roles in DNA damage signalling, recombinational repair and tumorigenesis. *Semin. Cell Dev. Biol*. *22*, 898–905.

Sy, S.M.H. et al. (2009). PALB2 is an integral component of the BRCA complex required for homologous recombination repair. *Proc. Natl. Acad. Sci*. *106*, 7155–7160.

Symington, L.S. (2016). Mechanism and regulation of DNA end resection in eukaryotes. *Crit. Rev. Biochem. Mol. Biol*. *51*, 195–212.

Tadi, S.K. et al. (2016). PAXX Is an Accessory c-NHEJ Factor that Associates with Ku70 and Has Overlapping Functions with XLF. *Cell Rep*. *17*, 541–555.

Taipale, M. et al. (2005). hMOF histone acetyltransferase is required for histone H4 lysine 16 acetylation in mammalian cells. *Mol. Cell. Biol*. *25*, 6798–6810.

Tang, J. et al. (2013). Acetylation limits 53BP1 association with damaged chromatin to promote homologous recombination. *Nat. Struct. Mol. Biol*. *20*, 317–325.

Tarutani, M. et al. (2003). Inducible activation of Ras and Raf in adult epidermis. *Cancer Res*. *63*, 319–323.

Tigges, J. et al. (2014). The hallmarks of fibroblast ageing. *Mech. Ageing Dev*.

138, 26–44.

Titus, S. et al. (2013). Impairment of BRCA1-Related DNA Double-Strand Break Repair Leads to Ovarian Aging in Mice and Humans. *Sci. Transl. Med.* 5, 172ra21.

Tollervey, J.R., and Lunyak, V. V. (2012). Epigenetics. *Epigenetics* 7, 823–840.

Tsurumi, A., and Li, W. (2012). Global heterochromatin loss. *Epigenetics* 7, 680–688.

Uziel, T. et al. (2003). Requirement of the MRN complex for ATM activation by DNA damage. *EMBO J.* 22, 5612.

Vaidya, A. et al. (2014). Knock-In Reporter Mice Demonstrate that DNA Repair by Non-homologous End Joining Declines with Age. *PLoS Genet.* 10, e1004511.

Vaquero, A. et al. (2006). SirT2 is a histone deacetylase with preference for histone H4 Lys 16 during mitosis. *Genes Dev.* 20, 1256–1261.

Vaquero, A. et al. (2007a). NAD⁺-dependent deacetylation of H4 lysine 16 by class III HDACs. *Oncogene* 26, 5505–5520.

Vaquero, A. et al. (2007b). SIRT1 regulates the histone methyl-transferase SUV39H1 during heterochromatin formation. *Nature* 450, 440–444.

Venne, A.S. et al. (2014). The next level of complexity: Crosstalk of posttranslational modifications. *Proteomics* 14, 513–524.

Vijg, J., and Suh, Y. (2013). Genome Instability and Aging. *Annu. Rev. Physiol.* 75, 645–668.

Di Virgilio, M. et al. (2013). Rif1 prevents resection of DNA breaks and promotes immunoglobulin class switching. *Science* 339, 711–715.

Vogel, H. et al. (1999). Deletion of Ku86 causes early onset of senescence in mice. *Proc. Natl. Acad. Sci.* 96, 10770–10775.

- Vyjayanti, V.N., and Rao, K.S. (2006). DNA double strand break repair in brain: Reduced NHEJ activity in aging rat neurons. *Neurosci. Lett.* 393, 18–22.
- Wang, A.S., and Dreesen, O. (2018). Biomarkers of Cellular Senescence and Skin Aging. *Front. Genet.* 9, 247.
- Wang, B. et al. (2007). Abraxas and RAP80 Form a BRCA1 Protein Complex Required for the DNA Damage Response. *Science (80-.)*. 316, 1194–1198.
- Weterings, E., and Chen, D.J. (2008). The endless tale of non-homologous end-joining. *Cell Res.* 18, 114–124.
- Weterings, E., and van Gent, D.C. (2004). The mechanism of non-homologous end-joining: a synopsis of synopsis. *DNA Repair (Amst)*. 3, 1425–1435.
- White, R.R. et al. (2013). Double-Strand Break Repair by Interchromosomal Recombination: An In Vivo Repair Mechanism Utilized by Multiple Somatic Tissues in Mammals. *PLoS One* 8, e84379.
- White, R.R., and Vijg, J. (2016). Do DNA Double-Strand Breaks Drive Aging? *Mol. Cell* 63, 729–738.
- Wu, L., and Hickson, I.D. (2003). The Bloom's syndrome helicase suppresses crossing over during homologous recombination. *Nature* 426, 870–874.
- Yan, J. et al. (2007). The Ubiquitin-Interacting Motif-Containing Protein RAP80 Interacts with BRCA1 and Functions in DNA Damage Repair Response. *Cancer Res.* 67, 6647–6656.
- Yu, X., and Chen, J. (2004). DNA Damage-Induced Cell Cycle Checkpoint Control Requires CtIP, a Phosphorylation-Dependent Binding Partner of BRCA1 C-Terminal Domains. *Mol. Cell. Biol.* 24, 9478–9486.
- Zhang, F. et al. (2009). PALB2 Links BRCA1 and BRCA2 in the DNA-Damage Response. *Curr. Biol.* 19, 524–529.
- Zhang, R. et al. (2007). Molecular Dissection of Formation of Senescence-

Associated Heterochromatin Foci. *Mol. Cell. Biol.* 27, 2343–2358.

Zimmermann, M. et al. (2013). 53BP1 Regulates DSB Repair Using Rif1 to Control 5' End Resection. *Science* (80-.). 339, 700–704.

Ziv, Y. et al. (2006). Chromatin relaxation in response to DNA double-strand breaks is modulated by a novel ATM- and KAP-1 dependent pathway. *Nat. Cell Biol.* 8, 870–876.

Zou, Y. et al. (2006). Functions of human replication protein A (RPA): From DNA replication to DNA damage and stress responses. *J. Cell. Physiol.* 208, 267–273.





Annex I

Identification of reference genes for RT-qPCR data normalisation in aging studies

Lourdes González-Bermúdez^{1, †}, Teresa Anglada^{1, †}, Anna Genescà¹, Marta Martín Flix^{1, §,*} and Mariona Terradas^{1,2, §,*}

¹Departament de Biologia Cel·lular, Fisiologia i Immunologia, Facultat de Biociències, Universitat Autònoma de Barcelona, Bellaterra, Spain

²Current address: Hereditary Cancer Program, Catalan Institute of Oncology, IDIBELL, Hospitalet de Llobregat, Barcelona, Spain

[†]These authors contributed equally to the study.

[§]These authors contributed equally to this work.

*Corresponding author: correspondence should be addressed to MTI (email: mterradas@idibell.cat) or MMF (email: Marta.Martin@uab.cat)

ACCEPTED IN SCIENTIFIC REPORTS

Abstract

Aging is associated with changes in gene expression levels that affect cellular functions and predispose to age-related diseases. The use of candidate genes whose expression remains stable during aging is required to correctly address the age-associated variations in expression levels. Reverse transcription quantitative-polymerase chain reaction (RT-qPCR) has become a powerful approach for sensitive gene expression analysis. Reliable RT-qPCR assays rely on the normalisation of the results to stable reference genes. Taken these data together, here we evaluated the expression stability of eight frequently used reference genes in three aging models: oncogene-induced senescence (OIS), *in vitro* and *in vivo* aging. Using NormFinder and geNorm algorithms, we identified that the most stable reference gene pairs were *PUM1* and *TBP* in OIS, *GUSB* and *PUM1* for *in vitro* aging and *GUSB* and *OAZ1* for *in vivo* aging. To validate these candidates, we used them to normalise the expression data of *CDKN1A*, *APOD* and *TFRC* genes, whose expression is known to be affected during OIS, *in vitro* and *in vivo* aging. This study demonstrates that accurate normalisation of RT-qPCR data is crucial in aging research and provides a specific subset of stable reference genes for future aging studies.

Introduction

Aging is a complex physiological process that affects organismal, tissue and cellular levels, and it is characterised by a persistent loss of cellular and tissue integrity that leads to impaired biological function and increased risk of pathologies and diseases¹. Hayflick and Moorehead² proved that normal cells have limited proliferation capability in culture and enter senescence due to the loss of telomeric integrity, after extensive replicative shortening, or the accumulation of unreparable DNA damage^{3,4}. Since then, studies using cells aged *in vitro* after extensive passaging have been extensively used in aging research. Additionally, fibroblast strains, such as BJ or IMR90, have been used to generate stable models of inducible senescence in which the proliferative arrest involves the activation of both the retinoblastoma and p53 pathways, by an activating mutation of an oncogene, termed as oncogene induced senescence (OIS)⁵. Living organisms also produce senescent cells in their tissues, whose frequency increases with age¹ and contributes to the age-associated decline of regenerative capacity, tissue inflammation and the development of age-related diseases^{6,7}. While *in vitro* induced senescent cells are almost homogeneous populations, regarding *in vivo* aged tissues, senescent cells coexist with young cells and with old cells that have accumulated many divisions but have not yet reached senescence. Thus, cells derived from old individuals share cellular and molecular phenotypes with *in vitro* senescent cells, but it is not clear whether these phenotypes are completely overlapping⁸. For this reason, when possible, researchers use *in vivo* model studies in which cells from young and elderly donors are used immediately after obtention or after a few passages in culture. Although these are the currently used models or approaches to study aging, careful consideration must be given to the differences among them.

Profound changes in gene expression are important determinants of organismal aging^{9,10}, and many genes change their expression with age^{8,11-13}.

Therefore, understanding gene expression changes provides insights into the molecular mechanisms underlying normal and pathological aging processes. Genome-wide studies in different species have identified sets of genes displaying age-associated expression alterations as promising biomarkers of aging^{4,14}. For instance, a meta-analysis of the age-associated gene expression profile has identified genes involved in the stress response, such as hypoxia-inducible factor 1-alpha (*HIF1A*) or apolipoprotein D (*APOD*), and in cell cycle regulation and apoptosis, such as cyclin dependent kinase inhibitor 1A (*CDKN1A*) and annexins, to be upregulated in a wide variety of tissues from humans, mice and rats during *in vivo* aging¹². Other *in vivo* aging studies in mammals have identified the downregulation of genes mainly associated with metabolism and mitochondrial function^{12,15,16}.

In contrast, age-associated variations in gene expression may also reflect the selected aging model. For example, it is possible to distinguish the molecular phenotype of human fibroblasts that have acquired the senescent phenotype *in vitro* from that of fibroblasts obtained from old individuals⁸. A cluster analysis from a cDNA microarray that evaluated the expression of 384 cancer-related genes in three types of aging: (i) replicative senescent fibroblasts, (ii) fibroblasts from a progeria patient and (iii) primary fibroblasts from an elderly donor, revealed that replicative senescent cells were clearly different from the other two aging models¹⁷. In a correlation-based comparison of gene expression in microarray datasets from senescent and *in vivo* aged human and mouse cells, similar expression signatures between the cellular senescent and *in vivo* aged cells could be established in mouse, but not in human cells. In conclusion, gene expression varies with age, but this variation is also influenced by the aging model used in the study¹⁸.

A powerful tool used to evaluate changes in gene expression is the reverse transcription quantitative-polymerase chain reaction (RT-qPCR) technique. Features including great accuracy, high sensitivity, reproducibility and high-throughput make RT-qPCR the most prevalent technique to assess

mRNA expression^{19,20}. Relative quantification of data obtained from RT-qPCR is used to determine changes in gene expression across multiple samples or conditions after normalisation to an internal reference gene²⁰. Thus, the accuracy of RT-qPCR relies on the availability of reference genes that maintain stable expression levels under the tested conditions, which could be used as endogenous controls for normalisation^{21,22}. Consequently, identification of appropriate reference genes is a crucial step in the correct development of RT-qPCR assays.

The ideal reference gene should exhibit stable expression in different cell types, tissues and experimental conditions or treatments. Traditionally, genes related to basal cellular function have been extensively used as reference genes²³. Nevertheless, numerous studies have demonstrated that the expression of reference genes varies under different conditions, reflecting the importance of validating the expression stability of the selected reference genes under the desired experimental settings before performing the RT-qPCR assays²⁴⁻²⁶. Focusing on human aging, frequently used reference genes such as β -2 microglobulin ($\beta 2M$) showed age-dependent variation with increased expression in aged muscle cells²⁷. In addition, glucuronidase beta (*GUSB*) was found to be the most suitable reference gene, whereas *18s* was found to be the least stable gene for expression studies in peripheral blood mononuclear cells from young and aged subjects²⁸. Recently, transmembrane protein 199 (*TMEM199*) has been described as a new candidate reference gene to normalise RT-qPCR data of senescent cells²⁹. These findings reveal differences in gene expression associated with species, tissues and age models and bring to light the difficulties in finding a stable reference gene for expression studies during aging. Therefore, the purpose of this study is to identify a set of stable reference genes that are suitable for the analysis of human age-associated gene expression changes in different models of aging.

To accomplish this goal, we analysed the impact of OIS, *in vitro* and *in vivo* aging on the expression stability of eight commonly used reference genes

that play a role in different biological functions and that have been previously tested in age-related studies^{23,27-30}: glyceraldehyde-3-phosphate dehydrogenase (*GAPDH*) and *GUSB* are involved in basal cellular functions; β -actin (*ACTB*) is an essential component of the cytoskeleton³¹; hypoxanthine guanine phosphoribosyl transferase (*HPRT1*) participates in nucleotide synthesis³²; pumilio-homolog 1 (*PUM1*) is involved in translation regulation³³; TATA box binding protein (*TBP*) functions in transcription regulation³⁴; ornithine decarboxylase antizyme 1 (*OAZ1*) is related to protein biosynthesis³⁵; *TMEM199* is involved in Golgi homeostasis³⁶. To analyse the expression stability of the candidate reference genes and to select the genes that are most suitable, we used the statistical software packages NormFinder³⁷ and geNorm³⁸. Finally, to validate their reliability, we evaluated the expression of genes that are known to change with aging after normalisation with the selected candidate reference genes.

Results

Establishment of senescence and aging models and testing of primers for reference genes

To determine the impact of aging on the stability of reference genes, we employed three aging models. The first model examined was the OIS model, which was established in immortalised primary human BJ foreskin fibroblasts (BJ fibroblasts) transduced with the *H-RAS* oncogene fused to a 4-hydroxytamoxifen (4-OHT)-responsive Estrogen Receptor (ER) ligand binding domain³⁹. Upon eight days of 4-OHT treatment, the cells were stained for senescence-associated beta-galactosidase (SA- β gal) activity. The percentage of BJ fibroblasts displaying SA- β gal activity after 4-OHT treatment was significantly higher (60.25%) compared to the control conditions (2.85%) (Chi-square test; $p < 0.001$) (Figure S1). The second model employed was the *in vitro* aging model, which consists of the serial culture of primary human dermal fibroblasts (HDFs), allowing the analysis of gene expression in a constant

environment over time⁴⁰. Primary HDFs have a limited growth potential and reach their replicative limit after 30 passages in culture⁴¹. Thus, we established a distinction between young cells (early passage, EP), which were cells with less than 10 passages in culture, and old cells (late passage, LP), which were cells with more than 20 passages in culture. Finally, we used Human Mammary Epithelial Cells (HMECs) derived from the healthy tissue of young (≤ 19 years of age) and old (≥ 61 years of age) donors as a model for *in vivo* aging.

To assess the RT-qPCR assay performance, we first calculated the amplification efficiency for all the primer pairs analysed in this study. RT-qPCR primer efficiencies were obtained from the slopes of their corresponding standard curves (Figure 1, Table 1). Primer efficiencies ranged from 85.61% to 104.61%, values included in the optimal efficiency range^{42,43}, and standard curves showed high linearity with correlation coefficients (R^2) between 0.971 and 0.999 (Table 1). Evaluation of the melting curves revealed single peaks for each primer pair, which confirmed the specificity of the amplifications (Figure S2).

Descriptive statistics of candidate reference genes

To study the expression profile of the candidate reference genes in the different aging models, RT-qPCR experiments were performed and the mean cycle threshold (Ct) value for each gene was calculated and the variation in expression among different samples, defined as the coefficient of variation (CV), was obtained for each gene. The CV should be small for a reference gene; thus, we considered that a stable and reliable reference gene should have a CV lower than 2.

In the OIS model, most reference genes showed very few intragroup expression variations, with *PUM1*, *HPRT1* and *TBP* being the reference genes that exhibited the most stable expression levels (CV < 2 for control and senescent BJ fibroblasts), as Ct values remained constant within control and senescent cells (Figure 2a). *OAZ1* and *TMEM199* displayed strong intragroup

variations, showing the highest CV values (Figure 2a). In senescent BJ fibroblasts, *GAPDH* and *ACTB* showed the strongest significant decrease in their expression level in comparison to control fibroblasts. To compare variations in reference genes expression with senescence, a one-way between subjects ANOVA using the Ct values of each reference gene was conducted, revealing a significant effect of OIS on reference gene expression [F (15, 76) = 2.045, $p = 0.0224$]. *GAPDH* expression levels varied between control (mean Ct values: 19.48; standard deviation (SD): 0.40) and senescent BJ fibroblasts (mean Ct values: 17.11; SD: 0.21) (Bonferroni post-hoc test; $p < 0.001$) (Figure 2a). Similarly, expression levels of *ACTB* displayed low intragroup variations, but they significantly differed between control (mean Ct value: 19.66; SD: 0.42) and senescent BJ fibroblasts (mean Ct value: 17.90; SD: 0.44) (Bonferroni post-hoc test; $p < 0.001$) (Figure 2a). These results point to *PUM1*, *HPRT1* and *TBP* as the most stable reference genes for expression studies during OIS. These results point to *PUM1*, *HPRT1* and *TBP* as the most stable reference genes for expression studies during OIS.

Regarding the expression of candidate reference genes in *in vitro* aged HDFs, we found *GUSB* and *PUM1* to have the lowest intragroup expression variations, reflected by the smallest CV values in EP and LP HDFs (Figure 2b). Conversely, the highest variable intragroup expression levels were detected for *OAZ1* and *TBP* ($CV > 2$) (Figure 2b). We also detected a significant effect of the *in vitro* age of HDFs on reference gene expression after conducting a one-way ANOVA test [F (15, 73) = 2.337, $p = 0.0086$]. The Bonferroni post-hoc test showed that the expression level of *GAPDH* significantly varied between early (mean Ct value: 22.74; SD: 0.33) and late (mean Ct value: 20.46; SD: 0.23) passage HDFs ($p = 0.0177$) (Figure 2b). Expression level of *HPRT1* was also found to significantly vary between EP (mean Ct value: 25.65; SD: 0.41) and LP (mean Ct value: 28.48; SD: 0.42) HDFs (Bonferroni post-hoc test; $p = 0.0048$) (Figure 2b). Therefore, *GUSB* and *PUM1* seem to be the most suitable reference genes for expression analysis in *in vitro* aging models.

The expression profile of the candidate reference genes suffered from strong intragroup variations in HMECs from older donors, as almost all the reference genes presented a large intragroup Ct variability in aged donors ($CV > 2$) (Figure 2c). However, the strongest intra- and intergroup variations were observed for *TBP*. A significant effect of the donor's age of HMECs on reference gene expression was also found after applying a one-way ANOVA test [$F(15, 239) = 9.936, p < 0.001$]. The post-hoc comparisons using the Bonferroni test indicated that the mean Ct value significantly increased in HMECs from aged donors (mean Ct value: 25.65; SD: 0.47) when compared to HMECs from young women (mean Ct value: 28.81; SD: 2.962) (one-way ANOVA and Bonferroni multiple correction test; $p < 0.001$). Furthermore, the mean Ct values of *GAPDH*, *HPRT1*, *PUM1*, *ACTB* and *TMEM199* were also found to increase significantly in HMECs from aged donors in comparison to HMECs from younger donors (Bonferroni post-hoc test; $p < 0.001$) (Figure 2c). Only *GUSB* and *OAZ1* expression levels showed very little intragroup variation, with no significant differences between HMECs from young and aged donors (Figure 2c). Therefore, these two genes appeared to be the most stable reference genes to study *in vivo* aging.

Expression stability of candidate reference genes

To select appropriate reference genes for each different aging model, genes were ranked based on their expression stability, which was evaluated with two statistical algorithms, NormFinder³⁷ and geNorm³⁸. It should be noted that the ranking of reference genes showed similar trends between both software packages, although with subtle variations, which might be attributed to the differences across algorithms. However, when faced with discrepancies between these methods, the recommended genes are always those closest to the most stable genes, reflecting their ability to be a suitable reference gene.

In OIS, both NormFinder and geNorm revealed that the least stable gene was *OAZ1*, followed by *TMEM199* (Table 2). These genes displayed high levels

of intragroup variation in their expression profile (Figure 2a). On the contrary, NormFinder and geNorm indicated that the most suitable genes to use as a reference gene were *PUM1*, followed by *TBP* and *HPRT1* (Table 2). This classification is in accordance with the expression profiles that we previously obtained (Figure 2a) in which these reference genes were those with the lowest intragroup variability and their expression levels were very similar before and during senescence.

The evaluation of gene stability during *in vitro* aging after applying NormFinder and geNorm agreed in suggesting that *OAZ1* was the least stable gene, together with *TBP* and *ACTB* (Table 2). In accordance to their expression profiles, these genes were those with higher levels of intragroup variation (Figure 2b). Additionally, analysis with NormFinder and geNorm rendered *PUM1* > *GUSB* > *GAPDH* as the most stable genes (Table 2). In agreement with the above results, expression profiles of *GUSB* and *PUM1* were very similar in young and in *in vitro*-aged fibroblasts (Figure 2b). Instead, *GAPDH* levels were very stable within each group, although they significantly decreased during *in vitro* aging, a probable reason for its third position in the ranking (Figure 2b).

For *in vivo* aging studies, NormFinder ranked *GAPDH* < *TBP* < *PUM1* as the least stable genes, while geNorm designated *TBP* < *HPRT1* < *TMEM199* (Table 2). Regarding the most stable genes, NormFinder identified *OAZ1* > *GUSB* > *ACTB*, whereas geNorm showed *GUSB* > *ACTB* > *OAZ1* (Table 2). Consistent with our earlier results, the expression profiles of *OAZ1* and *GUSB* showed stable intragroup levels and no expression differences between HMECs from young and aged donors (Figure 2c).

Finally, an optimal number of reference genes (*n*) for accurate normalisation was calculated by comparing the pairwise variation (*V*) of two sequential normalisation factors ($V_{n/n+1}$) with geNorm. In all aging processes, $V_{2/3} < 0.15$ indicated that two reference genes, among those selected by the

statistical algorithms, were enough to accurately normalise RT-qPCR data (Figure 2d).

Validation of selected reference genes

To validate the reference genes selected by the statistical algorithms as candidates for normalisation, we selected genes whose expression levels have been shown to change with senescence or aging. For each aging process, data were normalised to three distinct groups of reference genes. In agreement with the outcomes of NormFinder and geNorm algorithms, we selected the single most stable gene, the recommended combination of two reference genes and the candidate reference gene with the lowest stability.

Among the various features of senescence, increased expression of *CDKN1A* has been widely used as a biomarker to identify senescent cells⁴⁴. Therefore, we decided to check the *CDKN1A* expression profile in control and senescent BJ fibroblasts. Normalisation with the single most stable reference gene, *PUM1*, resulted in a significant increase of the *CDKN1A* expression level in senescent BJ fibroblasts compared to control BJ fibroblasts (Welch's t-test; $p = 0.0028$) (Figure 3a). The expression of *CDKN1A* was also significantly upregulated in senescent BJ fibroblasts after normalisation to the recommended reference gene pair, *PUM1* and *TBP* (Welch's t-test; $p = 0.0046$) (Figure 3a). These findings confirm that the combination of *PUM1* and *TBP* was also reliable for analysing expression changes of target genes during OIS (Figure 3a). However, when the least stable gene, *OAZ1*, was used for data normalisation, no statistical differences in *CDKN1A* expression were detected between normal and senescent cells. In fact, the *CDKN1A* expression pattern exhibited an opposite trend, decreasing in senescence instead of increasing (Figure 3a) when *OAZ1* was used as the reference gene.

A variety of genes have been shown to be differentially expressed during aging, making them potential markers of aging. Significant overexpression of *APOD* has been described during *in vitro*⁴⁵ and *in vivo* aging¹². Conversely, the

transferrin receptor (*TFRC*) was shown to decrease with age¹². Therefore, we analysed the expression profile of both of these age-related genes to confirm the reliability of the chosen reference genes in models of *in vitro* and *in vivo* aging.

During *in vitro* aging, independent of the reference genes used for normalisation, the expression levels of *APOD* were higher in LP than in EP HDFs, suggesting a very consistent age-dependent increase in the expression level of this gene (Figure 3b). Regarding *TFRC* expression, normalisation with the most stable single gene, *PUM1*, revealed a decrease in *TFRC* expression in LP HDFs in comparison to EP HDFs (Welch's t-test; $p = 0.0261$) (Figure 3b). Furthermore, after normalisation with the most reliable gene pair, *PUM1* and *GUSB*, a decrease in *TFRC* expression in LP HDFs compared to EP HDFs was again observed (Welch's t-test; $p = 0.0098$) (Figure 3b). In contrast, using the least stable reference gene for normalisation, *OAZ1*, statistical differences in *TFRC* levels between young and old cells were not detected (Figure 3b).

To validate reference genes for *in vivo* aging, we compared the expression profiles of *APOD* and *TFRC* between HMECs from one representative young and one representative aged donor. Using the suggested most stable single reference gene, *GUSB*, we observed that *APOD* was upregulated in HMECs from the aged donor compared to HMECs from the younger one (Welch's t-test; $p < 0.001$). Moreover, *TFRC* was downregulated in HMECs from the aged donor (Welch's t-test; $p = 0.0018$) (Figure 3c). Similar results were obtained upon normalisation with the recommended reference gene pair, *GUSB* and *OAZ1* (Figure 3c). Using both reference genes for normalisation, a higher expression of *APOD* was found in HMECs from the aged donor compared to HMECs from the younger one (Welch's t-test; $p = 0.0096$). In the case of *TFRC*, its expression was again downregulated in HMECs from the aged donor (Welch's t-test; $p = 0.0091$) (Figure 3c). Finally, when using *TBP*, the least stable reference gene, both *APOD* and *TFRC* expression levels showed large

variations, reflected by a high SD value, and no statistical differences were displayed between the age groups (Figure 3c).

Discussion

Gene expression analysis has become one of the most powerful tools in many fields of biological research, and RT-qPCR has emerged as the most frequently used approach for highly sensitive and precise quantification of gene expression. The accuracy of RT-qPCR results strongly depends on a careful selection of appropriate reference genes for normalisation of gene expression. Many studies have demonstrated that the expression of commonly-used reference genes varies among different cell types, tissues and experimental conditions^{24,30,38}. Since there are no universal reference genes for accurate normalisation, it is crucial to specifically select the most suitable reference gene for each experimental design.

The aging process is accompanied by gene expression changes that lead to a decline of many cellular functions and to the development of age-related diseases¹. Therefore, to obtain an unbiased comparison of gene expression profiles during aging, it is vital to select the appropriate reference genes. Also, expression of these reference genes may vary among the aging models used. In this study, we evaluated the stability of potential reference genes and selected the most suitable ones for gene expression analysis in three different aging models: OIS, *in vitro* and *in vivo* aging.

We identified *PUM1* and *TBP* as the most stable pair of reference genes for OIS models. Expression analysis of the senescent marker *CDKN1A*⁴⁴, after normalisation to *PUM1* and *TBP*, revealed increased *CDKN1A* expression during OIS. Increased expression levels of *CDKN1A* has been previously described in IMR-90 *ER:RAS* fibroblasts, a classical model used to study OIS in culture, using *GAPDH* or *ACTB* as reference genes⁴⁶. However, we show that these genes display intermediate or low stability values during OIS in BJ fibroblasts. In this regard, experiments of single-cell RT-qPCR have

demonstrated changes in *GAPDH* expression in IMR-90 fibroblasts after bleomycin-induced senescence⁴⁷. Additionally, *GAPDH* and *ACTB* have shown considerable variations in fibroblasts in which senescence was induced using different methods²⁹. These facts emphasise the need to specifically select reference genes depending on the senescence model and on the cell type. Indeed, together with the instability of classical reference genes, the potential use of new reference genes in a strain-dependent manner has been recently reported in senescence studies²⁹. Hence, we strongly advise to choose appropriate genes for every senescent experiment, but we suggest *PUM1* and *TBP* as a starting point for future OIS studies in BJ human fibroblasts.

We found *GUSB* and *PUM1* to be the most stable reference genes for the *in vitro* aging model and *GUSB* and *OAZ1* were determined as the most suitable reference genes for the *in vivo* aging model. Supporting our results, studies using white blood cells from aged mice and human peripheral blood mononuclear cells from young and aged donors also identified *GUSB* as the most stable reference gene^{28,48}. Considering *in vitro* aging, it should be noted that the two most stable reference genes during this process in HDFs coincided with the most stable reference genes for *in vivo* aging in HMECs (*GUSB*) and for senescent BJ fibroblasts (*PUM1*). These results suggest that *in vitro* aging is a model that might share expression characteristics with both the senescence and *in vivo* aging models. Indeed, several studies have used serially cultured somatic cells as an aging-like model that mimics some of the cellular and molecular alterations related to organismal aging^{40,49}. Nevertheless, it should be considered that these reference genes have been identified using human fibroblasts and HMECs, and we cannot reject that using other cell types may cause changes in the appropriate candidate pair. In both *in vivo* and *in vitro* aging models, validation of the most stable reference gene was performed by analysing age-related expression changes of *APOD* and *TFRC*. In both *in vitro* and *in vivo* aging, *APOD* expression increased with age while *TFRC* expression was reduced, which has already been described in

previous studies¹², validating our reference genes. Finally, the MIQE guidelines suggest the use of at least two reference genes and to test whether more than two are necessary⁴². Considering our results, in all the three models tested in our study, at least two reference genes are enough for a strong and reliable normalisation in RT-qPCR experiments.

Remarkably, we observed that most of the candidate reference genes exhibited strong variations in *in vivo* aged cells. These results are in agreement with previously published studies that demonstrated an increased cell-to-cell transcriptional variability in lymphocytes⁵⁰ and cardiomyocytes⁵¹ from aged mice. Age-related heterogeneity of gene expression has also been described in human aging after analysing microarray data sets, including data from the kidney, skeletal muscle and the cerebral cortex⁵². Accumulation of senescent cells in aged tissues has been associated with the loss of their regenerative capacity and the subsequent deterioration of their physiological functions^{6,7}. In this study, we analysed gene expression levels of cells isolated from aged human epithelial mammary tissue. The fact that aged tissues comprise a mixed population of replicative senescent cells, young cells and *in vivo* aged cells could explain the age-associated heterogeneous gene expression profiles described by others^{51,53}. Therefore, we hypothesise that at least part of the large variations in gene expression detected in HMECs during *in vivo* aging are due to the inherent heterogeneity of the *in vivo* aged tissue composition.

Finally, it is worth mentioning that *GAPDH* is one of the most commonly used reference genes, and it has been identified as a reliable reference gene for comparisons between young and old donors of human skeletal muscle²⁷. Conversely, *GADPH* showed expression variability in our three aging models and occupied a middle to low position in the stability ranking of each aging model, again demonstrating the importance of reference gene selection in these types of studies. The intermediate stability value of *GAPDH* supports its extended use as a relatively safe reference gene choice, which generally ensures confidence in the results of RT-qPCR assays. However, variability of

GAPDH expression in aging processes may impede the detection of subtle expression variations in target genes when using *GAPDH* as reference gene.

In summary, we demonstrate that expression of reference genes changes in a specific manner depending on the aging model, and thus it could be concluded that each aging process needs its own subset of reference genes for the reliable normalisation of RT-qPCR data. This study underlines the importance of selecting stable reference genes to correctly quantify gene expression levels during aging. Therefore, this report should be regarded as a guideline for future gene expression analysis, which ultimately leads to a better understanding of the basis of human aging.

Materials and Methods

Cell culture

HDFs and BJ fibroblasts were cultured in Dulbecco's Modified Eagle's Medium (Biowest, Riverside, MO, USA) and supplemented with 10% fetal bovine serum, 1% GlutaMAX and 1% penicillin-streptomycin (Thermo Fisher Scientific Inc., Waltham, MA, USA). Finite lifespan pre-stasis HMECs were a kind gift from Martha Stampfer from Lawrence Berkeley National Laboratory. HMECs were obtained from reduction mammoplasty tissue of 5 donors: 48R (16 years old), 240L (19 years old), 112R (61 years old), 122L (66 years old) and 429ER (72 years old); or peripheral non-tumour containing mastectomy tissue of 1 donor: 353P (72 years old). Donors were classified depending on age into two groups: young donors (YDs, ≤ 19 years old) and aged donors (ADs, ≥ 61 years old). HMECs were cultured using M87A medium supplemented with cholera toxin (Sigma-Aldrich, St. Louis, MO, USA) and oxytocin (Bachem, Torrance, CA, USA), with the addition of 100 U/mL penicillin and 100 $\mu\text{g}/\text{mL}$ of streptomycin (Thermo Fisher Scientific Inc., Waltham, MA, USA)⁵⁵. All the experiments with HMEC cells were performed with population doublings < 20 , calculated from passage 2. Incubation conditions for all cell types were 37 °C and 5% CO₂ atmosphere. Immortalised BJ human fibroblasts

expressing *ER-RASval12* (BJ hTERT ER:RAS) were kindly provided by Maite Huarte's laboratory at CIMA, *Universidad de Navarra*, who generated the cells by infecting BJ fibroblasts (purchased from ATCC, Manassas, VA, USA) with lentiviral particles containing hTERT and ER:RAS. HDFs were commercially obtained from Cell Applications (San Diego, CA, USA).

Senescence induction and detection

Exponentially growing BJ hTERT ER:Ras fibroblasts were treated with 200 nM of 4-OHT (Sigma-Aldrich, St. Louis, MO, USA) for 8 days to induce senescence. After 4-OHT treatment, detection of SA- β -galactosidase activity was performed following the Debacq-Chainiaux et al. protocol⁵⁶. Briefly, cells were fixed with 2% formaldehyde-0.2% glutaraldehyde in 1x PBS for 10 min at room temperature, washed with 1x PBS and treated for 12 h with H₂O containing 40 mM citrate-phosphate buffer (pH 6), 2 mM MgCl₂, 150 mM NaCl, 1 mg/ml of X-Gal, and 5 mM potassium ferricyanide and potassium ferrocyanide. This treatment results in the presence of a blue-dyed precipitate in senescent cells. Cells were subsequently washed with 1x PBS, methanol and distilled water. Pictures identifying senescent cells were captured with an IX71 optic inverted phase contrast microscope that was equipped with a DP20 camera and cell^A software (Olympus, Hamburg, Germany). A total of 100 cells were captured and quantified per condition.

RNA extraction and cDNA synthesis

Confluent cells were washed once with ice cold PBS. Then, PBS was aspirated and TRIzol reagent (Thermo Fisher Scientific Inc., Waltham, MA, USA) was added. After thoroughly mixing, extracts were kept at -80 °C until total RNA from all samples was collected. After thawing TRIzol extracts, chloroform was added at 1:5 (v/v), and RNA was separated from DNA and proteins by centrifugation. 200 μ L of the aqueous phase was then mixed with the same amount of lysis solution of the Maxwell RSC simply RNA kit in conjunction with the Maxwell system (Promega, Madison, WI, USA). The RNA

concentration and purity were evaluated with a NanoDrop 2000 spectrometer (Thermo Fisher Scientific Inc., Waltham, MA, USA). RNA samples with an absorbance ratio OD 260/280 between 1.8–2.1 and OD 260/230 between 2–2.2 were used for further analysis. The quality of the RNA samples was checked by on-chip electrophoresis on the Agilent 2100 Bioanalyzer following the manufacturer's protocol (Agilent Technologies, Santa Clara, CA, USA). The RNA integrity number (RIN) for all the RNA samples was 10, which is the maximum RNA integrity value.

Single-stranded cDNA was synthesised from 1 µg of total RNA in a final volume of 20 µL. For this purpose, the iScript cDNA synthesis kit (Bio-Rad, Hercules, CA, USA) was used and the manufacturer's instructions were followed. cDNA was stored at -20 °C for future use. The cDNA products were tested for genomic DNA contamination using agarose gel electrophoresis.

Selection of reference genes and primers design

Eight candidate reference genes were selected to test their stability among different aging processes. From the eight candidate reference genes, *ACTB*, *OAZ1* and *TMEM199* primer pairs were obtained from the literature^{29,30}. The rest of primer sets were designed using Primer3 online software⁵⁷, and after *in silico* validation with UCSC Genome Browser (<https://genome.ucsc.edu>), were purchased from Condalab (Metabion, Munich, Germany).

Quantitative PCR and primer efficiency calculations

Quantitative PCR reactions were performed using the universal SYBR Green Supermix (Bio-Rad, Hercules, CA, USA) on a CFX96 thermal cycler with Bio-Rad CFX Manager software (Bio-Rad, Hercules, CA, USA). 50 ng of cDNA were used for each reaction. The amplification program was initiated at 95°C for 3 min followed by 40 cycles of 10 s at 95 °C and 30 s at 60°C. After amplification, an additional thermal denaturising cycle (temperature ranged between 65 °C and 95 °C in 0.5 °C increments) was performed to obtain the melting curves of the RT-qPCR products and verify amplification specificity.

The reactions for each sample were run in triplicates, unless otherwise specified. RT-qPCR primer efficiency was tested for each primer pair using 10-fold serial dilutions of cDNA chosen among the samples. The mean threshold cycle (Ct) values for each serial dilution was plotted against the logarithm of the cDNA dilution factor. RT-qPCR primer efficiencies were calculated using the following equation: $E = ((10^{\frac{-1}{slope}}) - 1) * 100$. The efficiency of all designed primer pairs ranged from 80% to 110%, which is considered the optimal efficiency value^{42,43}.

Data analysis

To evaluate the stability of the candidate reference genes, two Add-in Microsoft Excel algorithms were applied, NormFinder³⁷ and geNorm³⁸. NormFinder provides a ranking of tested genes based on a stability value calculated from both intra- and intergroup variations of gene expression. GeNorm calculates the *M* value, a stability measure for each reference gene. A low *M* value reveals higher expression stability. Genes with an *M* value above 1.5 were considered inappropriate for normalisation. The algorithm identifies the two most stable reference genes by stepwise exclusion of the least stable gene. GeNorm also calculates the number of genes required for an optimal normalisation. Additionally, it compares the pairwise variation (*V*) of the two most stable genes with the remaining genes; thus, it calculates the *V* value of V_n/V_{n+1} between two sequential normalisation factors. A variation of V_n/V_{n+1} below 0.15 suggests that no additional reference gene is required for normalisation.

Validation of candidate reference genes

To validate the reliability of the reference genes for RT-qPCR data normalisation, the relative expression of *CDKN1A*, *APOD* and *TFRC* was analysed. The primers' specifications for these genes are listed in Supplementary Table 1. Expression of these genes was analysed using the most stable single and pair of reference genes and also the least stable gene. Normalisation of RT-qPCR data using two reference genes was performed with the geometric mean of the multiple reference genes (f) applying the formula below^{38,58} (*goi*, gene of interest; *ref*, reference gene):

$$\text{Normalised relative quantities} = \frac{2^{\Delta Ct, goi}}{2^{\frac{1}{f} \sum_{i=1}^f \Delta Ct, ref_i}}$$

A 100% PCR efficiency was assumed (reflected by a value of 2 at the base of the exponential function). Relative fold changes in gene expression were obtained according to the $2^{-\Delta\Delta Ct}$ method⁵⁹.

Statistical analysis

Statistical procedures and graph plotting were conducted in GraphPad Prism 6.01 (GraphPad Software, La Jolla, CA, USA). The coefficient of variation (CV) is defined as the ratio of the standard deviation to the mean. The Chi-square test was used to compare differences between the frequency of senescent cells. Means of different groups were compared and analysed using one-way ANOVA, followed by Bonferroni's post-hoc test to generate adjusted p-values or Welch's t-test. Differences were considered statistically significant when the *p*-value was less than 0.05.

Ethical statement

The authors declare that all methods were carried out in accordance with relevant guidelines and regulations and that all experimental protocols

were approved by *Universitat Autònoma de Barcelona*. HMEC specimens were obtained in the laboratory of Marta Stampfer between 1977–1981. This was before the current Institutional Review Board (IRB) regulations were in place, and consent at that time was covered by the hospitals' consent forms, which allowed the pathologists to use or distribute discarded surgical material at their discretion.

References

1. López-Otín, C., Blasco, M. A., Partridge, L., Serrano, M. & Kroemer, G. The Hallmarks of Aging. *Cell* **153**, 1194–1217 (2013).
2. Hayflick, L. & Moorhead, P. S. The serial cultivation of human diploid cell strains. *Exp. Cell Res.* **25**, 585–621 (1961).
3. Hernandez-Segura, A., Nehme, J. & Demaria, M. Hallmarks of Cellular Senescence. *Trends Cell Biol.* **28**, 436–453 (2018).
4. Sharpless, N. E. & Sherr, C. J. Forging a signature of in vivo senescence. *Nat. Rev. Cancer* **15**, 397–408 (2015).
5. Chandeck, C. & Mooi, W. J. Oncogene-induced cellular senescence. *Adv. Anat. Pathol.* **17**, 42–8 (2010).
6. Childs, B. G., Durik, M., Baker, D. J. & Deursen, J. M. van. Cellular senescence in aging and age-related disease: from mechanisms to therapy. *Nat. Med.* **21**, 1424 (2015).
7. Campisi, J. Aging, Cellular Senescence, and Cancer. *Annu. Rev. Physiol.* **75**, 685–705 (2013).
8. Faraonio, R., Pane, F., Intrieri, M., Russo, T. & Cimino, F. In vitro acquired cellular senescence and aging-specific phenotype can be distinguished on the basis of specific mRNA expression. *Cell Death Differ.* **9**, 862–864 (2002).

9. Fraga, M. F. & Esteller, M. Epigenetics and aging: the targets and the marks. *Trends Genet.* **23**, 413–8 (2007).
10. Fraga, M. F. Genetic and epigenetic regulation of aging. *Curr. Opin. Immunol.* **21**, 446–453 (2009).
11. Cristofalo, V. J., Volker, C., Francis, M. K. & Tresini, M. Age-dependent modifications of gene expression in human fibroblasts. *Crit. Rev. Eukaryot. Gene Expr.* **8**, 43–80 (1998).
12. de Magalhães, J. P., Curado, J. & Church, G. M. Meta-analysis of age-related gene expression profiles identifies common signatures of aging. *Bioinformatics* **25**, 875–881 (2009).
13. Eisenberg, E. & Levanon, E. Y. Human housekeeping genes, revisited. *Trends Genet.* **29**, 569–574 (2013).
14. Stegeman, R. & Weake, V. M. Transcriptional Signatures of Aging. *J. Mol. Biol.* **429**, 2427–2437 (2017).
15. Lee, C.-K., Allison, D. B., Brand, J., Weindruch, R. & Prolla, T. A. Transcriptional profiles associated with aging and middle age-onset caloric restriction in mouse hearts. *Proc. Natl. Acad. Sci.* **99**, 14988–14993 (2002).
16. Peters, M. J. et al. The transcriptional landscape of age in human peripheral blood. *Nat. Commun.* **6**, 8570 (2015).
17. Park, W.-Y. et al. Gene Profile of Replicative Senescence Is Different from Progeria or Elderly Donor. *Biochem. Biophys. Res. Commun.* **282**, 934–939 (2001).
18. Wennmalm, K., Wahlestedt, C. & Larsson, O. The expression signature of in vitro senescence resembles mouse but not human aging. *Genome Biol.* **6**, R109 (2005).

19. Nolan, T., Hands, R. E. & Bustin, S. A. Quantification of mRNA using real-time RT-PCR. *Nat. Protoc.* **1**, 1559–1582 (2006).
20. Schmittgen, T. D. & Livak, K. J. Analyzing real-time PCR data by the comparative C(T) method. *Nat. Protoc.* **3**, 1101–8 (2008).
21. Wong, M. L. & Medrano, J. F. Real-time PCR for mRNA quantitation. *Biotechniques* **39**, 75–85 (2005).
22. Bustin, S. A. et al. The need for transparency and good practices in the qPCR literature. *Nat. Methods* **10**, 1063–1067 (2013).
23. Rydbirk, R. et al. Assessment of brain reference genes for RT-qPCR studies in neurodegenerative diseases. *Sci. Rep.* **6**, 1–11 (2016).
24. Suzuki, T., Higgins, P. J. & Crawford, D. R. Control Selection for RNA Quantitation. *Biotechniques* **29**, 332–337 (2000).
25. Butterfield, D. A., Hardas, S. S. & Lange, M. L. B. Oxidatively modified glyceraldehyde-3-phosphate dehydrogenase (GAPDH) and Alzheimer's disease: many pathways to neurodegeneration. *J. Alzheimers. Dis.* **20**, 369–93 (2010).
26. Kozera, B. & Rapacz, M. Reference genes in real-time PCR. *J. Appl. Genet.* **54**, 391–406 (2013).
27. Touchberry, C. D., Wacker, M. J., Richmond, S. R., Whitman, S. A. & Godard, M. P. Age-related changes in relative expression of real-time PCR housekeeping genes in human skeletal muscle. *J. Biomol. Tech.* **17**, 157–62 (2006).
28. Zampieri, M. et al. Validation of suitable internal control genes for expression studies in aging. *Mech. Ageing Dev.* **131**, 89–95 (2010).

29. Hernandez-Segura, A., Rubingh, R. & Demaria, M. Identification of stable senescence-associated reference genes. *Aging Cell* **18**, e12911 (2019).
30. de Jonge, H. J. M. et al. Evidence Based Selection of Housekeeping Genes. *PLoS One* **2**, e898 (2007).
31. Rubenstein, P. A. The functional importance of multiple actin isoforms. *BioEssays* **12**, 309–315 (1990).
32. Kang, T. H., Park, Y., Bader, J. S. & Friedmann, T. The Housekeeping Gene Hypoxanthine Guanine Phosphoribosyltransferase (HPRT) Regulates Multiple Developmental and Metabolic Pathways of Murine Embryonic Stem Cell Neuronal Differentiation. *PLoS One* **8**, e74967 (2013).
33. Spassov, D. & Jurecic, R. The PUF Family of RNA-binding Proteins: Does Evolutionarily Conserved Structure Equal Conserved Function? *IUBMB Life International Union Biochem. Mol. Biol. Life* **55**, 359–366 (2003).
34. Akhtar, W. & Veenstra, G. J. C. TBP-related factors: a paradigm of diversity in transcription initiation. *Cell Biosci.* **1**, 23 (2011).
35. Casero, R. A., Murray Stewart, T. & Pegg, A. E. Polyamine metabolism and cancer: treatments, challenges and opportunities. *Nat. Rev. Cancer* **18**, 681–695 (2018).
36. Jansen, J. C. et al. TMEM199 Deficiency Is a Disorder of Golgi Homeostasis Characterized by Elevated Aminotransferases, Alkaline Phosphatase, and Cholesterol and Abnormal Glycosylation. *Am. J. Hum. Genet.* **98**, 322–30 (2016).
37. Andersen, C. L., Jensen, J. L. & Ørntoft, T. F. Normalization of real-time quantitative reverse transcription-PCR data: a model-based variance

- estimation approach to identify genes suited for normalization, applied to bladder and colon cancer data sets. *Cancer Res.* **64**, 5245–50 (2004).
38. Vandesompele, J. et al. Accurate normalization of real-time quantitative RT-PCR data by geometric averaging of multiple internal control genes. *Genome Biol.* **3**, RESEARCH0034 (2002).
 39. Tarutani, M., Cai, T., Dajee, M. & Khavari, P. A. Inducible activation of Ras and Raf in adult epidermis. *Cancer Res.* **63**, 319–323 (2003).
 40. Phipps, S. M. O., Berletch, J. B., Andrews, L. G. & Tollefsbol, T. O. Aging cell culture: methods and observations. *Methods Mol. Biol.* **371**, 9–19 (2007).
 41. Sedelnikova, O. A. et al. Senescing human cells and ageing mice accumulate DNA lesions with unreparable double-strand breaks. *Nat. Cell Biol.* **6**, 168–170 (2004).
 42. Bustin, S. A. et al. The MIQE Guidelines: Minimum Information for Publication of Quantitative Real-Time PCR Experiments. *Clin. Chem.* **55**, 611–22 (2009).
 43. Zhang, A. N., Mao, Y. & Zhang, T. Development of Quantitative Real-time PCR Assays for Different Clades of ‘Candidatus Accumulibacter’. *Sci. Rep.* **6**, 23993 (2016).
 44. Muller, M. Comprehensive Invited Review Cellular Senescence: Molecular Mechanisms, In Vivo Significance, and Redox Considerations. *Antioxid. Redox Signal.* **11**, (2009).
 45. Provost, P. R., Marcel, Y. L., Milne, R. W., Weech, P. K. & Rassart, E. Apolipoprotein D transcription occurs specifically in nonproliferating quiescent and senescent fibroblast cultures. *FEBS Lett.* **290**, 139–41 (1991).

46. Yosef, R. et al. p21 maintains senescent cell viability under persistent DNA damage response by restraining JNK and caspase signaling. *EMBO J.* **36**, 2280–2295 (2017).
47. Wiley, C. D. et al. Analysis of individual cells identifies cell-to-cell variability following induction of cellular senescence. *Aging Cell* **16**, 1043–1050 (2017).
48. Sieber, M. W. et al. Inter-age variability of bona fide unvaried transcripts. *Neurobiol. Aging* **31**, 654–664 (2010).
49. Mainzer, C. et al. In vitro epidermis model mimicking IGF-1-specific age-related decline. *Exp. Dermatol.* **27**, 537–543 (2018).
50. Martinez-Jimenez, C. P. et al. Aging increases cell-to-cell transcriptional variability upon immune stimulation. *Science* **355**, 1433–1436 (2017).
51. Bahar, R. et al. Increased cell-to-cell variation in gene expression in ageing mouse heart. *Nature* **441**, 1011–1014 (2006).
52. Somel, M., Khaitovich, P., Bahn, S., Pääbo, S. & Lachmann, M. Gene expression becomes heterogeneous with age. *Curr. Biol.* **16**, R359-60 (2006).
53. Wiley, C. D. et al. Analysis of individual cells identifies cell-to-cell variability following induction of cellular senescence. *Aging Cell* **16**, 1043–1050 (2017).
54. Garbe, J. C. et al. Accumulation of multipotent progenitors with a basal differentiation bias during aging of human mammary epithelia. *Cancer Res.* **72**, 3687–701 (2012).
55. Garbe, J. C. et al. Molecular Distinctions between Stasis and Telomere Attrition Senescence Barriers Shown by Long-term Culture of Normal Human Mammary Epithelial Cells. *Cancer Res.* **69**, 7557–7568 (2009).

56. Debacq-Chainiaux, F., Erusalimsky, J. D., Campisi, J. & Toussaint, O. Protocols to detect senescence-associated beta-galactosidase (SA- β gal) activity, a biomarker of senescent cells in culture and in vivo. *Nat. Protoc.* **4**, 1798–1806 (2009).
57. Koressaar, T. & Remm, M. Enhancements and modifications of primer design program Primer3. *Bioinformatics* **23**, 1289–1291 (2007).
58. Hellemans, J., Mortier, G., De Paepe, A., Speleman, F. & Vandesompele, J. qBase relative quantification framework and software for management and automated analysis of real-time quantitative PCR data. *Genome Biol.* **8**, R19 (2007).
59. Livak, K. J. & Schmittgen, T. D. Analysis of Relative Gene Expression Data Using Real-Time Quantitative PCR and the $2^{-\Delta\Delta CT}$ Method. *Methods* **25**, 402–408 (2001).

Acknowledgements

The authors are grateful to Martha Stampfer and Maite Huarte for donation of HMECs and BJ hTERT ER:RAS cells, respectively. The A.G. and M.M. laboratory is funded by *Consejo de Seguridad Nuclear, Generalitat de Catalunya (2017-SGR-503)* and *Fundación Dexeus Salud de la Mujer 2016* grants. L.G. has been a beneficiary of *Universitat Autònoma de Barcelona* PhD program fellowship. T.A. has been a beneficiary of FI-DGR (*Generalitat de Catalunya*) fellowship.

Authors' contribution

L.G. conducted the experiments, analysed the data, interpreted the results and wrote the main manuscript text, as well as prepared the figures and tables. T.A. conceived the study, participated in sample collection and checked analysis of the obtained data. M.T. and M.M. designed the study, interpreted

the results and directed the research. A.G. helped to supervise the project. All authors discussed the results and contributed to the final manuscript.

Competing interests

The authors declare no competing financial nor non-financial interests.

Figures

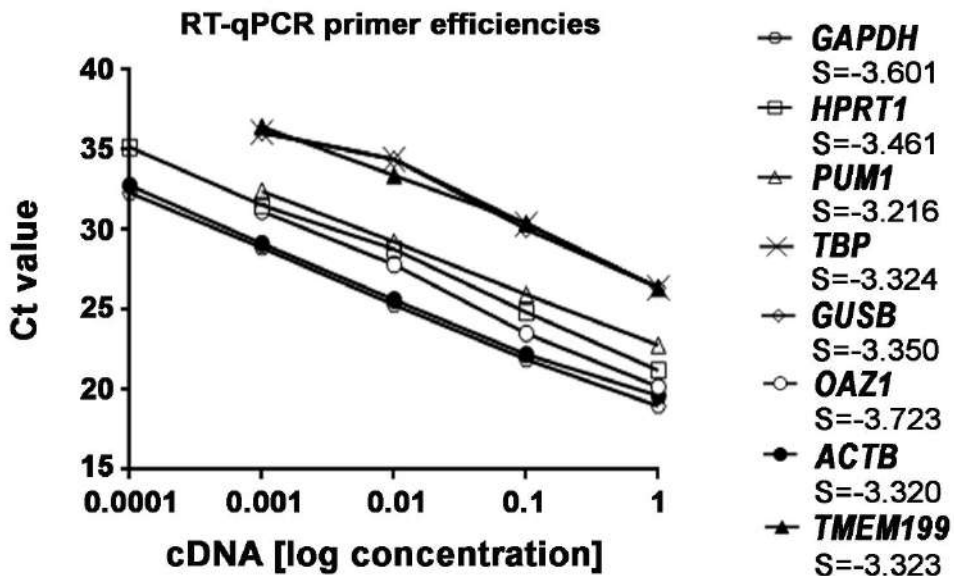


Figure 1. Evaluation of RT-qPCR primer efficiencies. The amplification efficiency for each primer threshold cycle (Ct) and the logarithm of the initial cDNA concentrations were plotted to calculate the slope (S) of each primer pair. Standard curves were generated from at least four dilution points for each primer pair. RT-qPCR reactions for each sample were run in duplicate, with standard deviations < 0.85.

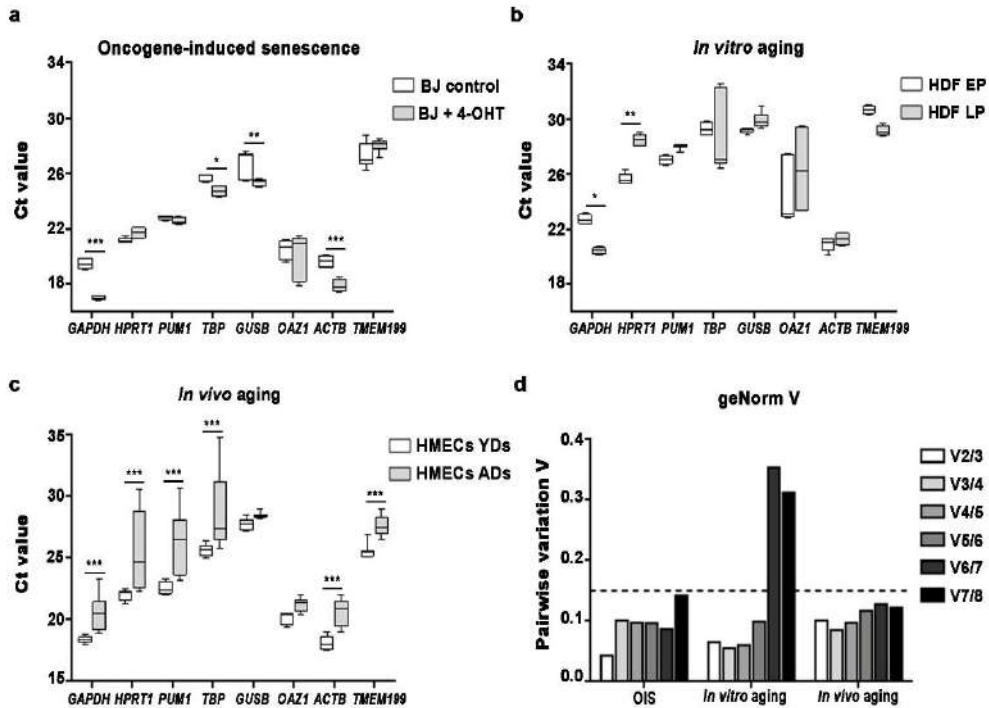


Figure 2. Ct values of eight candidate reference genes in different aging models and the optimal number of reference genes needed for accurate normalisation calculated by geNorm. Box and whisker plots show the raw Ct values of the candidate reference genes during (a) oncogene-induced senescence in BJ fibroblasts, (b) *in vitro* aging in HDFs and (c) *in vivo* aging in HMECs from young and aged donors. (d) Pairwise variation ($V_{n/n+1}$) of candidate reference genes was obtained by geNorm to determine the required number of reference genes for accurate normalisation in each aging model. A discontinuous line indicates a pairwise variation (V) of 0.15, the cut-off value defined by geNorm. Abbreviations: 4-OHT: 4-Hydroxytamoxifen; Ct: cycle threshold; HDFs: Human Dermal Fibroblasts; HMECs: Human Mammary Epithelial Cells; EP: early passage (< 10); LP: late passage (> 20); YDs: young donors; ADs: aged donors. Notes: the boxes include values from the 25th to the 75th percentiles, the line across the box indicates the median, and whiskers show the minimum and maximum values for (continue on the next page)

each reference gene. One-way ANOVA test was conducted. In those cases, where p values were <0.05, a Bonferroni post-hoc test was conducted. Bonferroni corrected p values are shown (*p < 0.05, **p < 0.01, ***p < 0.001).

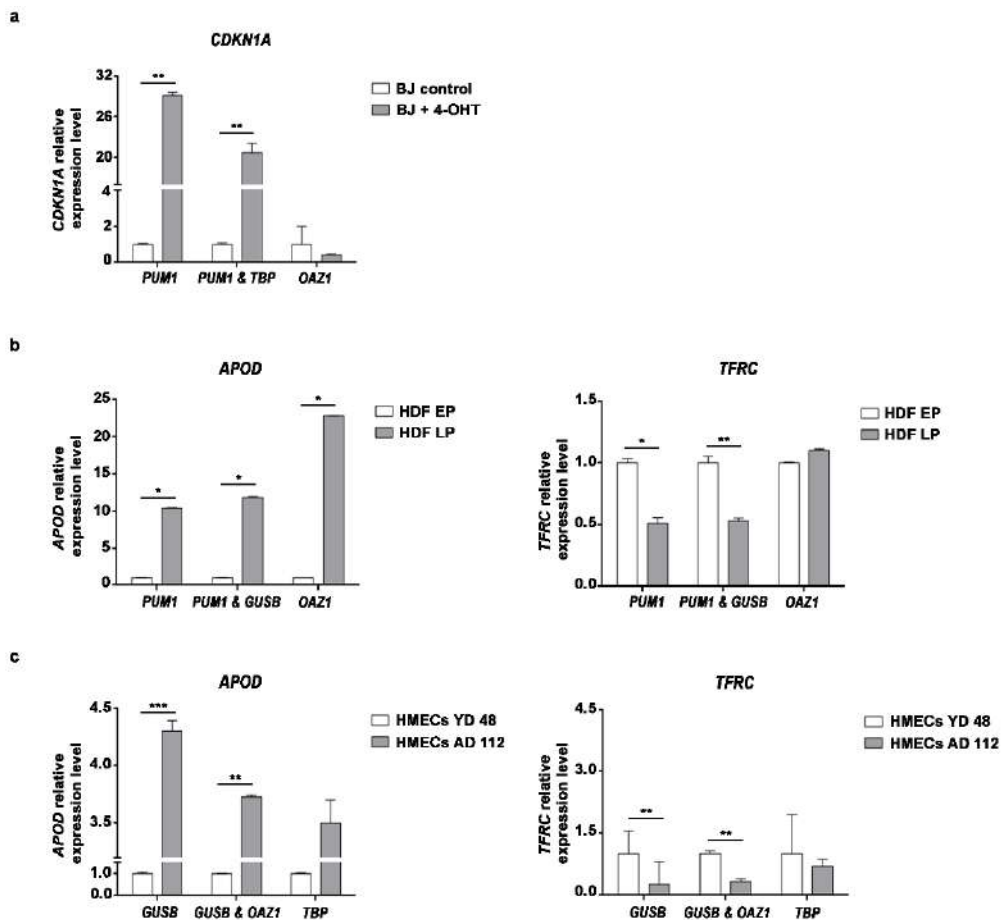


Figure 3. Expression levels of target genes normalised to different reference genes. Gene expression levels were normalised to the indicated reference gene or gene pair in the X axis. **(a)** Relative expression levels of *CDKN1A* in control and in senescent BJ fibroblasts. **(b)** Relative expression of *APOD* and *TFRC* in EP and LP HDFs and **(c)** in HMECs from a young donor and an aged donor (YD 48R & AD 112R, respectively). Relative fold changes in gene expression were obtained according to the $2^{-\Delta\Delta Ct}$ method. Abbreviations: 4-OHT: 4-Hydroxytamoxifen; (continue on the next page)

HDF: Human Dermal Fibroblasts; EP: early passage (< 10); LP: late passage (> 20); HMECs: Human Mammary Epithelial Cells; YDs: young donors; ADs: aged donors; OIS: oncogene-induced senescence. Data are presented as mean and SD. P-values obtained from pairwise comparisons using Welch's t test are shown (* $p < 0.05$, ** $p < 0.01$, *** $p < 0.001$).

Tables

Table 1. List of the reference genes tested by RT-qPCR

Gene Symbol	Accession Number	Primer Sequence	Amplicon Size (bp)	Efficiency (%)	R ²
<i>GAPDH</i>	NM_002046	F:AGCCACATCGCTCAGACAC R:GCCCAATACGACCAATCC	66	98.43	0.998
<i>HPRT1</i>	NM_000194	F:GGCCAGACTTTGTTGGATTG R:TGCGCTCATCTTAGGCTTTGT	144	104.61	0.999
<i>PUM1</i>	NM_001020658	F:CGGTCGTCTGAGGATAAAA R:CGTACGTGAGGCGTGAGTAA	121	94.48	0.997
<i>TBP</i>	NM_003194	F:GAGAGTTCTGGGATTGTACCG R:ATCCTCATGATTACCGCAGC	143	99.89	0.971
<i>GUSB</i>	NM_000181	F:AAGTCCTCACCAGCAGCG R:CCACGGTGTCAACAAGCAT	75	98.84	0.972
<i>OAZ1</i>	NM_004152	F:GGATCCTCAATAGCCACTGC R:TACAGCAGTGGAGGGAGACC	150	85.61	0.997
<i>ACTB</i>	NM_001101	F:CCAACCGCGAGAAGATGA R:CAGAGGCGTACAGGGATAG	97	100.05	0.996
<i>TMEM199</i>	NM_152464	F:ACCAGCATCTGAGAGAAAGG R:CCGTGGAGGCTTACAAC	96	99.95	0.994

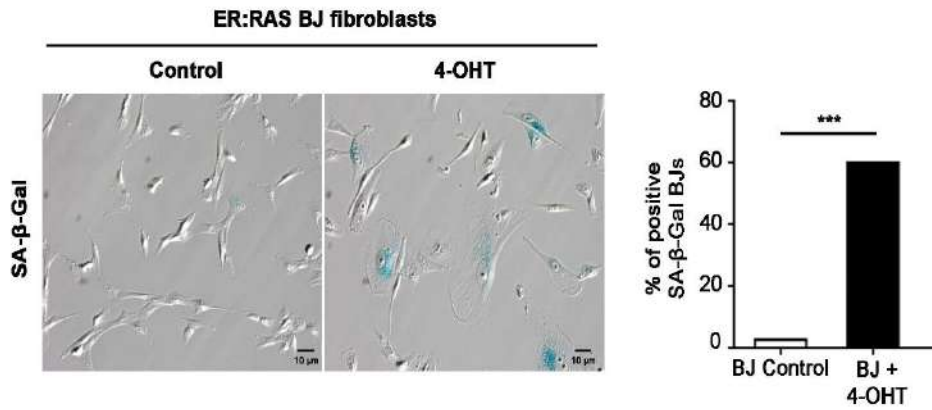
Abbreviations: bp, base pair; F, forward; R, reverse; R², correlation coefficient of the corresponding standard curve.

Table 2. Candidate reference gene expression stability ranked by NormFinder and geNorm in different aging processes. Putative reference genes are listed from top to bottom in order of decreasing stability for each aging process.

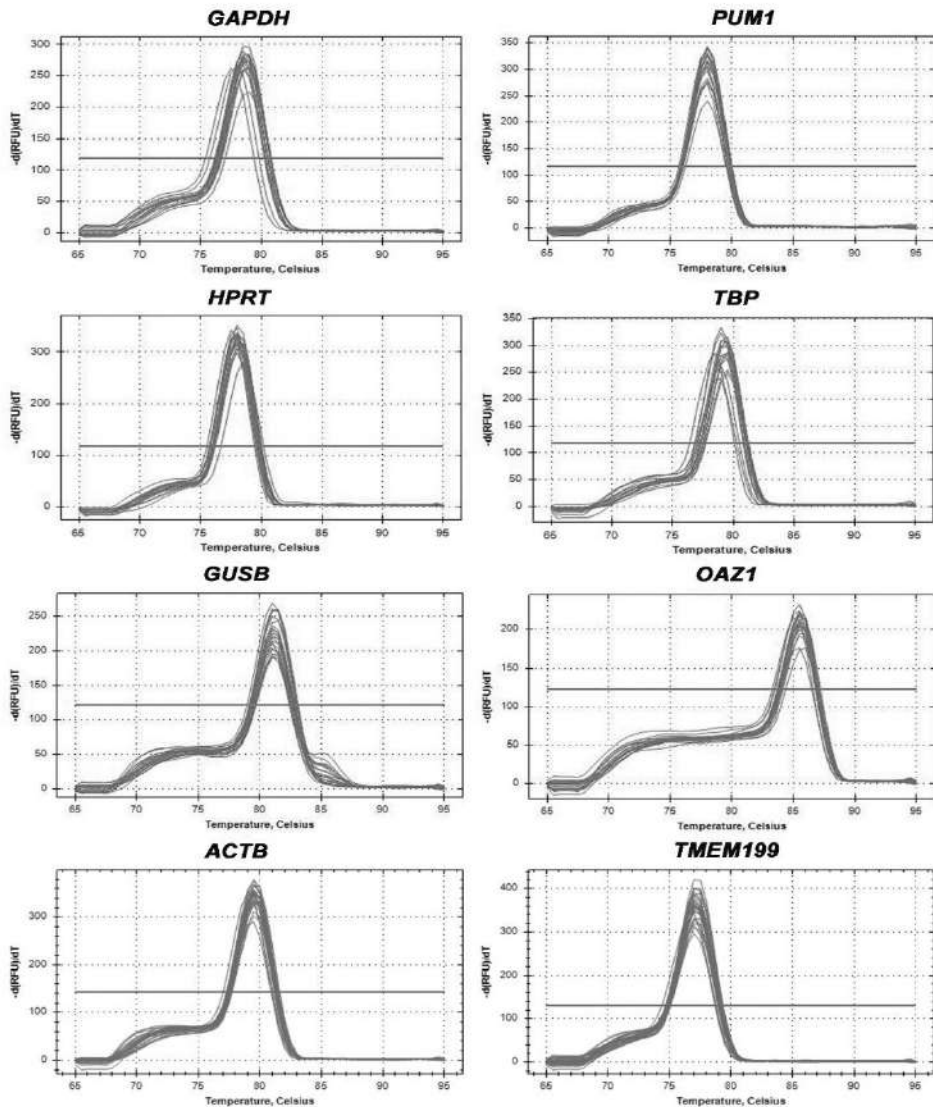
Aging Process	Rank	NormFinder		geNorm	
		Gene	Stability value	Gene	M
OIS	1	<i>PUM1</i>	0.097	<i>PUM1</i>	0.507
	2	<i>TBP</i>	0.109	<i>HPRT1</i>	0.553
	3	<i>GUSB</i>	0.111	<i>TBP</i>	0.570
	4	<i>GAPDH</i>	0.112	<i>GAPDH</i>	0.592
	5	<i>HPRT1</i>	0.144	<i>GUSB</i>	0.598
	6	<i>ACTB</i>	0.204	<i>ACTB</i>	0.673
	7	<i>TMEM199</i>	0.208	<i>TMEM199</i>	0.732
	8	<i>OAZ1</i>	0.343	<i>OAZ1</i>	1.179
In vitro aging	1	<i>PUM1</i>	0.024	<i>PUM1</i>	0.945
	2	<i>GUSB</i>	0.039	<i>GUSB</i>	0.948
	3	<i>GAPDH</i>	0.040	<i>GAPDH</i>	0.951
	4	<i>TMEM199</i>	0.095	<i>TMEM199</i>	0.964
	5	<i>HPRT1</i>	0.148	<i>HPRT1</i>	1.061
	6	<i>TBP</i>	0.251	<i>ACTB</i>	1.283
	7	<i>ACTB</i>	0.401	<i>TBP</i>	2.288
	8	<i>OAZ1</i>	0.408	<i>OAZ1</i>	2.582
In vivo aging	1	<i>OAZ1</i>	0.104	<i>GUSB</i>	0.565
	2	<i>GUSB</i>	0.105	<i>ACTB</i>	0.574
	3	<i>ACTB</i>	0.110	<i>OAZ1</i>	0.583
	4	<i>HPRT1</i>	0.111	<i>PUM1</i>	0.630
	5	<i>TMEM199</i>	0.116	<i>GAPDH</i>	0.716
	6	<i>PUM1</i>	0.123	<i>TMEM199</i>	0.874
	7	<i>TBP</i>	0.127	<i>HPRT1</i>	0.994
	8	<i>GAPDH</i>	0.145	<i>TBP</i>	1.077

Abbreviations: OIS, oncogene-induced senescence; M, expression stability value.

Supplementary Figures



Supplementary Figure 1. Oncogene-induced senescence in BJ fibroblasts. Percentage of positive SA-β-Gal ER:RAS BJ fibroblasts in control conditions and after 4-Hydroxytamoxifen (4-OHT) treatment. The p -value indicates the Chi-square test significant level: *** $p < 0.001$.



Supplementary Figure 2. Melting curve analyses of all primers used in the study. For each primer pair, only single peaks were observed, indicating the specificity of RT-qPCR amplification and the absence of primer dimers.

Supplementary tables

Supplementary Table 1. Primer details of validation genes.

Gene Symbol	ENSEMBL ID	Primer Sequence	Amplicon Size (bp)	Efficiency (%)	R ²
<i>CDKN1A</i>	ENSG00000124762	F: CCGAAGTCAGTTCCTTGTGG R: CATGGGTTCTGACGGACAT	112	92.44	0.996
<i>APOD</i>	ENSG00000189058	F:GCAGCGTCCATTCTCAAAGG R:GGCAGAGGGACAAGCATTTC	133	109.83	0.998
<i>TFRC</i>	ENSG00000072274	F:GCAATCCTGATGACCGAG R:TTTCCATTGTTAACGCA	127	94.49	0.999

Abbreviations: bp, base pair; F, forward; R, reverse; R², correlation coefficient of the corresponding standard curve.





Annex II

Sequence of shRNAs

shMOF1

5'-GCAAGATCACTCGCAACCAAA-3'

shMOF2

5'-CGAAATTGATGCCTGGTATTT-3'

Primer sequences for RT-qPCRs

<i>MOF</i>	F: GAAGTCACGGTGGAGATCGG R: AATTCCTCTCGGCCCTCCT
<i>SIRT1</i>	F: TGA CTGTGAAGCTGTACGAGG R: TGGTTTCATGATAGCAAGCGG
<i>SIRT2</i>	F: GCTGAAGGACAAGGGGCTAC R: CCACCAAGTCCTCCTGTTCC
<i>HDAC1</i>	F: GGACCAGATTTCAAGCTCCA R: CGGCAGCATTCTAAGGTTCT
<i>HDAC2</i>	F: TCCTCCAGCCCAATTAACAG R: AGCTCTCAACTGGCGGTTCC
<i>TIP60</i>	F: TGCGAGTTCTGCCTCAAGTA R: ATCTCATTGCCTGGAGGATG
<i>LOXL1</i>	F: GGCCGCGGTCTCCCTGACTT R: GCTGGGGGAAGCGCAGTAGC
<i>LOXL2</i>	F: ACTGACTGCAAGCACACGGA R: TCAGGTTCTCTATCTGGTTGATCAA
<i>PUM1</i>	F: CGGTCGTCCTGAGGATAAAA R: CGTACGTGAGGCGTGAGTAA

Buffers for ChiP

SDS lysis buffer	1% SDS 10 mM EDTA 50 mM Tris pH 8
Dilution buffer	0.01% SDS 1.1% Triton X-100 1.2 mM EDTA 16.7 mM Tris pH 8 167 mM NaCl
Soft lysis buffer	50 mM Tris pH 8 10 mM EDTA 0.1% NP-40 10% Glycerol
Low salt lysis buffer	0.1% SDS 1% Triton X-100 2 mM EDTA 20 mM Tris pH8 150 mM NaCl
High salt buffer	0.1% SDS 1% Triton X-100 2 mM EDTA 20 mM Tris pH 8 500 mM NaCl
LiCl buffer	250 mM LiCl 1% NP-40 1% NaDOC 10mM Tris pH 8
Elution buffer	1% SDS 100 mM Na ₂ CO ₃

Primer sequences for ChIP-qPCR

Hit1_chr14	F: ATAAGCTTTTTGATGTGCTGCTG R: GAGCTGCTAGCATTCTTCTAA
Hit2_chr5	F: TAACTCATTTATGAGGCCAACGTC R: CTTGTGCATATTGAACCAGCCT
Hit4_chr2	F: AGCTCTGTAAGAACTAAGATTGGGCT R: TTCTATCTTCACGGTTCTCCAAGA
Hit5_chr17	F: TAAGAGAGCCTTGCATCCCA R: AGGCCAGCATCATCCTGATA
SMIM5	F: CAAGGGAAATTGTCCAGACTTC R: AGTAGCTGGGACTACAGGCG
RNAPII	F: CTGAGTCCGGATGAACTGGT R: ACCCATAAGCAGCGAGAAAG

Buffers for lentivirus production

2XHBS	274 mM NaCl
	50 mM HEPES
	1.5 mM Na ₂ HPO ₄
	10 mM EDTA

Buffers for Western Blot

SDS lysis buffer	2% SDS 10% glycerol 50 mM Tris pH 8 Protease Inhibitor Tablets (Sigma-Aldrich, St. Louis, MO, USA)
TTBS	20 mM Tris 150 mM NaCl 0.1% Tween20

Script macro Fiji/ImageJ

```
dir2=getDirectory("C:\Users\EQUIPO\Desktop\Exp")
print(dir2);
ThDir=dir2+"/Threshold/";
print(ThDir);
list2=getFileList(dir2);
f= File.open("\Users\EQUIPO\Desktop\Results.xls");
print(f,"Foto" + "\t" + "Area" + "\t" + "Mean" + "\t" + "IntDen");
for (i=0; i<list2.length; i++) {
    if (endsWith(list2[i], ".tif")){
        print(i+": "+dir2+list2[i]);
        open(dir2+list2[i]);
        imgName=getTitle();
        baseNameEnd=indexOf(imgName, ".tif");
        baseName=substring(imgName,0,baseNameEnd);
        run("8-bit");
        run("Threshold...", "method=Otsu background=Dark");
    }
}
```

```

title = "WaitForUserDemo";

msg = "If necessary, use the \"Threshold\" tool to adjust the
threshold, then click \"OK\".";

waitForUser(title, msg);

makeRectangle(2388,123,177,159);

roiManager("Add");

roiManager("Measure");

makeRectangle(24,24,2700,1992);

minsize=80.50;

maxsize=643.97;

run("Analyze Particles...", "size=&minsize-&maxsize exclude
add display");

File.makeDirectory(ThDir);

saveAs("Tiff", ThDir+baseName+"-threshold");

for (j=0; j<nResults; j++) {
    a=imgName;
    b = getResultString("Area",j);
    c=getResultString("Mean",j);
    d=getResultString("IntDen",j);
    print(f, a+ "\t"+ b+"\t"+c+"\t"+d);
    run("Close All"); }

roiManager("Delete");

selectWindow("Results");

run("Close");

}

}

File.close(f)

```


Acknowledgements

Recuerdo la primera vez que vi a mis dos directoras de tesis. Había una pantalla de por medio y unos 2000 km de distancia entre nosotras. Yo me encontraba en Alemania y ellas en Barcelona. Cuando colgué aquella llamada de Skype, tenía la marca de las uñas clavadas en la palma de mis manos, como síntoma del claro nerviosismo de una entrevista de trabajo, pero, sobre todo, tenía la sensación de haber encontrado algo extraño y único en el mundo de la ciencia. En aquella habitación de una pequeña ciudad de Alemania del Este me sorprendieron la calidez, la alegría, la humanidad y la cercanía que emanaban aquellas dos científicas: Marta y Mariona, Mariona y Marta. Pensé entonces, que si finalmente decidía hacer el doctorado tenía que ser con gente como ellas, científicas tan inteligentes como humanas. Cuatro años después, puedo afirmar que no me confundí ni con la primera impresión de ambas ni al mudarme a Barcelona para realizar el doctorado bajo su dirección.

Marta y Mariona, gracias por dejarme formarme científicamente a vuestro lado, por depositar en mí vuestra confianza, por descubrirme algo tan fascinante como que incluso nuestro DNA falla y se rompe, pero luego puede repararse y seguir adelante. Marta, gracias por discutir las cosas y aportar nuevas ideas y caminos. Me llevo conmigo tu carácter alegre, tu brillante rapidez mental, tu curiosidad, tu creatividad y tu seguridad. Sin duda, un ejemplo como mujer, libre e independiente. Mariona, gracias por ser la razón del equipo, por tu inmenso conocimiento, por tu inteligencia lógica, por tu capacidad de trabajo y por enseñarme a trabajar ordenadamente en el laboratorio. Te agradezco el compromiso que has mostrado en todo momento con esta tesis, a pesar de no estar físicamente, te he sentido cerca siempre que lo he necesitado. A las dos, gracias por haberme tratado con sensibilidad y cariño tanto en los momentos de más alegría como en los momentos de más estrés y ansiedad. Habéis sido unas directoras de tesis maravillosas.

Me gustaría hacer extensivo este agradecimiento al resto de miembros del grupo de Genome Integrity. A Anna, por su serenidad y sabiduría, por ser un apoyo incondicional e imprescindible para este trabajo. A Teresa, por su motivación científica y disposición, por descubrirme Menorca y sus paraísos. A Joan, por su entrañable carácter y bonhomía. A Marina, por su permanente apoyo, su capacidad de escucha, sus ganas de aprender y por preferir FISH al SPOT. A David, por ayudarme siempre que lo he necesitado y por los partidos de pádel y otros deportes. A Nùria, porque no se me ocurre mejor relevo para continuar el estudio del DNA y su reparación.

No puedo irme sin hablar del mayor descubrimiento que me ha aportado este doctorado: mi amigo Toni. Podíamos hacer otra tesis con todas las cosas que me has enseñado. Gracias por enriquecerme culturalmente, por compartir conmigo tu sensibilidad artística, por tus charlas terapéuticas, por abrirme la mente, por tu sarcasmo, por tus recomendaciones cinéfilas, literarias y musicales. Gracias también por coronarme como ganadora de la primera DragCon, por bautizarme con mi nombre de drag, por tu lenguaje de la cuadra, por enseñarme a personajes como la Veneno o Aramis Fuster. Gracias, Antonio por ser el show, la purpurina, la amistad y mi gran tesoro de estos cuatro años.

Por supuesto, me gustaría agradecer al resto de compañeros que han hecho posible un ambiente de trabajo único, haciendo una fiesta de cada día en el laboratorio. A Celia, mi compañera de clase en Biotecnología, de trabajo de fin de grado, de doctorado y también de recta final de tesis. Gracias por demostrarme que hay mucho más aparte del laboratorio, por tus inquietudes, por ser capaz de escribir novelas y por tu fantástico mundo interior. A Marta R, mi hermana catalana, por ser amante y crítica de la investigación científica, por su humor mordaz y por hacerme reír tanto. A Mireia S, por su capacidad para encontrar la belleza, por transmitir tranquilidad y calma. A Aina, por ser tan apasionada, por saber reírse de sí misma, por saber secarse las lágrimas y seguir trabajando. A Andreu, el embajador de Mallorca en la Unidad, por las

conversaciones interesantes, por hacerme dudar, recapacitar y ver las cosas desde otro punto de vista. A Jorge, por ser el chulapo del laboratorio y por ser el postdoc más cercano que he conocido. A Ot, por su amabilidad, por su educación y por su capacidad para ironizar de todo. A Sandra, por ser mi Andalucía en el laboratorio, por tu acento, que me hacía viajar hasta el sur y me llevaba directa a la preciosa Granada, por sonreír tan a menudo y por tener siempre tanta vida en la unidad y fuera de ella. A Mireia R, por sus abrazos tan reconfortantes, por sus detallitos, por su energía y por sus mil planes y propuestas. A Oriol, por poner el toque bohemio de Gràcia en el laboratorio y por haberse integrado tan fácilmente en esta locura de Unidad. A Rober, por ser un gran apoyo durante todo el tiempo que compartimos juntos. Finalmente, a Albert, Mireia B, Laia V, Marta V e Inma, por recibirme con los brazos abiertos y hacerme sentir parte de esta familia desde el primer momento.

Mas allá de los doctorandos o doctores, me gustaría agradecer a María Jesús, Silvia y Jonatan su encomiable labor para mantener el correcto funcionamiento de la Unidad. Muchas gracias María Jesús por ser mi madre catalana, por tus piropos mañaneros, por ser tan resolutiva y estar siempre dispuesta para trabajar. A Nerea, por su espíritu joven y salvaje y por su admirable ética científica. Me gustaría transmitir mi agradecimiento a todos los profesores que forman parte de la Unidad y ayudan a hacerla más competitiva cada día.

Durante estos años, los amigos invisibles, los vídeos de tesis, los disfraces, las visitas al SAF, las cervezas, las fiestas temáticas o las excursiones me han hecho sentirme cálidamente acogida en Cataluña. Gràcies a tots per fer que el meu cor sigui des d'ara una mica més català!

La finalización de este trabajo no habría sido posible sin la ayuda de D. Josep Planas y de la Dra. Martín. Gracias por resucitarme y por darme herramientas útiles para enfrentarme a las dificultades. Muchas gracias por vuestra profesionalidad y por hacerme romper estigmas.

Más allá del mundo del laboratorio, tengo mucho que agradecer a los amigos que me han apoyado durante esta aventura y todas las anteriores. A Alejandra, por no dejarme caer en los abismos, por tener paciencia en los malos momentos, por nuestras charlas y planes cultuquetas y por estar siempre a menos de 200 km de mí. A Pierre, el mejor compañero de piso que se puede tener, por ponerlo todo tan fácil y por ser mi marido sin habernos casado. A Víctor, María y Ester, porque sé que estáis a una llamada de teléfono o a un mensaje de WhatsApp, por todas las conversaciones inteligentes y por hacerme sentirme afortunada por poder contar con vosotros.

Gracias a mi Ekipo. A mi Lore, mi Isa, mi Cintia y mi Irene. No hay palabras para describir todo lo que hemos compartido desde que coincidimos en primero de Biotecnología mientras pensábamos “¿Dónde me he metido?” A vosotras os debo todos los buenos recuerdos de la carrera porque por veros, charlar, reírnos, merecía la pena acudir todos los días a clases de Física o de Biorreactores. Siempre aprenderé de vosotras y seréis un ejemplo para mí. Lore muchas gracias por animarme tanto desde Sevilla, por escuchar mis problemas y por ayudarme a relativizarlos. Esta tesis es muy tuya.

Por supuesto, me gustaría mencionar a mi grupo de amigas de siempre. A mis niñas de Sevilla que a pesar de estar dispersas por el mundo y a pesar de trabajar en otros ámbitos, siempre han preguntado “¿Qué tal va la tesis?” Gracias por sacarme de mis pensamientos y de la rutina diaria cada vez que coincidíamos. Muchas gracias Alejandra, Ana, Angela, Ángeles, Bea, Carmen, Espe, Fátima, Georgina. Gracias también a Bea G, por darme siempre la diversión, por dejarme ser tu Louise y por ser mi Thelma. A mi amigo Andrés, por ser un ejemplo profesional para mí y por tus “illa, illa que tú eres una crack, que tú sacas eso”. Gracias Ángeles, por tu entereza, estoicismo, madurez y fortaleza que me han inspirado tanto para terminar este trabajo.

Construyendo poco a poco esta tesis ha estado siempre mi familia. Muchas gracias a mi madre, por su amor incondicional, por ser la capitana de mi vida,

por ser mi cómplice, por ser tan curiosa e interesarse siempre por mi trabajo. Gracias a mi padre, por dejarme volver a oír su voz, por animarme bajo cualquier circunstancia a trabajar duro y por implicarse cuando ha sido necesario. Gracias papá por haber superado tantos obstáculos para finalmente verme terminar esta etapa. Este es mi regalo. Me gustaría agradecer a mi tío todo su optimismo, sus ganas de alegrarme el día y su tremenda vitalidad que ha sido tan necesaria durante estos años. A Lolita, Niño Enriquito, Cati y Abu, doctores de la vida. Y muchísimas gracias a mi hermana Blanca, mi cuidadora y mi mejor amiga. Gracias Blanca por no soltarme nunca de la mano, por no dejarme ir, por levantarme para hacer deporte, por estar atenta a mí desde otros continentes, por las conversaciones filosóficas sobre la ciencia y por tu confianza en mí para terminar esta etapa. Gracias por tantas virtudes que me han servido como ejemplo durante toda mi vida y, por supuesto, durante el doctorado. Gracias Blanca por ser mi hermana mayor pequeña.

Y finalmente, muchas gracias a Steu. Gracias por llegar a mi vida, descubrir mis luces y mis rincones más oscuros y querer quedarte en ella. Muchas gracias por no dejarme tirar la toalla en ninguna ocasión, por tu paciencia sin límites y por tu escucha activa. Gracias Stef, por calmarme cuando estaba preocupada trayéndome la paz de las montañas de Aosta, por relajarme cuando no salían los experimentos haciéndome reír con tu fina ironía, por regalarme otra familia, por distraerme con tu amplia cultura durante la última etapa de escritura. Gracias Stewi, por tu desbordante e infinita bondad. Grazie Stefano per tutto il tuo amore.

Cover page and section dividers were
designed by **SHOOK Studio**

